


1-1-2013

Synthesis And Characterization Of Transition Metal Arsenide Nanocrystals And The Metastability And Magneto-Structural Phase Transition Behavior Of Mnas Nanocrystals

Yanhua Zhang
Wayne State University,

Follow this and additional works at: http://digitalcommons.wayne.edu/oa_dissertations

 Part of the [Inorganic Chemistry Commons](#), [Materials Science and Engineering Commons](#), and the [Nanoscience and Nanotechnology Commons](#)

Recommended Citation

Zhang, Yanhua, "Synthesis And Characterization Of Transition Metal Arsenide Nanocrystals And The Metastability And Magneto-Structural Phase Transition Behavior Of Mnas Nanocrystals" (2013). *Wayne State University Dissertations*. Paper 721.

This Open Access Dissertation is brought to you for free and open access by DigitalCommons@WayneState. It has been accepted for inclusion in Wayne State University Dissertations by an authorized administrator of DigitalCommons@WayneState.

**SYNTHESIS AND CHARACTERIZATION OF TRANSITION METAL ARSENIDE
NANOCRYSTALS AND THE METASTABILITY AND MAGNETO-STRUCTURAL
PHASE TRANSITION BEHAVIOR OF MNAS NANOCRYSTALS**

by

YANHUA ZHANG

DISSERTATION

Submitted to the graduate School

of Wayne State University,

Detroit, Michigan

in partial fulfillment of the requirements

for the degree of

DOCTOR OF PHILOSOPHY

2013

MAJOR: CHEMISTRY (INORGANIC)

Approved by:

Advisor

Date

DEDICATION

To my loved parents, wife and daughter

ACKNOWLEDGEMENTS

First of all, I want to express my sincerest gratitude to my advisor, Prof. Stephanie L. Brock for her support, guidance and great patience. She is dedicating, knowledgeable, full of passion and always considerate for her student. She teaches me how to be a professional chemist, not only in the intellectual or experimental aspect, but also in the attitude to handle the problems. She always keeps me focused, gives me advices on the project every week and guides me to the next step to achieve my goals. Without her guidance, insights and great patience, I will not be able to finish my thesis today. What I learn from her will continuously benefit me in my future career.

I would also like to take this opportunity to thank my dissertation committee members, Prof. Arthur Suits, Prof. Stanislav Groysman and Prof. Gavin Lawes, for all the help and suggestions they provided, especially for making time from their busy schedules to read and correct the dissertation on time. I would thank Prof. Gavin Lawes again as my main collaborator for the magnetic data collect and analysis. He is a great person and we had many invaluable discussions on the magnetic data of MnAs in the past years. He always sent us the data in time and give suggestions in the email. He took care of and attended my pre-defense even his son was just born recently. I also want to thank Prof. Claudio Verani, who was my dissertation committee but replaced for the health reason of one of his family members. He also helped me a lot and wrote the recommendation letter for me.

I want to thank all the office staffs in the Department of Chemistry, especially Melissa Barton, Debbie McCreless, Diane Klimas, Erin Bachert and Mary Wood. They are all willing to

offer help: Melissa helped me several time for the registration and the procedures reviewing; Debbie solved some contract issues for me and Diane kept our documents very well. I also want to appreciate Nestor Ocampo for the computer technique support and the poster printing. I also appreciate the following CIF members: Dr. Yi Liu and Dr. Zhi Mei for the electron-microscopy guidance and Dr. Mary Jene Heeg for the XRD collecting. I am also grateful to the stuffs in the Science Store who always support me in purchasing chemicals in time.

Many thanks are going to the former and present group members during my Ph.D pursuing period. Dr. Keerthi Senevirathne started the project of MnAs and taught me a lot before he graduated. Dr. Qinghong Yao was one of my good friends and helped me settle down when I first came to the lab. The working passion of Dr. Elayaraja Muthuswamy motivated me very much and he also gave me help with the glove box maintenance and TEM. I had good time with my “neighbor-hood” user Dr. Irina Pala and Dr. Shreyashi Ganguly for many things. I also learned a lot from my current lab-mates and I am very fortunate to have them as colleagues: Dr. Layan Savithra, Lasantha Perera, Asha Bandara, Roshini Pimmachcharige, Derak Jame, Ruchira Liyanage and Jessica Davis. I want to thank all of these people again for research discussions, parties, and coffee times, etc.

Finally, I want to deeply thank my parents and my wife for their enormous support and love. This work is dedicated for them.

TABLE OF CONTENTS

Dedication	ii
Acknowledgements.....	iii
List of Tables	vi
List of Figures.....	vii
List of Schemes.....	xiii
Chapter 1 – Introduction	1
Chapter 2 – Experimental and Materials Characterization Techniques.....	26
Chapter 3 – The Magnetostructural Phase Transformation Behavior in Bulk and Nanoscale MnAs	54
Chapter 4 – Probing the Stability of MnAs Nanocrystals Prepared by Rapid Precipitation.....	72
Chapter 5 – General Synthesis of Metal Arsenide Nanoparticles.....	97
Chapter 6 – Conclusions and Prospectus	101
References.....	112
Abstract.....	127
Autobiographical Statement.....	129

LIST OF TABLES

Table 1.1	Transition metal pnictide materials and associated properties	19
Table 2.1	Characterization techniques derived from the radiation generated from the interaction between a high energy electron beam and a specimen	38
Table 4.1	Effects of reaction time and amount of coordinating ligand on the size of as-prepared type-B MnAs nanocrystals	75

LIST OF FIGURES

Figure 1.1 Illustration of the electronic levels and band gaps of materials varying from bulk to atomic.....	3
Figure 1.2 A schematic diagram of the localized SPR on metal nanoparticles showing the displacement of the electron cloud (negative real and positive imaginary) relative to the nucleus.	4
Figure 1.3 Schematic illustration of La Mer’s model showing the nucleation and growth stages during monodisperse nanoparticle formation	7
Figure 1.4 Illustration of different types of magnets, showing the alignment of the spin orientation in magnetic structures and the corresponding magnetic susceptibilities.	8
Figure 1.5 Typical M vs H curve for diamagnetic materials	9
Figure 1.6 Typical magnetic properties for paramagnetic materials: (A) M vs H curve, (B) χ vs T curve and (C) Inverse χ vs T curve	10
Figure 1.7 Typical magnetic properties for ferromagnets: (A) χ vs T curve, (B) Inverse χ vs T curve and (C) M vs H hysteresis	12
Figure 1.8 Typical magnetic properties for antiferromagnetic materials: (A) M vs H curve, (B) χ vs T curve and (C) Inverse χ vs T curve.	13
Figure 1.9 Comparison of spin alignment behavior between bulk (multidomain) and nanomaterials (single domain) along the direction of the applied field	16
Figure 1.10 Comparison of magnetic behaviors in magnetization vs applied field (moving from strong field to weak field, left to right) for (A) ferromagnets (FM), (B) superparamagnets (SPM) and (C) paramagnets (PM).	17
Figure 1.11 A typical FC/ZFC curve for a nano-ferromagnet showing the blocking temperature (T_b) and the Curie temperature (T_C). FM, SPM and PM indicate ferromagnetic region, superparamagnetic region and paramagnetic region	18
Figure 1.12 The magneto-structural transition in bulk MnAs	22

Figure 2.1 A typical schematic diagram for a glove box (original figure adapted from Ref. 96)	27
Figure 2.2 An illustration of a typical Schlenk Line. (Picture adapted from Ref. 97)	29
Figure 2.3 A schematic diagram depicting X-ray generation inside the X-ray tube ...	30
Figure 2.4 Illustration of (A) Cu $K\alpha$ X-ray generated from electron transition from 2p to 1s (1s vacancy is caused by ionization) (B) different types of X-rays generated by the X-ray source (adapted from West, see Ref. 99). $K_{\alpha 1}$ and $K_{\alpha 2}$ correspond to two different spin states for the 2p electron.....	31
Figure 2.5 Illustration of Bragg's Law.....	33
Figure 2.6 Electronic excitations occurring after a specimen is hit by a high energy electron beam in an electron microscope	37
Figure 2.7 Schematic diagram for a TEM with STEM capability.....	40
Figure 2.8 Ray diagram showing the parallel beam operation in the TEM: (left) using just C1 and an underfocused C2 lens, (right) creating parallel beams using C1, C2, and the objective lens.....	41
Figure 2.9 Ray diagram showing the convergent-beam/probe mode in the TEM (adapted from Williams, see Ref. 107).....	42
Figure 2.10 Ray diagrams showing how to produce (A) a bright-field (BF) image from the direct beam and (B) a dark-field (DF) image from the diffracted beam, by controlling the objective aperture.....	43
Figure 2.11 The working principles of EDS	45
Figure 2.12 Ray diagram showing the two basic operations of the TEM imaging system: (A) diffraction mode and (B) image mode.....	46
Figure 2.13 A schematic diagram showing the various types of electron detectors in a STEM	48
Figure 2.14 General schematic diagram for (A) a SQUID detection coil and (B) a SQUID magnetometer	51
Figure 2.15 A general schematic diagram of a coil set for AC magnetic susceptibility measurements.....	53

Figure 3.1 The PXRD pattern of bulk MnAs before and after etching	55
Figure 3.2 The PXRD pattern of MnAs nanoparticles synthesized by the slow heating method (type-A MnAs nanoparticles). The reference PDF corresponds to α -MnAs.	58
Figure 3.3 TEM image including the size distribution and the EDAX pattern of MnAs nanoparticles prepared by the slow heating method (type-A nanoparticles)	58
Figure 3.4 The PXRD pattern of type-B MnAs nanoparticles prepared by the rapid injection method. The reference PDF corresponds to β -MnAs.....	59
Figure 3.5 TEM image of MnAs nanoparticles prepared by the rapid injection method.....	60
Figure 3.6 PDF refinements on the bulk MnAs (left) and type-A MnAs nanoparticles (right). The blue curve represents the experimental PDF data and the red line is the calculated PDF data from Rietveld refinement. The green curve is the difference curve between the experimental data and calculated model data.....	61
Figure 3.7 (a) The difference curves (orange) of diffraction data for bulk MnAs between 295 K (blue) and 335 K (red); (b) The difference curves (violet) of diffraction data for type-A MnAs nanoparticles between 295 K (blue) and 335 K (red); (c) Comparison of the (a) and (b) curves (the (b) curve is scaled by a factor of 4 for direct comparison).....	62
Figure 3.8 (a) The difference curves (orange) of PDF data for bulk MnAs between the PDF at 295 K (blue) and 335 K (red); (b) The difference curves (violet) of PDF data for type-A MnAs nanoparticles between the PDF at 295 K (blue) and 335 K (red); (c) Comparison of the curve (a) and (b) (scaled by a factor of 4).....	63
Figure 3.9 Comparison of lattice parameters and atomic displacement factors from Rietveld refinements of the bulk MnAs and type-A MnAs nanoparticles to the α -phase structure model upon heating from 295 K to 335 K (red for bulk and cyan for type-A nanoparticles on heating) and cooling back from 335 K to 295 K (blue for bulk and magenta for type-A nanoparticles): (a) lattice parameter \underline{a} , (b) lattice parameter \underline{c} , (c) U_{iso} for Mn, (d) U_{iso} for As.....	64
Figure 3.10 PDF refinements for type-B MnAs nanoparticles at (a) 295 K with α model fitting, (b) 295 K with β -model fitting, (c) 335 K with α model fitting and (d) 335 K with β model fitting. The colors correspond to the same curve representations as shown in Figure 3.11	65

Figure 3.11 The difference curves (orange) of diffraction data for bulk MnAs at 295 K (blue) and at 335 K (red); (b) The difference curves (violet) of diffraction data for type-A MnAs nanoparticles at 295 K (blue) and 335 K (red); (c) comparison of the (a) and (b) difference curves. The orange curve has been enlarged by a factor of 10.	66
Figure 3.12 (a) The difference curves (orange) of PDF data for bulk MnAs at 295 K (blue) and at 335 K (red); (b) The difference curves (violet) of PDF data for type-B MnAs nanoparticles at 295 K (blue) and 335 K (red); (c) comparison of the difference curves from (a) and (b). The orange curve has also been enlarged by a factor of 10 to enable a meaningful comparison.	67
Figure 3.13 Comparison of lattice parameters from PDF refinements of bulk MnAs and type-B MnAs nanoparticles to the β -phase structure model upon heating from 295 K to 335 K (red for bulk and cyan for type-B nanoparticles) and cooling back from 335 K to 295 K (blue for bulk and green for type-B nanoparticles): (a) lattice parameter a , (b) lattice parameter b , (c) lattice parameter c	68
Figure 3.14 Comparison of AC magnetization (a) and unit cell volume (b) in bulk MnAs, type-A MnAs nanoparticles and type-B MnAs nanoparticles. All unit cell volumes are based on the refinements of the α -model. Dashed lines at 303 K and 317 K indicate the temperature range of the first order structural transitions of the bulk MnAs. The color settings are: blue (cooling, bulk), red (heating, bulk), cyan (cooling, type-A nanoparticles), magenta (heating, type-A nanoparticle), green (cooling, type-B nanoparticles) and orange (heating, type-B nanoparticles)	70
Figure 4.1 The XRD patterns of synthesized Type-B MnAs nanocrystals prepared using 5g of TOPO at different times. The drop lines indicate the reference spectrum of the β -MnAs standard (PDF# 71-0923).....	76
Figure 4.2 TEM image of type-B MnAs nanoparticles indicating highly uniform 18 nm samples are prepared (scale bar = 100 nm).....	77
Figure 4.3 TEM images and size distribution histograms of synthesized Type-B MnAs nanoparticles with different sizes (the scale bar is 20 nm): (a) 32 nm; (b) 21 nm; (c) 18 nm; (d) 12 nm.	78
Figure 4.4 XRD image of 21 nm β MnAs nanocrystal before and after heating at 393 K.....	79

Figure 4.5 HAADF of type-B MnAs nanoparticles and elemental analysis maps for Mn, As, O, P and Cl, respectively.	80
Figure 4.6 EDAX comparison of the composition for type-A (top) and type-B (bottom) MnAs nanoparticles.....	82
Figure 4.7 HAADF image and EDS map for type-A MnAs nanoparticles (no P or Cl is detected).....	83
Figure 4.8 Line profile elemental analysis for several single Type-B MnAs nanoparticles.....	84
Figure 4.9 Temperature dependent XRD for type-B MnAs nanoparticles cooling to -150 °C and then warming back to room temperature (from bottom to top)	85
Figure 4.10 XRD image comparison for 32 nm nanocrystals after aging for 3 weeks (left) and after cooling at 77 K and then rewarming to room temperature (right).....	86
Figure 4.11 High resolution TEM images and FFT processing of a type-B MnAs nanocrystal before cooling (left) and after warming to room temperature from 77 K (right).....	87
Figure 4.12 Comparison of the T dependent magnetic susceptibility (magnetic susceptibility per mole of Mn) for type-B MnAs nanocrystals(from 12 to 30 nm, left) and type-A MnAs nanoparticles (22 nm, right).....	88
Figure 4.13 Modeling of magnetic structure of α and β MnAs (The spin orientations are in the same direction).	89
Figure 4.14 (left) DC magnetization acquired at 300 K for 21 nm type-B MnAs nanoparticles before and after cooling to 77 K and returning to room temperature. (right) XRD of 21 nm type-B MnAs nanoparticles at room temperature before and after cooling to 77 K.....	90
Figure 4.15 XRD data comparison for 21 nm type-B MnAs nanoparticles after cooling and after being under 5 T field	91
Figure 4.16 Magnetic moment measurements of MnAs nanoparticles: (A) 30 nm type-B, (B) 21 nm type-B), (C) 12 nm type-B, and (D) 22 nm type-A.....	92
Figure 4.17 A) XRD measurements of different sizes of type-B MnAs nanoparticles upon warming to room temperature from 77 K. To clearly differentiate the structure, a $2\theta = 45^\circ \sim 55^\circ$ window is selected out for comparison. The solid drop-lines are the standard β -phase	

MnAs reference (PDF# 71-0923) and the dash drop-lines are the standard α -phase MnAs reference (PDF# 28-0644).....	94
Figure 4.18 Room temperature XRD patterns (left) and TEM images (right) of polydisperse 32 nm (average) type-B MnAs nanoparticles before and after cooling to 77 K.....	95
Figure 5.1 XRD patterns for synthesized transition metal arsenide nanocrystals (from top to bottom): NiAs, FeAs and CoAs. The solid drop lines are the reference patterns for NiAs (PDF# 75-0603), FeAs (PDF# 71-2216) and CoAs (PDF# 77-1351).....	100
Figure 5.2 TEM micrographs for transition metal nanocrystals (from top to bottom): NiAs, FeAs and CoAs	101
Figure 5.3 XRD patterns for synthesized transition metal arsenide nanocrystals: FeAs (left) and CoAs (right). The solid drop lines are the reference patterns for FeAs (PDF# 71-2216) and CoAs (PDF# 77-1351).....	103
Figure 5.4 TEM images of transition metal arsenide nanocrystals: FeAs (left) and CoAs (right).....	104
Figure 5.5 The XRD pattern (left) and TEM image (right) of nickel arsenide ($\text{Ni}_{11}\text{As}_8$) nanoparticles.....	105

LIST OF SCHEMES

Scheme 3.1 The procedure for type-A MnAs nanoparticle synthesis by the slow heating method	56
Scheme 3.2 The procedure of type-B MnAs nanoparticle synthesis by the fast injection method	57
Scheme 5.1 The synthesis of NiAs nanocrystals by metal nanoparticle conversion....	98
Scheme 5.2 The synthesis steps for preparation of metal arsenide nanoparticles by direct reaction	102

CHAPTER 1

Introduction

As the size of materials is scaled down from extended structures in bulk materials to the nanoscale level (1-100 nm), materials tend to exhibit unique properties. Nanomaterials are usually defined as being smaller than a one tenth of a micrometer in at least one dimension.¹ The chemical and physical properties differ from bulk materials in their electronic,² magnetic,³ optical,⁴ or catalytic attributes,⁵ depending on the materials' structures and intrinsic properties. The novel properties of nanomaterials make them of interest for applications impacting the environment,⁶ medicine,⁷ energy,⁸ information,⁹ and communication,¹⁰ among others. For example, magnetic nanoparticles can be bound to antibodies to label specific molecules, structures or microorganisms;¹¹ and nanoporous materials can be used for small drug molecule encapsulation and transportation.¹² Recent advances in nanotechnology for LEDs (light-emitting diodes)¹³ or QCAs (quantum caged atoms)¹⁴ could greatly reduce the energy consumption for illumination; and sub-10 nm gold nanoparticles show excellent catalytic performance in reactions such as CO oxidation due to the dramatically increased surface area to volume ratio compared to bulk gold, which is chemically inert and considered a poor catalyst.¹⁵ Due to the properties of nanomaterials and their wide applications in many devices, the development of nanomaterials with new compositions or by improved synthetic methods is in high demand as is a detailed understanding of how properties vary with size. Over the past decade, the Brock group has contributed greatly to the synthesis of new nanomaterials of transition metal pnictides and the study of their catalytic and magnetic properties.¹⁶

In this dissertation, the research is mainly focused on the magnetostructural phase transformation and metastability of MnAs nanoparticles. In addition, the development of a general synthetic strategy for transition metal arsenide nanoparticles, including Ni₁₁As₈, FeAs, CoAs, and MnAs and the study of their properties will also be discussed.

1.1 Nanoparticles and Properties

Nanoparticles are of great scientific interest because the properties of the nanoparticles are intermediate between those of bulk materials and molecular/atomic structures. Due to the significantly decreased size relative to bulk materials, the ratio of the surface atoms to those of the interior is greatly increased. Thus, it is easy to deduce that the catalytic performance will be greatly enhanced for nanoparticles because of the greater number of exposed active sites caused by the increased surface to volume ratio.¹⁷

The electronic structure of nanoparticles is also different from either bulk materials or molecular/atomic structures. Bulk materials ($> 0.1 \mu\text{m}$) have constant physical properties, regardless of their size difference, while size-dependent properties are characteristic of nanoparticles.¹⁸ Thus, the energy band shown in bulk materials is broad and continuous, while the orbitals describing the energy for molecules or atoms are discrete and definite. However, due to size effects, the energy bands in nanomaterials become discrete and tunable, or more “molecule-like”, as the size is decreased. The generic band energy diagram of a semiconductor and illustration of how it breaks down into atomic orbitals is shown in Figure 1.1 (adapted from Schmid¹⁹). The tunable band gap between the highest occupied molecular orbital (HOMO) and the lowest unoccupied molecular orbital (LUMO) results in size-dependent emissions of

semiconductor nanocrystals. The unexpected optical properties arise because the nanocrystals are small enough to confine the electrons and produce quantum effects. The size dependent optical properties make the semiconductor nanocrystals, or quantum dots widely studied for photovoltaic and biomedical imaging devices.

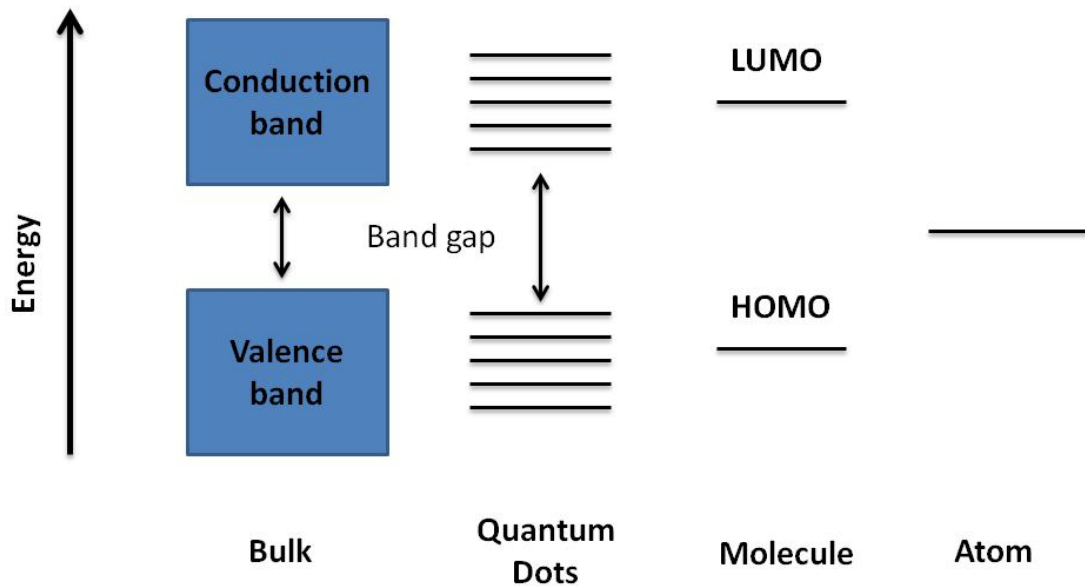


Figure 1.1 Illustration of the electronic levels and band gaps of materials varying from bulk to atomic (adapted from Schmid, ref. 29).

Another property difference between bulk materials and nanomaterials is the Surface Plasmon Resonance (SPR), observed in some metal nanoparticles.²⁰ SPR corresponds to the surface electromagnetic waves which propagate parallel to the metal/dielectric interface, and which are easily affected by the interface boundary change. For metal nanoparticles, a combined oscillation from valence electrons occurs when light matching the frequency of surface electrons oscillating against the attraction force of positive nuclei impacts on the interface. SPR in

nanosized structures is called localized SPR, and the effect of the electric field on electron cloud oscillations is shown in Figure 1.2. This results in unique absorbance properties of noble metal nanoparticles and can be used in analytical devices for diagnosis and therapeutics.

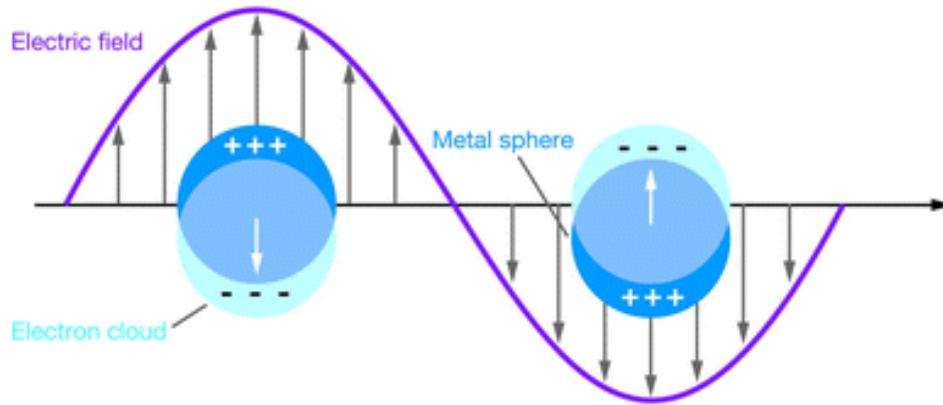


Figure 1.2 A schematic diagram of the localized SPR on metal nanoparticles showing the displacement of the electron cloud (negative real and positive imaginary) relative to the nucleus.

For ferromagnetic or ferrimagnetic nanoparticles, the size dependent property variation from bulk materials includes superparamagnetism when the size of the nanoparticle is reduced to less than that of a single magnetic domain. In addition, the magnetic coercivity (the energy needed to flip spins to their opposite direction) and the blocking temperature (the temperature at which there is sufficient the thermal energy to induce the magnetic domain relaxation) are tunable by changing the size and shape of the nanoparticles. The magnetic nanoparticles can be potentially used in the development of data-storage devices, drug delivery and release, magnetic refrigeration and contrast agents for MRI.^{3a, 21}

1.2 Synthesis of Nanoparticles

Typically, there are two approaches widely used for nanoparticle synthesis: top-down or bottom-up methods. The top-down method is the strategy that breaks down bulk materials using physical methods such as lithography to create nanomaterials. However, the minimum resolution is typically greater than 200 nm.²² Bottom-up methods use molecular level precursors to construct the nanomaterials by chemical synthesis and crystal growth.^{22c, 23} A key advantage for bottom-up methods is the ability to control the size dimension by controlling the chemical reaction parameters. Furthermore, various surface ligands can be used to functionalize the surface of the materials and alter the physicochemical properties.²⁴ The formation of monodisperse nanoparticle samples is important to understand and exploit their size-dependent properties. Accordingly, bottom-up chemical synthesis is used exclusively in the dissertation research.

1.2.1 Chemical Synthesis of Nanoparticles

A variety of chemical synthesis methods can be used for the preparation of nanoparticles such as solvothermal methods,²⁵ temperature programmed reduction (TPR),²⁶ microwave synthesis,²⁷ micellar or inverse micellar synthesis²⁸ and solution phase arrested precipitation (SPAP).²⁹ In this dissertation, we adopt the SPAP method for the synthesis of transition metal arsenide nanoparticles by decomposition of organometallic reagents in mixtures of high boiling point solvents and coordinating ligands.

In SPAP synthesis, the selection of the coordinating ligands is very important.³⁰ The coordinating ligands, which are normally bulky groups or consist of long alkyl carbon chains with bonding group at their tails, are useful to control the growth of nanocrystals. Common

coordinating ligands include alkyl amines, alkyl acids, alkyl phosphines or alkyl phosphine oxides. In some reactions, more than one kind of ligand may be selected to control the reaction.³¹ The coordinating ligands bind to the growing nanoparticle nuclei in a dynamic fashion, thereby resulting in a decrease of the growth kinetics. Additionally, depending on the energy of different facets of nanocrystals, the bonding strengths for specific ligands also vary. These variations in bonding strengths are often adopted for the synthesis of 1-D or 2-D nanostructures, which grow anisotropically due to the different growth rate of crystal facets.³² In general, the shorter the alkyl chain length or the lower the concentration of ligands, the larger the particles will form because of the decreased steric stabilization, and vice versa.

Currently, the method of decomposition of organometallic precursors in hot coordinating solvents (more than 120 °C) has been proved to be among the most successful nanoparticle preparation methods in terms of the quality and monodispersity of the product.³³ There are two key steps for controlling nucleation and growth in the formation of quality nanocrystals with a narrow size distribution. Figure 1.3 (adapted from Kolimov³⁴) illustrates the formation of highly monodisperse nanocrystals by La Mer's model of nucleation and growth.³⁵ First, the injection of the organometallic precursors into the hot coordinating ligands and solvents results in the immediate decomposition of the precursors, causing a supersaturation of monomers. The supersaturated monomers then form nuclei as the seeds for the next growth step. The growth rate will be rapid, proceeding by the consumption of additional monomers by the formed seeds. When the monomer concentration goes down to the threshold limit, there will be no more nuclei formed. After depletion of the monomers, the growth steps are governed by Ostwald ripening process, which is commonly observed in solid solutions/liquid sols that describes the evolution of an inhomogeneous system over time. During this process in nanoparticle synthesis, small

nanoparticles will dissolve due to the higher surface energy and redeposit onto larger nanocrystals. The supersaturation and nucleation steps can also be optimized by using a slow heating rate (usually over hours) of the precursors to the reaction temperature. The reaction time and the reaction temperature are two other factors that impact the SPAP reaction. Generally, higher temperatures and longer Ostwald ripening times will lead to larger nanoparticles due to the faster growth rate and longer growth time, respectively.

To make the nanoparticle sample more monodisperse, in addition to the control of the reaction discussed above, post synthesis steps such as size selective precipitation (SSP) can be

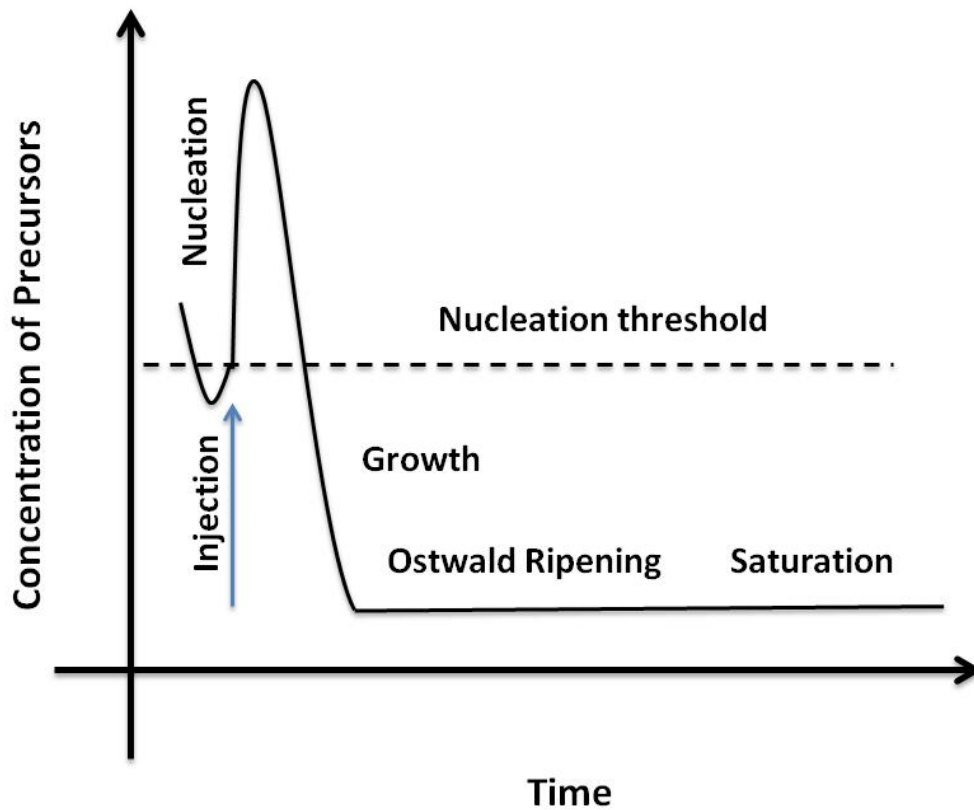


Figure 1.3 Schematic illustration of La Mer's model showing the nucleation and growth stages during monodisperse nanoparticle formation

employed. SSP involves the further use of a solvent and antisolvent defined relative to the surface ligands on the nanoparticles to control the precipitation of nanoparticles, with larger nanoparticles settling out first. Smaller nanoparticles are then separated step by step with the further addition of the anti-solvent.

1.3 Magnetism

Magnetism is a physical property of materials. Materials can be basically cataloged as ferromagnetic, ferrimagnetic, paramagnetic, antiferromagnetic and diamagnetic depending on their magnetic response (magnetic susceptibility (χ), defined as the ratio between the magnetization (M) and the applied field (H)) to an external magnetic field. Their differences can

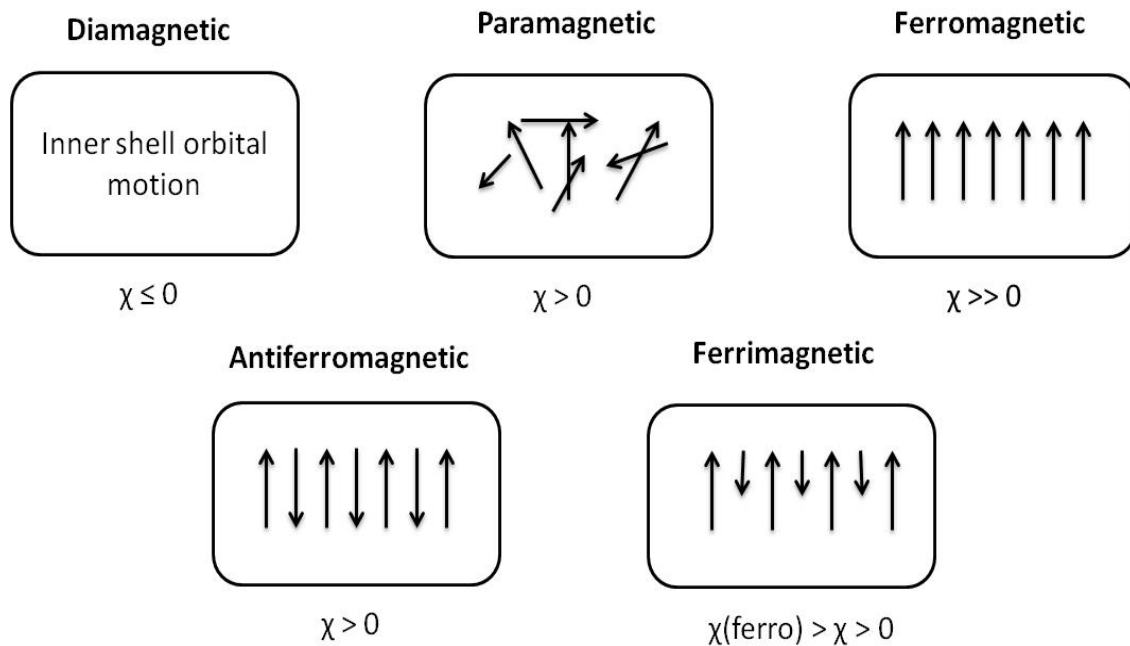


Figure 1.4 Illustration of different types of magnets, showing the alignment of the spin orientation in magnetic structures and the corresponding magnetic susceptibilities (adapted from Myers, see ref. 56).

be understood in terms of magnetic moment alignment as shown in Figure 1.4.³⁶

1.3.1 Diamagnetism

Diamagnetism appears in all materials due to the presence of paired electrons and is manifested by the expulsion of an external magnetic field. Those materials containing only paired electrons in a structure are classified as diamagnetic because the susceptibility values are very small and negative ($\chi \sim -10^{-5}$) compared to other kinds of materials with unpaired electrons, where χ is larger and positive. Because there are no unpaired electrons, the intrinsic electron magnetic field cannot produce any bulk effect and the magnetization arises from the orbital motions from the electrons, which are essentially temperature independent. Figure 1.5 shows the typical response for a diamagnetic material to an applied magnetic field. In materials with

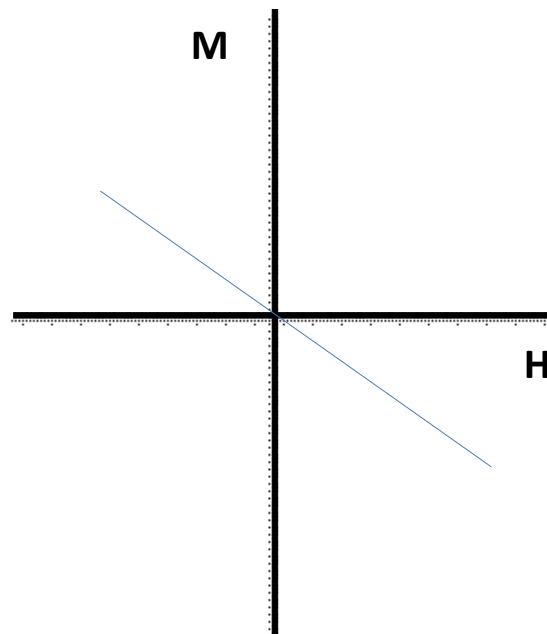


Figure 1.5 Typical M vs H curve for diamagnetic materials

unpaired electrons, the diamagnetic effect is minimal.

1.3.2 Paramagnetism

There are unpaired electrons in paramagnetic materials. Unlike paired electrons, which must have the intrinsic magnetic moments (spins) pointing in opposite directions due to the Pauli Exclusion Principle, that an unpaired electron is possible to align its magnetic moment (spin) in any direction. These spins have a tendency to be aligned parallel with the direction of the applied field. The susceptibility for paramagnets is small and positive (typically in the range from 10^{-5} to 10^{-3}). Figure 1.6 shows a magnetization vs. applied curve for a typical paramagnet; the magnetization increases linearly with applied field. The magnetic susceptibility of a paramagnet varies with $1/T$ and can be modulated by the Curie Law (Equation 1.1), as shown in Figure 1.6 (B) and (C).

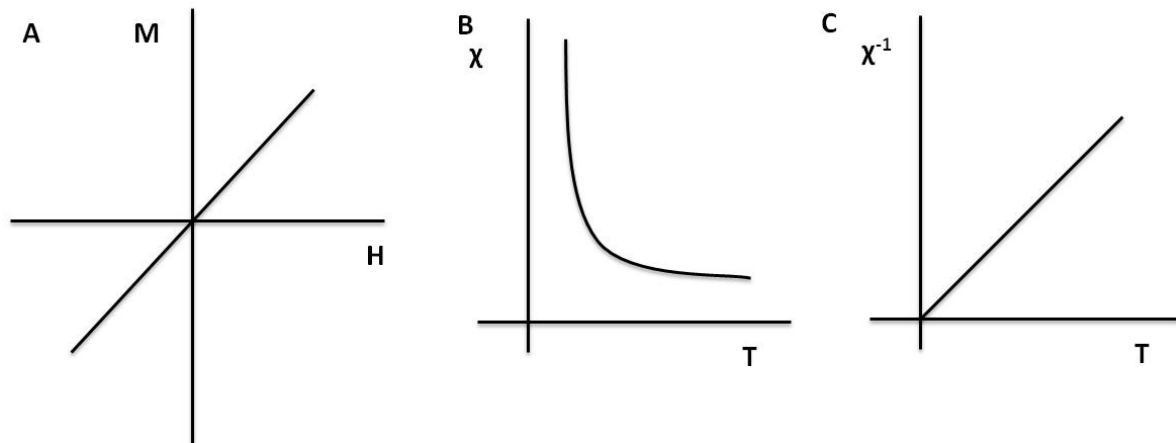


Figure 1.6 Typical magnetic properties for paramagnetic materials: (A) M vs H curve, (B) χ vs T curve and (C) Inverse χ vs T curve.

$$\chi = (C/T), \quad \chi^{-1} = T/C \quad (1.1)$$

C=Curie Constant

1.3.3 Ferromagnetism

Ferromagnetism is the basic mechanism by which certain materials form permanent magnets, or can be attracted to magnets. Of all types of magnetism, ferromagnetism is the strongest and ferromagnetic materials are characterized by large positive susceptibilities ($\chi \gg 1$), which make ferromagnetic materials the most important class of magnetic materials. Ferromagnetic materials are extensively used in magnetic recording media, electro-magnets, transformers, electromagnetic relays and magneto-refrigeration. The magnetic moments arise by the orientation of the unpaired electrons in parallel with the direction of the applied magnetic field as with paramagnets. However, unlike paramagnets, there is a tendency for these magnetic moments to orient parallel to each other to form a lower energy state. Thus, even when the applied field is removed, the electrons in the materials maintain a parallel orientation and give rise to a permanent magnetic moment. However, this parallel orientation alignment can be disordered by the application of thermal energy. If the thermal energy is greater than the energy of spin alignment, the material will become paramagnetic. The temperature above which the ferromagnetic alignment is lost is referred to the Curie temperature (T_c). T_c can be discerned from a χ -T curve, as shown in Figure 1.7 (A). Likewise, a plot of inverse susceptibility vs. temperature in the paramagnetic region will be linear, as in Figure 1.6 (C), but will have a

positive x-intercept corresponding to the Weiss constant (T_θ) in Equation. 1.2 (Curie-Weiss Law), as shown in Figure 1.7 (B). Ideally, $T_\theta = T_C$.

$$\chi = \frac{C}{T - T_\theta} \quad (1.2)$$

$$\chi^{-1} = \frac{T - T_\theta}{C}$$

C is the Curie constant, T_θ is the Weiss constant.

For typical ferromagnets below T_C , there is a hysteresis curve in the plot of the magnetization vs. applied field, as shown in Figure 1.7 (C). Ewing first introduced the hysteresis and such hysteresis loops are used to characterize and quantify the magnetization of materials. In Figure 1.7 (C), the virgin curve (VC) shows the initial magnetization as measured as a function

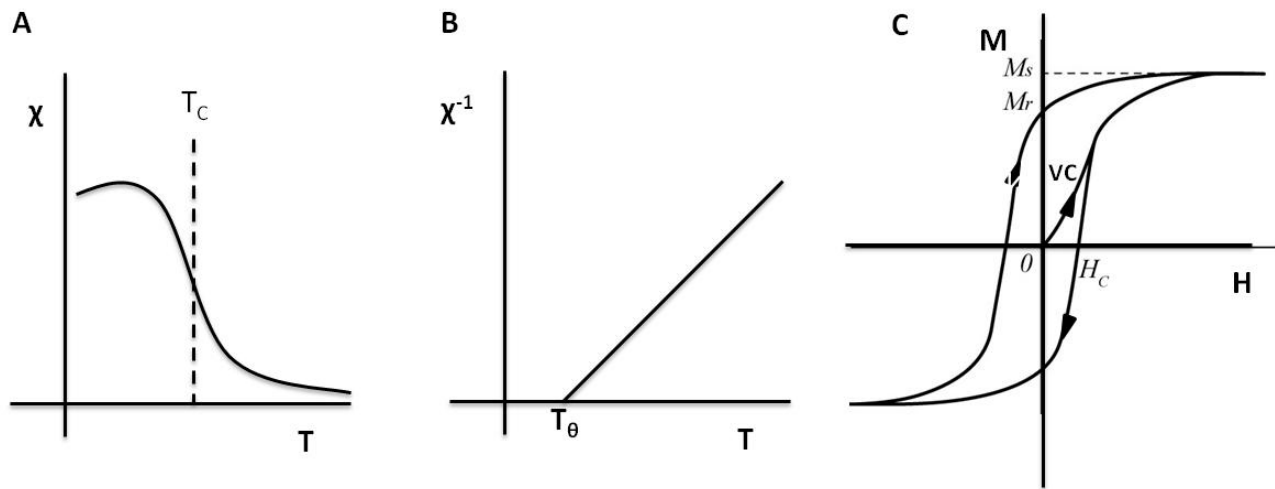


Figure 1.7 Typical magnetic properties for ferromagnets: (A) χ vs T curve, (B) Inverse χ vs T curve and (C) M vs H hysteresis

of applied field. When all the moments in the material are aligned with the direction of the applied field, the magnetization will reach a saturation state, which is a characteristic property for ferromagnetic substances, called saturation magnetization (M_S). When the applied field is gradually reduced to zero, the magnetic moments remain aligned. This residual magnetization (y-intercept) is called the remnant magnetization (M_R), and this can be neutralized to zero when an external field is applied in the opposite direction. The magnitude of the neutralization field is called the coercivity (H_C). The saturation magnetization can be achieved again finally in the opposite direction as the magnetic field in that direction increases.

1.3.4 Antiferromagnetism

Opposite of the case for ferromagnetism, in an antiferromagnet, the tendency of spins is the equivalent spins of neighboring valence electrons point in opposite directions.

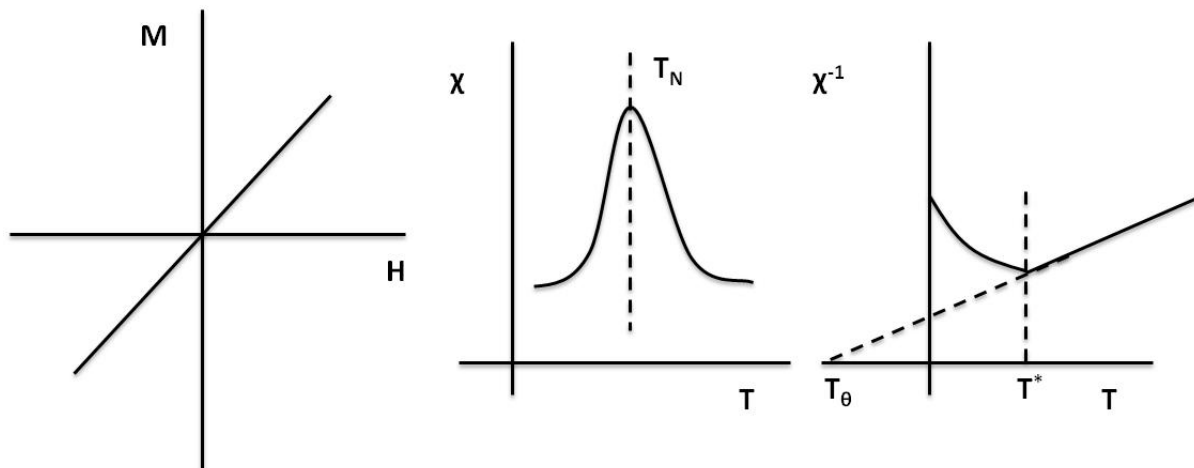


Figure 1.8 Typical magnetic properties for antiferromagnetic materials: (A) M vs H curve, (B) χ vs T curve and (C) Inverse χ vs T curve.

Antiferromagnets exhibit a very small susceptibility when applying an external magnetic field, usually on the order of $0\sim 10^{-2}$ and have no spontaneous moment in the absence of a field. Figure 1.6 depicts the typical graphs for the response of the magnetization under the applied field. A parameter called the Néel Temperature (T_N) is used to show the thermal effect that transforms antiferromagnets into paramagnets. In this occasion, Curie-Weiss Law will apply because the Curie Law does not take into account of the magnetic moment interactions between atoms. Ideally, $T_\theta = T_N$.

1.3.5 Ferrimagnetism

Similar to antiferromagnetism, the spin alignment in ferrimagnets are opposite between neighbors but have different magnitudes, which means the spontaneous moment of ferrimagnets is not zero and these materials behave similar to ferromagnets. This arises because in certain geometrical arrangements, there is a larger magnetic moment from a sublattice of electrons pointing in one direction than from another sublattice where they point in another direction. A well known example is Fe_3O_4 , which adopts the inverse spinel structure in which all Fe^{2+} ions occupy half of the octahedral sites and Fe^{3+} are split evenly across the remaining octahedral sites and the tetrahedral sites. The spins of the octahedral sites, including Fe^{2+} and Fe^{3+} , are colinear but the Fe^{3+} ions in the tetrahedral sites are anti-parallel to the Fe^{3+} ions on the octahedral sites. The net magnetism contributed by the remnant Fe^{2+} ions makes Fe_3O_4 a permanent magnet which exhibits all the characteristics of ferromagnetism such as hysteresis, Curie temperature, coercivity etc. but with a lower spontaneous moment.

1.4 Magnetism in Nanomaterials

The magnetic moments of atoms in a ferromagnetic or ferrimagnetic material cause them to behave like 'tiny' permanent magnets. These moments stick together and are aligned into small regions of more or less alignment called magnetic domains or Weiss domains.

When the size of the magnetic materials is decreased to the nanoscale and becomes comparable to the size of the magnetic domains, the magnet will behave like a single magnetic spin that is subject to Brownian motion. The magnetic susceptibility to a magnetic field is qualitatively similar to the response of a paramagnetic, but much larger because in sufficiently small nanomaterials, magnetization can randomly flip under the influence of temperature. In bulk magnets, magnetic domains stick together and all spins point along the same direction. The domains are separated by domain walls, which are transitions between different magnetic moments. Thus, the domain wall represents a gradual reorientation of individual moments across a finite distance usually around 100-150 atoms. For bulk magnetic materials, the reorientation of moment in response to an applied field occurs by the motions of the domain walls, in a process called domain wall migration. However, for sufficiently small magnets, like nanoparticles, each particle behaves like a single domain because the formation of domain wall is not thermodynamically favorable and is easily overcome by thermal energy. The process of reorientation occurs through the coherent rotation of all the spins in the domain (particle). When the size is further decreased, the spins can fluctuate due to thermal energy and the magnetic behavior becomes superparamagnetic. In superparamagnetic nanoparticles, the magnetic field dominates the orientation of the spins and hysteresis is no longer observed, which makes them like paramagnetic materials (zero M_R) at zero applied field but also like ferromagnets (high

M_S). The illustration of the changes that occur between bulk materials (multiple domains) and nanoparticles (single domains) under applied field are shown in Figure 1.9.

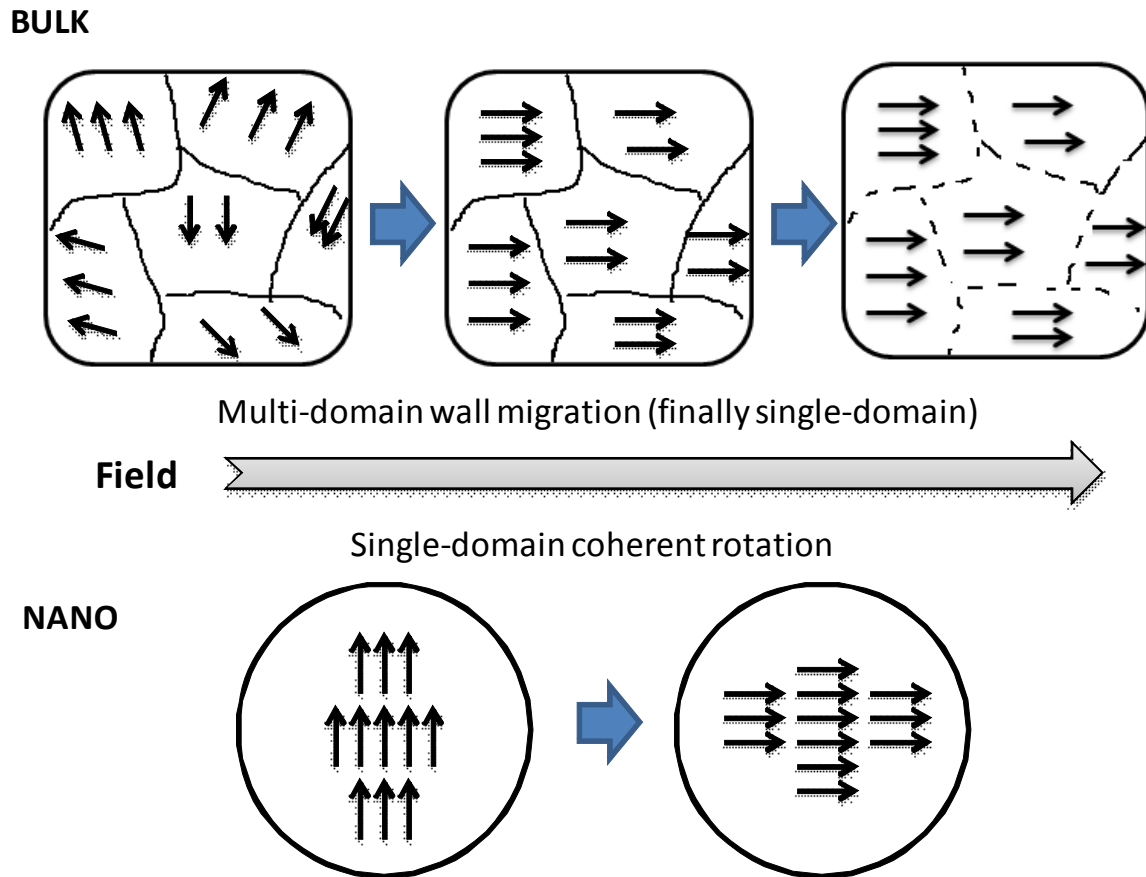


Figure 1.9 Comparison of spin alignment behavior between bulk (multidomain) and nanomaterials (single domain) along the direction of the applied field.

The magnetic behavior as demonstrated by the M vs H curve, for ferromagnetic, superparamagnetic and paramagnetic materials is shown in Figure 1.10. The temperature above which the ferromagnet become superparamagnetic for nanoparticles is called the blocking temperature (T_b), which is a function of the size of the nanoparticles and the measurement time. T_c can be measured by plotting magnetization under an applied field on a sample cooled in the field (field cooled magnetization, FC) and T_b can be obtained by the zero-field-cooled magnetization (ZFC, no external field), as shown in Figure 1.11. In the ZFC curve measurement, the sample is first cooled down at very low temperature (~ 10 K) in the absence of a magnetic field at which point the magnetic moments are frozen at zero. Then the sample is gradually heated under a low magnetic field. With the increase of temperature, the low applied field starts to activate the alignment of the spins because thermomovement is increased. At a temperature (T_b), the thermo-movement becomes dominant and overwhelms the spin alignment energy, which causes the moments to orient randomly and the spontaneous magnetization drop to zero. At T_c , the sample becomes paramagnetic. The regime between T_b and T_c is the superparamagnetic regime.

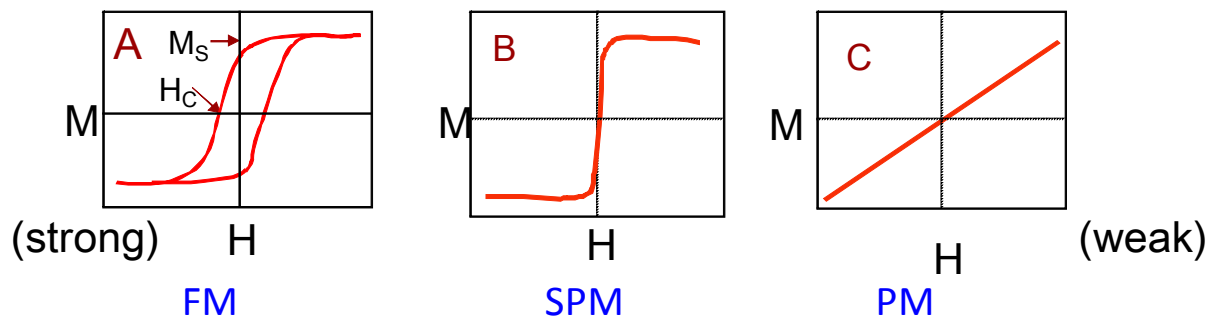


Figure 1.10 Comparison of magnetic behaviors in magnetization vs applied field (moving from strong field to weak field, left to right) for (A) ferromagnets (FM), (B) superparamagnets (SPM) and (C) paramagnets (PM).

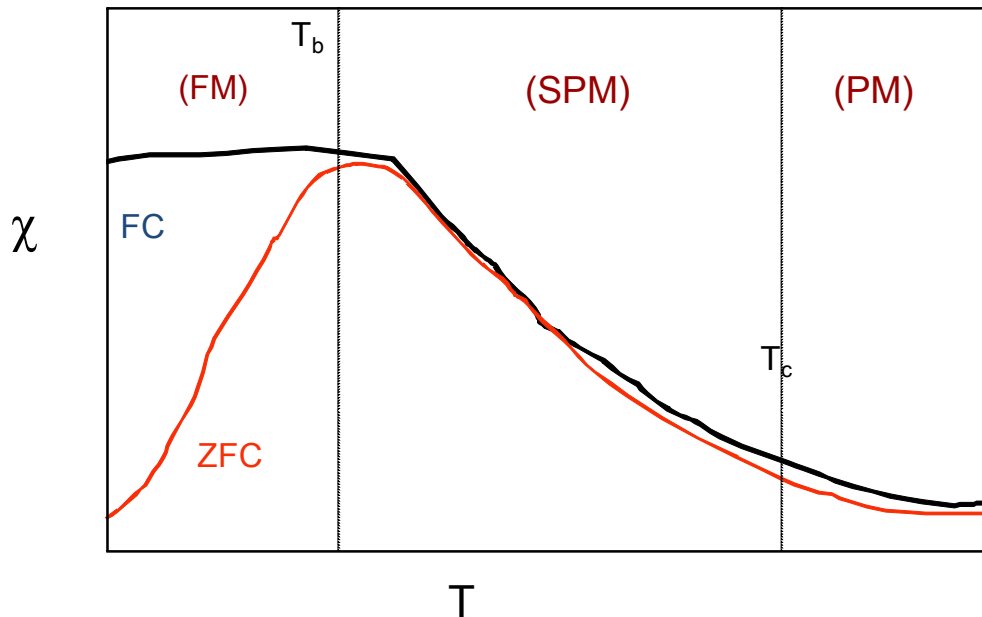


Figure 1.11 A typical FC/ZFC curve for a nano-ferromagnet showing the blocking temperature (T_b) and the Curie temperature (T_c). FM, SPM and PM indicate ferromagnetic region, superparamagnetic region and paramagnetic region, respectively.

1.5 Transition metal pnictide materials

Transition metal pnictide (phosphide, arsenide and antimonide) materials have been studied because of their potential in magnetic, semiconducting, optical and catalytic applications.³⁷ The physical properties of this class of materials depend on their composition and structures. Table 1.1 lists the known properties for a selection of binary pnictide materials with varied composition.³⁷⁻³⁸ Compared to the metal phosphides, which have been studied for years because of their potential use in hydrodesulfurization (HDS) catalysis (e.g. Ni_2P), and ferromagnetic properties (MnP , Fe_2P). Research on metal arsenide is relatively rare, despite their potential application in compact displays, satellite TV receivers³⁹ and optical fibers.⁴⁰ For example, iron arsenides have long been studied due to their importance in thermoelectric

semiconductors, secondary high-temperature batteries and catalysis.⁴¹ Recently, a series of FeAs-based superconductors have been synthesized, with the highest critical temperature reaching up to 39 K.⁴² In the transition metal antimonides and bismuthides, MnBi and MnSb are important materials showing magneto-optical properties;⁴³ FeSb nanoparticles were recent found to show ferromagnetic properties;⁴⁴ FeSb₂ and CoSb₃ are the new research focus for the thermoelectrical materials.⁴⁵

Table 1.1 Transition metal pnictide materials and associated properties

Property	Transition metal pnictide
Ferromagnetic	MnP ($T_c = 292$ K), MnAs ($T_c = 315$ K), MnSb ($T_c = 587$ K), MnBi ($T_c = 628$ K, magneto-optical activity), Fe ₃ P ($T_c = 716$ K), Fe ₂ P ($T_c = 217$ K)
Antiferromagnetic	FeP ($T_N = 115$ K), Fe ₂ As, Mn ₂ As
Semiconducting	FeP ₂ , CoP ₃ , NiP ₂ , RhP ₂
Catalytic Activity	Co ₂ P, CoP, Ni ₁₂ P ₅ , Ni ₂ P, MoP, Rh ₂ P, Pd ₅ P ₂ , WP
Thermoelectric	FeSb ₂ , CoSb ₃
Superconducting	NiP ₂ , Mo ₃ P, W ₃ P,

1.6 Transition metal pnictide nanoparticles

As previously discussed, nanoscale materials exhibit size and shape tunable physical properties (electronic, magnetic, catalytic, etc.), making their study of considerable interest. However, despite a good understanding of the bulk properties of binary pnictides, little is known of their nanoscale properties, due in part to a lack of methodologies that enable size control on this scale. Hence, recent attention has turned to the synthesis of nanoscale forms of transition metal pnictides. Methods have been developed for the synthesis of metal pnictide nanoparticles. The solvothermal method, which has been popular for making nanostructures, has been used by Qian and coworker to prepare a variety of transition metal pnictide nanomaterials. They successfully reported phases like FeP, Ni₂P, Co₂P, Cu₃P, NiAs, CoP, CoAs, FeAs and NiSb by using this method.^{41a, 46} However, these solvothermal reactions tend to produce polydisperse samples without size and morphology control. Additionally, the As precursors they use, including alkylarsines or arsenic compounds reacting with NaBH₄, are very toxic because As is a carcinogen. The sol-gel method, using a silica xerogel matrix, has also been employed to control the size of the metal pnictide nanoparticles. Lukehart and coworkers prepared metal containing compounds with phosphine and alkoxysilyl functional groups to form silica xerogel matrices that upon thermal treatment under reducing conditions yield a series of crystalline metal phosphides nanoparticles embedded within a silica matrix. However, the same problem is encountered as with the solvothermal method because the products are still polydisperse. Furthermore, the silica xerogel encapsulation limits the further application and manipulation of these metal phosphides.

Our lab is a pioneer in the formation of disperse transition metal pnictide nanoparticles with good size and dispersity control using the SPAP method.⁴⁷ As early as 2003, Perera et al used organometallic and phosphine precursors to synthesize FeP, and later MnP, nanoparticles.

For the synthesis of FeP nanoparticles, tri-octylphosphine oxide (TOPO) dodecylamine (DDA), myristic acid (MA) and hexylphosphonic acid (HPA) were heated at 240-320 °C, and iron (III) acetylacetonate and tris-trimethylsilyl phosphine ($P(\text{SiMe}_3)_3$) (-SiMe₃ is abbreviated as TMS) were introduced, subsequently yielding phase-pure spherical nanoparticles of FeP with an average size of 4.65 ± 0.74 nm. Highly crystalline spherical nanoparticles of MnP nanoparticles can be obtained by reacting manganese carbonyl ($\text{Mn}_2(\text{CO})_{10}$) and $P(\text{TMS})_3$ at a temperature higher than 220 °C in a similar manner. Subsequently, trioctylphosphine (TOP) was found to be an effective replacement for pyrophoric phosphines such as $P(\text{TMS})_3$, resulting in safer and more economical syntheses. The Schaak group has used trioctylphosphine as a general phosphorus source for low temperature conversion of metal nanoparticles into metal phosphides, producing highly crystalline product.^{33b} Recently, Muthuswamy et al in our lab also explored the synthesis of metal (Fe and Ni) phosphides with different atomic ratios and morphologies by conversion of metal nanoparticles.⁴⁸ The development and success in the synthesis of high quality metal phosphide nanoparticles is encouraging as a similar method should be applicable to metal arsenide nanoparticle synthesis. Indeed, similar reactions have been explored for making III-V quantum dots (main group metal arsenide) such as GaAs or InAs nanocrystals. Peng and coworkers successfully synthesized high quality InAs nanocrystals by injecting $\text{As}(\text{TMS})_3$ into preheated InCl_3 at 270 °C with octadecene (ODE) as a noncoordinating solvent and different coordinating ligands such as lauric, myristic, palmitic and stearic acids.^{41b} Similar reactions with GaCl_3 and $\text{As}(\text{NMe}_2)_3$ were employed by Malik to form GaAs nanoparticles.⁴⁹ However, transition metal arsenide nanoparticles remain largely unexplored.

1.8 MnAs

Among transition metal arsenides, bulk MnAs has been extensively studied for a long time due to its interesting magnetic properties and potential applications in information storage and energy devices.⁵⁰ Bulk MnAs has a magneto-structural phase transition in which a first order magnetic transition from a ferromagnet to a paramagnet and structural transition from the hexagonal α phase (NiAs-type) to the orthorhombic β phase (MnP-type) occurs at 313 K.⁵¹ At higher temperature ($T = 399$ K), a second-order phase transition occurs in which the β reverts back to the α phase structure, as shown in Figure 1.12.⁵¹ The first order transition and associated temperature hysteresis can be exploited for technological applications. For example, magneto-elastic effects are useful for transducers,⁵² and magneto-caloric properties can be applied in magnetic refrigeration devices.⁵³ The temperature of the first-order phase transition is sensitively influenced by the bond distances between Mn-Mn and Mn-As,⁵⁴ and can be tuned by external pressure or internal chemical pressure (i.e. by doping).⁵⁵ As early as 1967, Goodenough and co-workers found that increasing external pressure could cause a decrease of the transition temperature, whereas reduced pressure could increase the transition temperature. The changes in

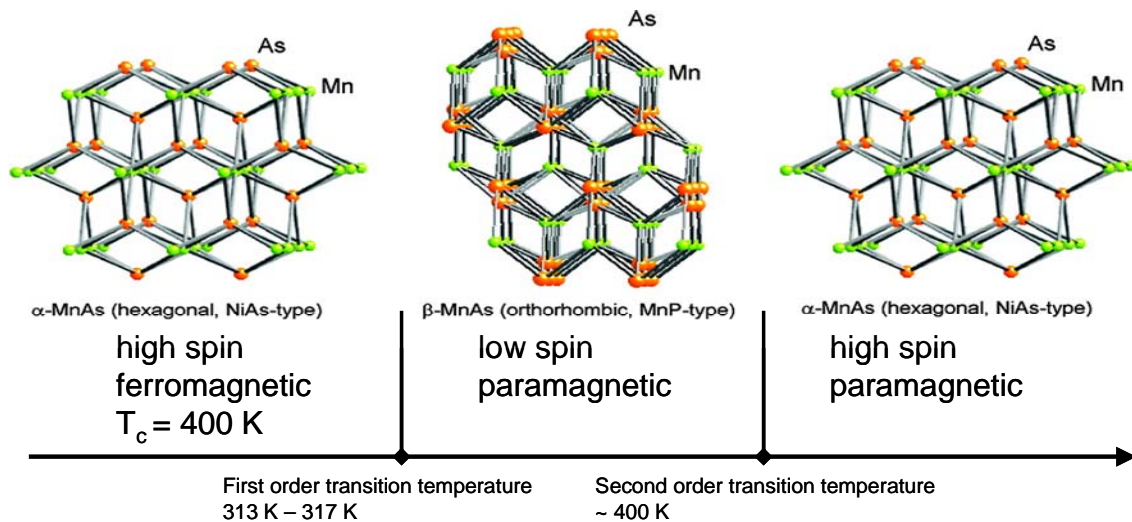


Figure 1.12 The magneto-structural transition in bulk MnAs

transition temperature are due to the lattice compression or expansion, respectively.⁵⁴ MnAs is a good candidate for room temperature magnetic refrigeration applications because of its T_c near room temperature. For practical applications, expanding hysteresis in the magnetism as a function of temperature (M-T) is desired and can be achieved by doping in other transition metal atoms. Recently, De Campos and co-workers partially doped Fe in MnAs and they found that the M-T hysteresis can extend from 285 K to 310 K, depending on the amount of Fe doped.⁵³ Similarly, Sun et al. observed a giant magneto-caloric effect near room temperature by doping 0.6%-1% Cr in MnAs, because the transition temperature on cooling is even reduced to 265 K and the hysteresis is significantly enlarged after doping.⁵⁶ Despite the fact that there is a large lattice mismatch (30%) between MnAs and the semiconductor (GaAs),^{55, 57} MnAs is also an attractive candidate for spintronic technologies when the ferromagnetic component is coupled to semiconductors such as GaAs, InP, or InAs. These combination ferromagnet/semiconductor (FM/S) devices are useful for LED or data storage devices.

Research on nanoscale MnAs is focused on epitaxially grown MnAs particles or disks on semiconducting thin films⁵⁸ or nanowires.^{57b} However, these MnAs nanomaterials are subject to external pressure due to the lattice strain from the substrate. In order to discern the intrinsic magnetic and structural properties of discrete unstrained MnAs nanoparticles, our group synthesized MnAs nanoparticles with sizes from 9-23 nm in solution by reaction of dimanganesedecacarbonyl ($Mn_2(CO)_{10}$) and triphenylarsine oxide ($(C_6H_5)_3As=O$) in coordinating solvents at temperatures ranging from 523-603 K.^{38d} Intriguingly, either the α or β phase can be isolated at room temperature, depending on the synthesis temperature employed and whether the synthesis was conducted by slow heating (type-A MnAs nanoparticles) or rapid injection (type-B MnAs nanoparticles). Magnetic measurements of the type-A MnAs

nanoparticles reveal a transition at 315 K. However, temperature dependent X-ray diffraction suggests that in type-A MnAs nanoparticles, there is no structural phase transition from α to β , even when the temperature is increased up to 343 K; this behavior is distinct from bulk materials, where the magneto-structural phase transition is observed at 313-317 K. Moreover, the type-B MnAs nanoparticles also show ferromagnetic behavior with a phase transition near 315 K, which is distinct from bulk paramagnetic β -MnAs, but remarkably similar to type-A MnAs nanoparticles. An additional finding is that metastable type-B MnAs nanoparticles will convert from β phase to the thermodynamically stable α phase over time at room temperature.

1.9 Thesis statement

Overall, the dissertation research established methodologies for preparation of transition metal arsenides as discrete nanoparticles and evaluated their size and composition dependant properties. The dissertation research pursued three objectives.

- (1) The first objective was focused on relation of the synthetic method for MnAs nanoparticles (type-A vs type B) to magnetic and structural properties. This goal was achieved by the synthesis of different room temperature stable phases of MnAs nanoparticles (α or β) by employing slow heating or rapid injection methodologies, respectively. The size was controlled by the precursor concentration and reaction time. The temperature dependent Pair Distribution Function (PDF) technique and magnetic susceptibility measurements were employed to evaluate intrinsic magnetic and structural properties of the nanoparticles, and

the results then were compared to a representative bulk sample. The results of pursuing this objective will be presented in Chapter 3.

(2) A second objective was to extend our synthesis of phase pure, discrete and monodisperse MnAs nanoparticles to produce nanoscale samples of varying sizes and discern the relationships among particle size, magnetic properties and structural phase changes in MnAs nanoparticles in the absence of epitaxially imposed strain. Low and high temperature processing as well as aging (at room temperature) was employed in order to study the structural transformation of the type-B MnAs nanoparticles. Temperature dependent PXRD studies were performed to assess the reversibility of the $\beta \rightarrow \alpha$ transition. These data were correlated with detailed magnetic susceptibility measurements.

(3) A third objective is to establish a general method for the synthesis of monodisperse metal arsenide nanoparticles of Mn, Fe, Co and Ni in order to provide general and rational synthetic approaches to transition metal arsenide nanoparticles. Direct conversion of metal nanoparticles into metal arsenide nanoparticles in organic solvents do not enable the size and monodispersity to be controlled. However, a new SPAP method involving injection of metal carbonyl into preheated arsenic precursors showed improved results. The consequences of pursuing this objective will be presented in Chapter 5.

In addition to these research chapters, Chapter 2 will present experimental methods and Chapter 6 will describe the conclusions of the dissertation research and provide prospectus.

CHAPTER 2

Experimental and Materials Characterization Techniques

2.1 General Information

Transition metal arsenide nanoparticles are synthesized by arrested precipitation reactions under inert atmosphere (Ar). Schlenk lines and glove boxes are required for the synthesis to protect the materials against oxidation from air and reactions with moisture. The structure and properties of the synthesized nanoparticles were studied by several materials characterization methods including Powder X-ray Diffraction (XRD), Transmission Electron Microscopy (TEM), Energy Dispersive Spectroscopy (EDS), and magnetic susceptibility. In addition, to study the metastability and the magneto-structural phase transition in MnAs nanoparticles, the atomic Pair-Distribution Function (PDF) method, Differential Scanning Calorimetry (DSC) and T-dependent XRD were also employed. This chapter will describe the general experimental methods for making transition metal arsenide nanoparticles, followed by a detailed discussion of the relevant characterization techniques.

2.2 Chemicals

Manganese carbonyl (98%), iron carbonyl (99%), cobalt carbonyl (95%), bis(cyclooctadiene)nickel(0), triphenylarsine oxide (97%), 1-octadecene (90%, tech grade), and trioctylphosphine oxide (90%, tech grade) were purchased from Sigma Aldrich Inc.

The purification of trioctylphosphine (TOPO) followed a reported procedure by Buhro and coworkers. 500 g of 90% TOPO was put into a round bottom flask connected to a Schlenk line and preheated to 150 °C. Once all the solid TOPO melted, the temperature was gradually increased by 20 °C per 10 mins. At about 250 °C, the first component will be distilled out followed by a second component at 300 °C. The second component was collected and transferred to a beaker. The as-distilled TOPO was heated and melted in acetonitrile at 70 °C and recrystallized by cooling back to room temperature. The final product were dried and collected and dried by keeping in the hood.

2.3 Synthesis and Characterization Techniques

2.3.1 Inert Atmosphere Handling

Inert atmosphere systems in the lab include glove boxes and Schlenk lines, which are used for handling air-sensitive chemicals and preparing reactions, respectively. A typical glove

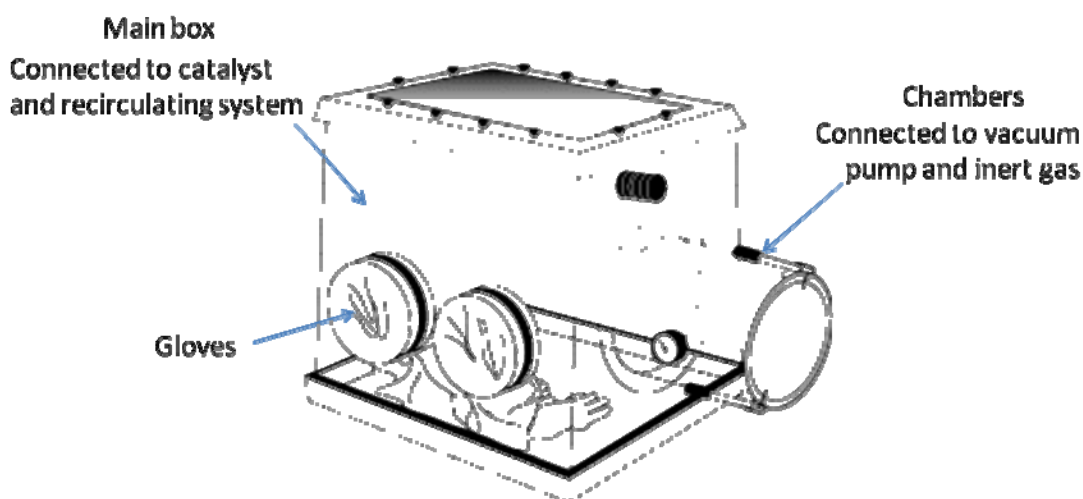


Figure 2.1 A typical schematic diagram for a glove box (original figure adapted from Ref. 96)

box, shown in Figure 2.1,⁵⁹ is essential for storing and handling air/moisture sensitive chemicals. The main parts of the glove box include a tightly sealed metal box with a plastic front window for making observations, a pair of standard butyl gloves attached to the plastic window for handling and preparing the chemicals inside, a chamber with vacuum and purge valves connected to the side of the main box, an inert gas cylinder (argon or nitrogen) for purging and a vacuum pump for evacuation. The inert environment inside the main box is maintained a continuous circulation of the inert gas over a catalyst, usually Cu/Al₂O₃, to remove oxygen, and molecular sieves to remove moisture. The catalyst can be regenerated by high temperature reduction with a hydrogen flow followed by evacuation. Some glove boxes are equipped with a small refrigerator for storing volatile or particularly sensitive chemicals that needs low temperature. A photohelic pressure gauge is used to control the pressure inside the box. The glove box should always be kept at positive pressure inside to avoid air diffusing in through leaks. In this dissertation research, the chemicals are stored and handled inside the VAC-HE493 glove box outfitted with two antechambers and a refrigerator working at -30 °C.

Once the chemicals are prepared and scaled in a Schlenk flask inside the glove box, they will be transferred and reacted on a Schlenk line. A Schlenk line is a common lab glass apparatus consisting of a dual manifold with several ports. One of the manifolds is connected to the vacuum pump, while the other is connected to a source of purified inert gas. An oil bubbler is used for each port of the inert gas to prevent backflow of air, while a cold trap is connect between the vacuum line and the vacuum pump to trap the solvent vapors and gaseous reaction products. Stopcocks enable vacuum or inert gas to be selected. The Schlenk flask containing the reagents is attached to a port for degassing and purging processes. A diagram of a typical Schlenk line is shown in Figure 2.2.⁶⁰

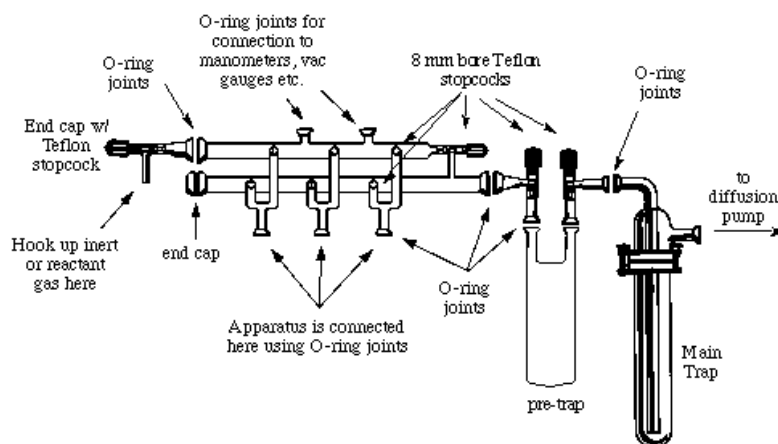


Figure 2.2 An illustration of a typical Schlenk Line. (Picture adapted from Ref. 97)

2.3.2 Power X-Ray Diffraction (PXRD)

When X-rays interact with the lattice of a crystalline phase, a diffraction pattern is observed. The X-ray diffraction pattern is unique for different crystalline materials, which thus makes the XRD for a pure material like a “fingerprint” of a material.⁶¹ Currently, XRD patterns for about 50,000 inorganic and 25,000 organic crystalline phases have been collected and stored as standards. Search/match procedures can be used to identify the components in a sample characterized by powder XRD.

The X-rays are generated inside an X-ray tube when a metal target (such as Cu or Ni) is impacted by a high energy electron beam. A typical schematic diagram for an X-ray generating tube is shown in Figure 2.3 and includes three main components: (1) an electron source; (2) a high voltage electrode system to accelerate the electrons and (3) a metal target. Electrons are generated by passing a current through the tungsten filament and then accelerated directly across the X-ray tube from cathode to anode by a acceleration voltage. X-rays are then generated from the collision of the high energy electron beams with the metal (Cu or Ni) target. Transparent beryllium windows enable X-rays to pass through. Cold water flow is used to cool the metal target to prevent melting from the heat generated by the high energy electrons. A rotating anode makes X-ray tube more efficient because more surface of the metal target will be exposed. This

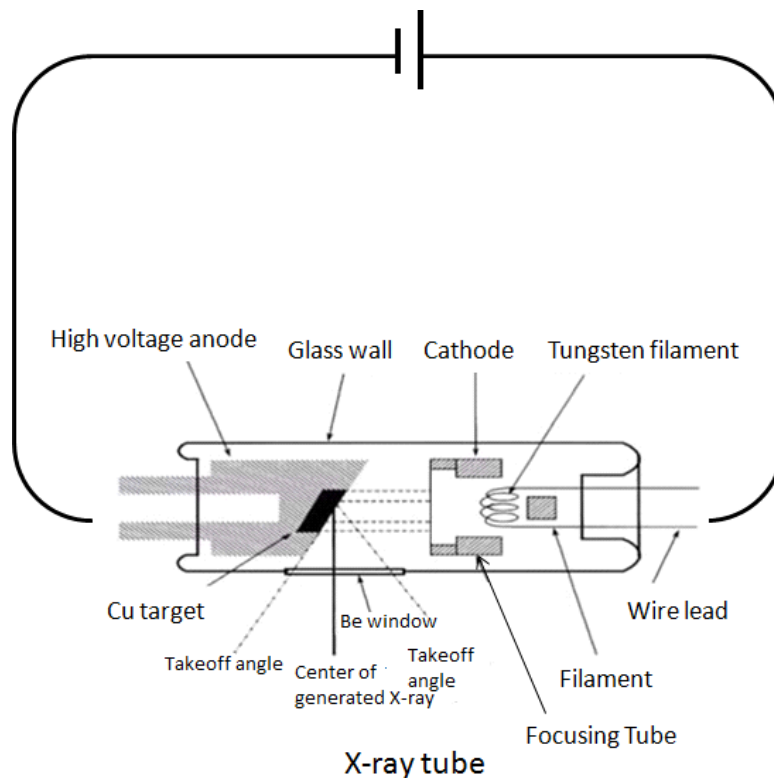


Figure 2.3 A schematic diagram depicting X-ray generation inside the X-ray tube (adapted from Cullity, see ref. 98).

enables the use of higher currents, and thus generation of a larger X-ray flux.

There are two different components of X-ray radiation generated inside the X-ray tube: (1) white radiation, which consists of a continuous spectrum of wavelengths; and (2) characteristic radiation. White radiation occurs due to the loss of energy of the electrons by collision with the atom via multiple events, part of which is converted into electromagnetic waves. Depending on the metal anode, when the energy of the accelerated electrons overcomes a certain threshold value, characteristic radiation is emitted. Characteristic radiation consists of one or more monochromatic X-rays arise from ionization of the target metal atoms, as shown in Figure 2.4,⁶¹⁻⁶² taking Cu as an example. When the Cu target is struck by the accelerated electrons, some of

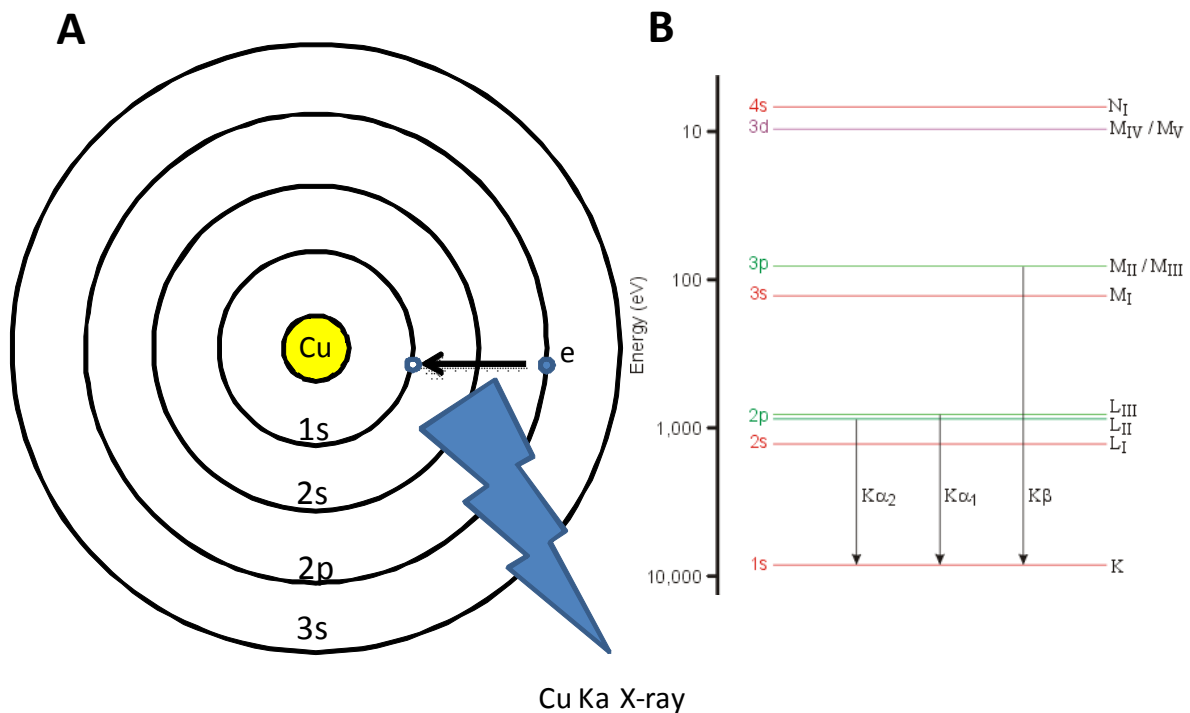


Figure 2.4 Illustration of (A) Cu K α X-ray generated from electron transition from 2p to 1s (1s vacancy is caused by ionization) (B) different types of X-rays generated by the X-ray source (adapted from West, see Ref. 99). K α_1 and K α_2 correspond to two different spin states for the 2p electron.

the Cu 1s electrons (in the K shell) will be ionized, which results in an electron from a higher atomic level (2p or 3p orbitals) dropping into the inner vacant orbital and the concomitant emission of an X-ray photon characterized by the difference in energy between the two orbitals. For the example shown in Figure 2.4(B), the $2p \rightarrow 1s$ orbital transition is called the K_α transition with wavelength 1.5418 Å, while the K_β (1.3922 Å) comes from the $3p \rightarrow 1s$ transition. For better resolution, a monochromatic filter is used to pass only K_α radiation for diffraction with the sample.

In crystalline solids, the atoms are arranged in regular repeating structures, with the smallest volume element (the unit cell) repeated in three dimensions. The oscillation of an electron in an electromagnetic field will have the same frequency as the applied field. Thus, when an X-ray beam hits the atoms of the sample, the electrons around those atoms will oscillate with the same frequency as the beam. In most directions, the interference of the oscillations from one atom to the next can be considered destructive, which means there is no energy leaving the solid sample and the combining waves are out of phase. However, because the atoms in a crystalline solid are regularly arranged, in a few directions, the interference will be constructive. Then the waves are in phase and there will be X-ray beams leaving the sample in specific directions, as shown in Figure 2.5.⁶² Assume an X-ray beam hits a pair of parallel planes (P1 and P2) of a crystalline solid, separated by the interplanar spacing d . There are two parallel X-ray beams making an angle with the planes, one of which is A and the other is B, while the diffracted beams are A' and B', respectively. If A' and B' are in phase, then the reflected beam of maximum intensity will result. Thus, the difference between A to A' and B to B' in the path length must be an integer number of wavelengths. Bragg's law can be used to express this mathematical relationship as shown in Equation 2-1.

$$2d\sin\theta = n\lambda \quad (2.1)$$

Bragg's law indicates that for an X-ray beam with a certain wavelength (depending on the target material) and a certain plane spacing, the angle for the incoming beam should obey a strict condition, and from the θ that meets this condition, we can find the corresponding d value, which is directly related to the lattice parameters (a , b , c) and the structure plane parameters (h , k , l). However, the intensity of the reflected beam is determined by the distribution of the electrons in the unit cell. Therefore, those planes with high electron density will give strong reflection peaks while the planes with low electron density will show weak intensity. Depending on the arrangement of atoms within and between planes, strong peaks can combine destructively, resulting in low- or zero-intensity reflections.

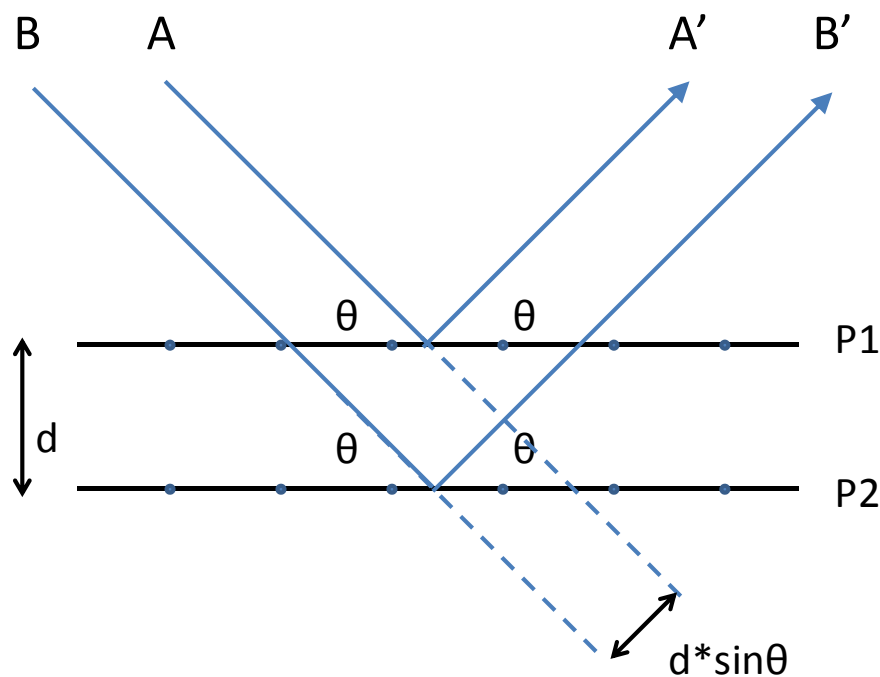


Figure 2.5 Illustration of Bragg's Law (adapted from West, see Ref. 99)

For powder or polycrystalline samples, which have crystallites in every possible orientation, XRD can be used for “fingerprint identification”. In the characterization process, a detector (movable scintillation detector (MSD) or static charge-coupled device (CCD)) is used to record the diffracted X-rays. The signals are then manipulated into a 1-D plot where the intensities of the X-ray reflections are plotted against 2θ . These plots can then be compared to reference plots for known materials.

For nanoparticles, the PXRD patterns differ relative to bulk materials due to the fact that the crystallites in nanoparticles consist of many fewer lattice planes. Thus, destructive cancelling of scattering is incomplete at angles near the 2θ mandated by Bragg’s Law, resulting in the observed reflections becoming broader relative to material with larger (i.e. micron-scale) crystallites. Peak broadening is inversely proportional to the nanoparticle size, and thus the full width at half maximum of the peak (FWHM), can be used to calculate crystallite size (B) using the Scherrer Formula,⁶³ as shown in Equation 2.2.

$$B = \frac{0.9\lambda}{(FWHM) \cos \theta} \quad (2.2)$$

In this dissertation research, the instrument used for primary structure identification in the dissertation research is a Rigaku RU200B with a 12 kW rotating anode Cu $K\alpha_1$ (1.5418 Å in wavelength) radiation. Powder nanoparticle samples were affixed to a zero-background quartz-holder with a tiny amount of vacuum grease. Diffraction data were collected using 40 kV and 150 mA working conditions in the 2-Theta range 20-70 degrees. The diffraction patterns were

compared to the Powder Diffraction File (PDF) database (release 2000) from the International Center for Diffraction Data (ICDD) to determine the phase.

T-dependent XRD data in the 2-Theta range 47-53 degrees were collected on a PANalytical X'Pert Pro diffractometer with temperature variation using the Scintag XDS-2000 accessory equipped with a Moxtek detector and an Anton Parr stage. Liquid nitrogen was used to cool the sample and a platinum heat strip was used to heat the sample. The temperature dependent study was performed in the range between -150 °C and 50 °C.

2.3.3 The Total Scattering and Atomic Pair Distribution Functional (PDF) Method

Modern solid state materials such as nanoparticles are often disordered or ordered over only a short range, which means some aspect of the structure is not the same as the average structure.⁶⁴ In nanoparticles, the concept of crystal does not hold and a nanocrystal cannot be simply considered as an approximation to infinite periodicity. Although standard crystallographic methods like PXRD are still useful for the characterization of these materials, it is sometimes necessary to go beyond Bragg's Equation. A new approach, which treats both the Bragg diffraction and the scattering, called the total scattering method, is now well developed and allows people to explore the interaction between neighboring atoms in a solid material. This comprehensive method detects the total reciprocal space information of the material, which then can be translated by the Fourier transformation method. This is known as pair distribution function (PDF) analysis.⁶⁵

In the dissertation research, the total scattering powder diffraction was carried at the 11-ID-B beam-line at the Advanced Photon Source (APS) at Argonne National Laboratory for both bulk and nanoparticles of MnAs. This beam-line is dedicated to PDF measurements and employs a Perkin Elmer (PE) amorphous silicon area detector. The monochromator is Si(511) and the photon flux is 1×10^{11} per sec @ 58 keV. Data were collected and analyzed in collaboration with Simon Billinge (Michigan State University/Columbia University) and his group.

2.3.4 Transmission Electron Microscopy

Because of the extremely short de Broglie wavelength of electrons,⁶⁶ Transmission Electron Microscopy (TEM) is capable of significantly higher resolution than the optical microscope, making it ideal for characterization nano-structure. Max Knoll and Ernst Ruska built the first TEM instrument in 1931. Compared to light, electrons were selected and preferred for several reasons.⁶⁷ First, the wavelength of electrons can be tens of thousands times small than a photon at the same energy. Second, due to the charged nature of electrons, the wavelength of the electrons can be tuned based on the acceleration voltage and the electron beams can be controlled by the use of a magnetic field. Finally, electrons scatter strongly because they interact with both the nucleus and the electrons of the scattering atoms when they interact with the specimen.

TEM is a major analysis tool for nanomaterials characterizations. For example, the chemical composition of specimen can be visualized and identified on the sub-nanometer to micrometer range; the size, shape and morphology can be directly obtained; and lattice fringes

and crystalline facets can be imaged or electron diffraction patterns obtained and used to identify the crystal structure or the growth direction of the anisotropic nanostructure.

Besides transmission and diffraction, many other experiments can be performed in the TEM. Figure 2.6 and Table 2.1 depicts the processes that occur and related applications.⁶⁸ For example, energy dispersive spectroscopy (EDS) can provide information on the chemical composition; electron energy loss spectroscopy (EELS) can be used to identify the light elements in materials; and scanning transmission electron microscopy (STEM) when coupled with EDS can be used to build an elemental map along a chosen direction of the specimen.

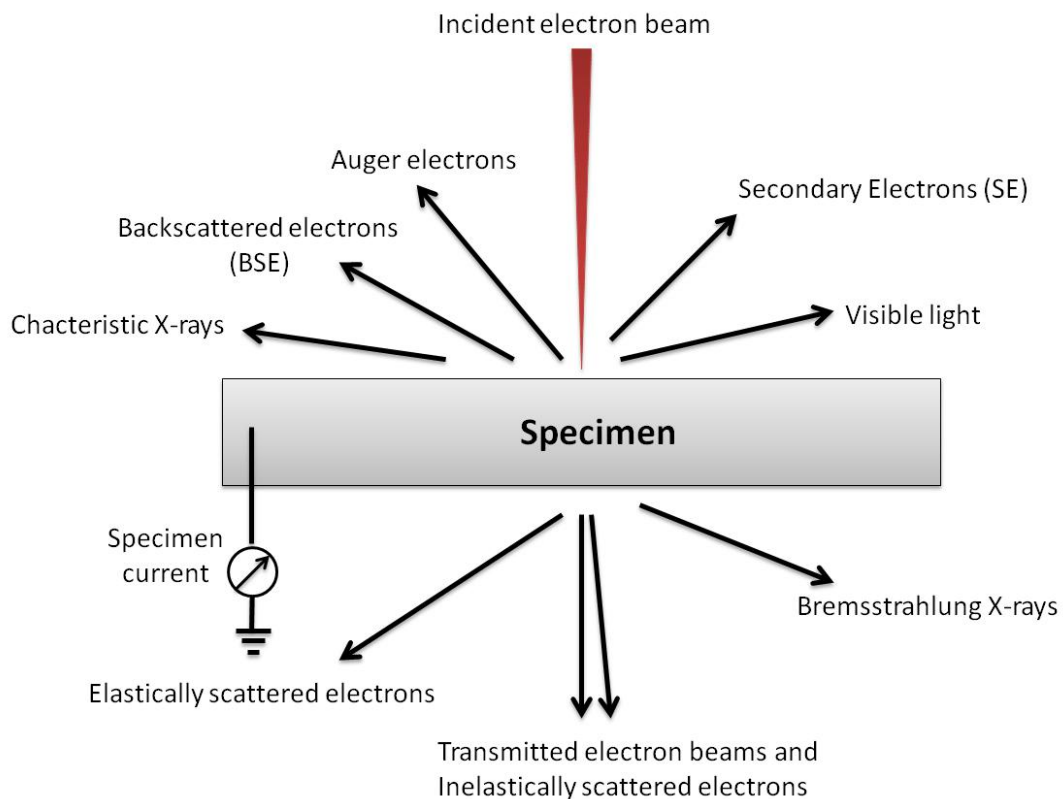


Figure 2.6 Electronic excitations occurring after a specimen is hit by a high energy electron beam in an electron microscope (adapted from Williams, Ref. 107)

Table 2.1 Characterization techniques derived from the radiation generated from the interaction between a high energy electron beam and a specimen

Radiation Type	Corresponding Application
Auger electrons	Auger Electron Spectroscopy (AES)
Secondary electrons	Scanning Electron Microscopy (SEM)
Backscattered electrons	Scanning Electron Microscopy (SEM)
Inelastically scattered electrons	Transmission Electron Microscopy (TEM) Electron Diffraction (ED)
Transmitted Electrons	Transmission Electron Microscopy (TEM)
Elastically Scattered electrons	Transmission Electron Microscopy (TEM) Electron Diffraction (ED) Scanning Transmission Electron Microscopy (STEM) Electron Energy Loss Spectroscopy (EELS)
Characteristic X-rays	Energy Dispersive Spectroscopy (EDS)

Figure 2.7 shows a general schematic diagram of a transmission electron microscope.⁶⁸ Two types of electron sources are used in TEM: one is called a thermionic source, in which a tungsten (W) or lanthanum hexaboride (LaB₆) filament is heated; the other is a field emission source, in which fine tungsten needles are the field emitters. The majority of TEMs use a thermionic source. However, the electrons generated from thermionic sources are less monochromatic, and the W filament or LaB₆ crystals will gradually evaporate or oxidize, which make their life more limited. For field-emission sources, a very strong electronic field ($\sim 10^9 \text{ Vm}^{-1}$) is used to extract the electrons from the tungsten needles. The temperature needed is much lower than that for the thermionic source, which makes the lifetime of the filament longer. The electrons generated from the field emission source are monochromatic and the source brightness is much higher than that of thermionic sources, which makes the field emission source popular

for the best high-resolution imaging and analytical performance. However, the field emission source requires a more rigorous high vacuum environment.

Generally, the operating voltage for accelerating the generated electrons is between 100 kV and 400 kV, and determines the wavelength of the generated electrons. The relationship between the voltage (energy) of the electrons and their wavelength is shown in Equation 2.4, where m_0 is the mass of electron, E is the kinetic energy (in electron volts), h is Planck's constant and λ is the wavelength. The kinetic energy can be directly obtained from the accelerating voltage (V). When the accelerating voltage is higher than 100 kV, relativistic effects cannot be ignored because the electron velocities will be more than half that of the speed of light, which results in the calculated value of the wavelength being more of an approximation.⁶⁸

$$\lambda = \frac{h}{(2m_0E)^{0.5}} \quad (2.4)$$

The illumination system generates the electrons from the source and lets them pass through the specimen either in a broad beam or in a focused beam form depending on the arrays of condenser lenses in the illumination system. After the illumination system, the electrons are either in a parallel form or in a convergent form, as shown in Figure. 2.8 and Figure 2.9.⁶⁹

For simple imaging to observe the morphology or the size of the sample, the first two condenser lenses are adjusting to produce parallel beams of electrons. The sample should be thin enough for electron transmission and stable under the electron beam. The contrast of the image depends on the thickness and the atomic number of the material being imaged as discussed before. The objective lens is a key part of the illumination system, enabling a parallel electron

beam, as shown in Figure 2.8. If the objective lens is well focused, then the transmitted electrons will pass through a set of intermediate lenses and the projector lens will further magnify the

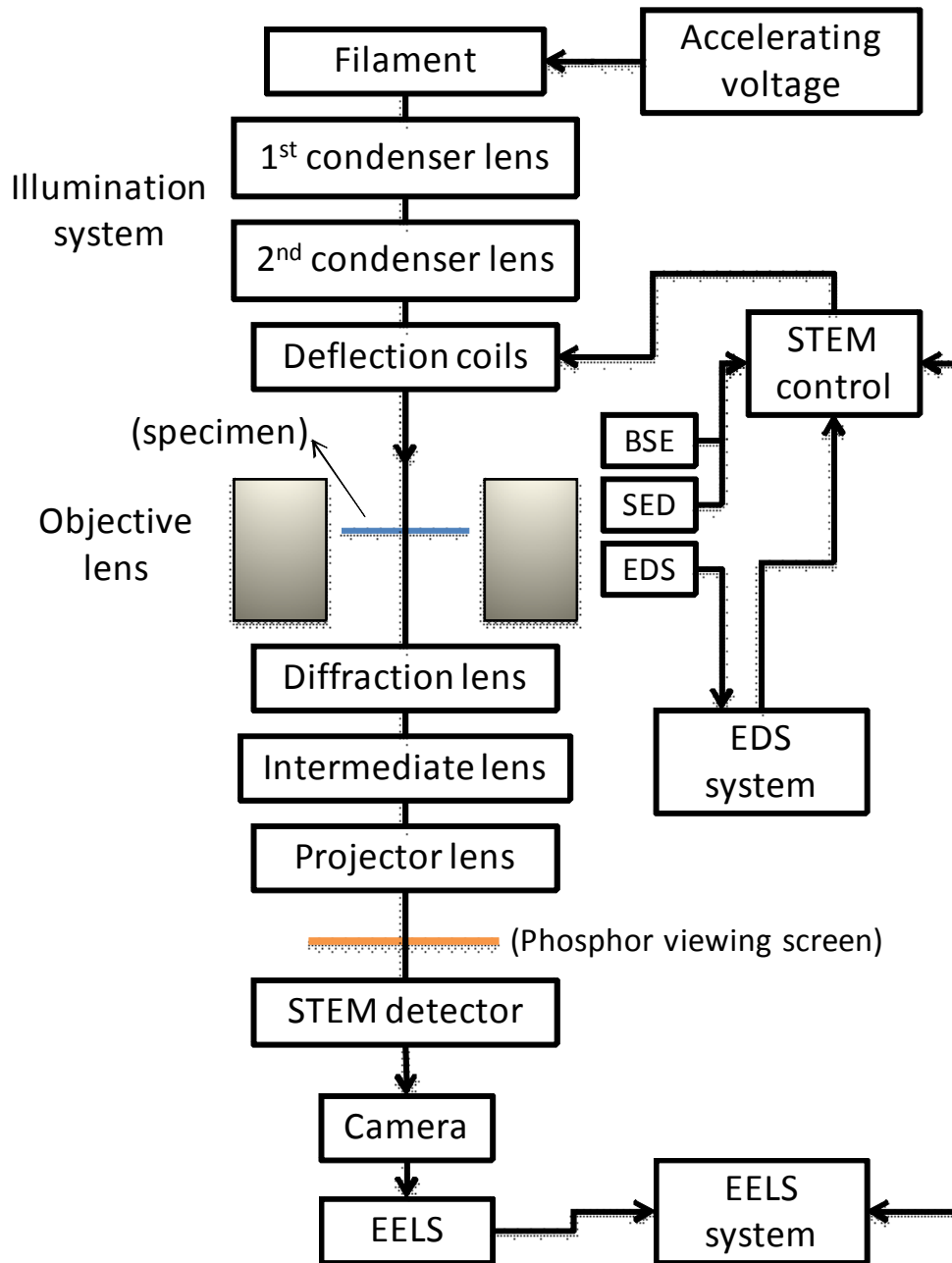


Figure 2.7 Schematic diagram for a TEM with STEM capability (adapted from Fultz, see ref.108)

transmitted pattern. The final image will be projected on a fluorescent screen, and then will be

captured by a camera system. The signal will be analyzed by the software system and stored in a digitalized form.

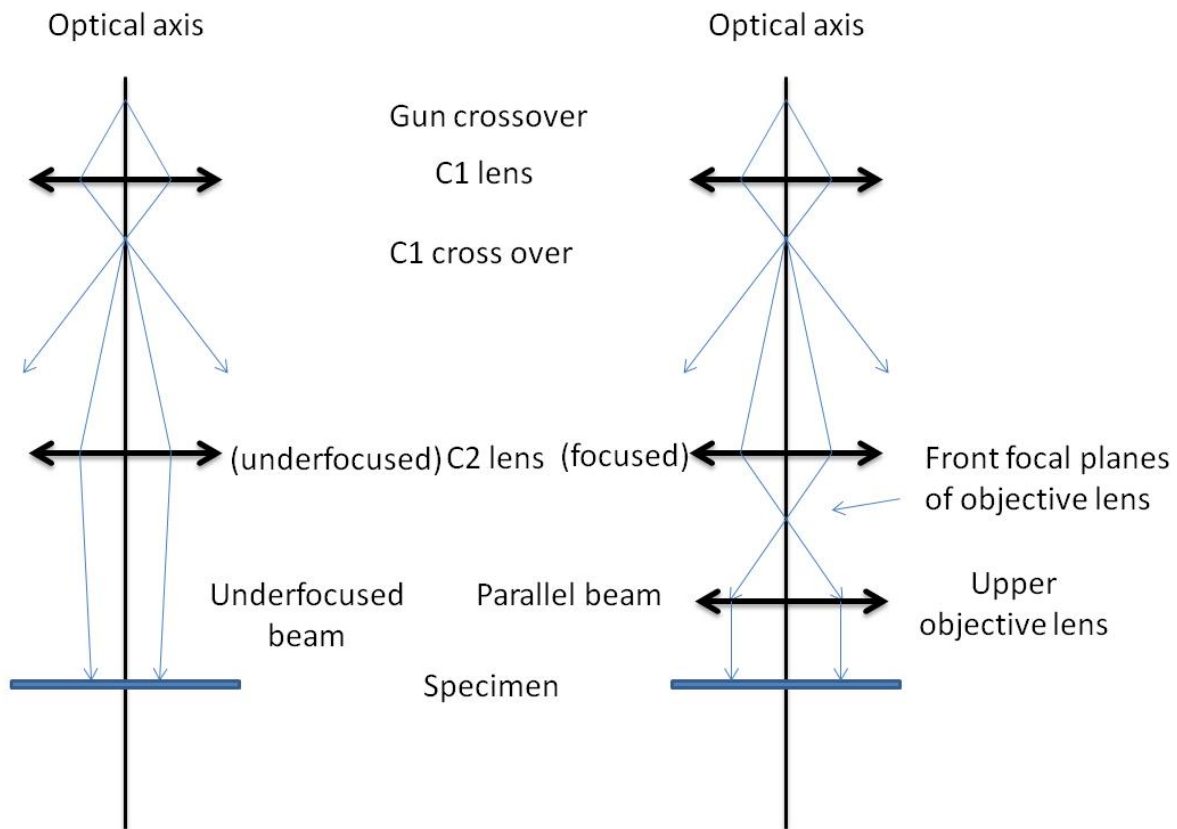


Figure 2.8 Ray diagram showing the parallel beam operation in the TEM: (left) using just C1 and an underfocused C2 lens, (right) creating parallel beams using C1, C2, and the objective lens(adapted from Williams, see Ref. 107)

For some advanced imaging such as XEDS, EELS, or CBED, more focused electron beams are required so that the intensity of the beam on a specific area of the specimen will be greatly increased. A convergent beam can be used as a probe, as shown in Figure 2.9. In this working mode, the C2 lens will be switched off and the upper-objective polepiece will be used as a C3 lens to provide the smallest possible probe and very large convergence angles. In this mode, the image is not immediately read because the convergence destroys the parallelism and the

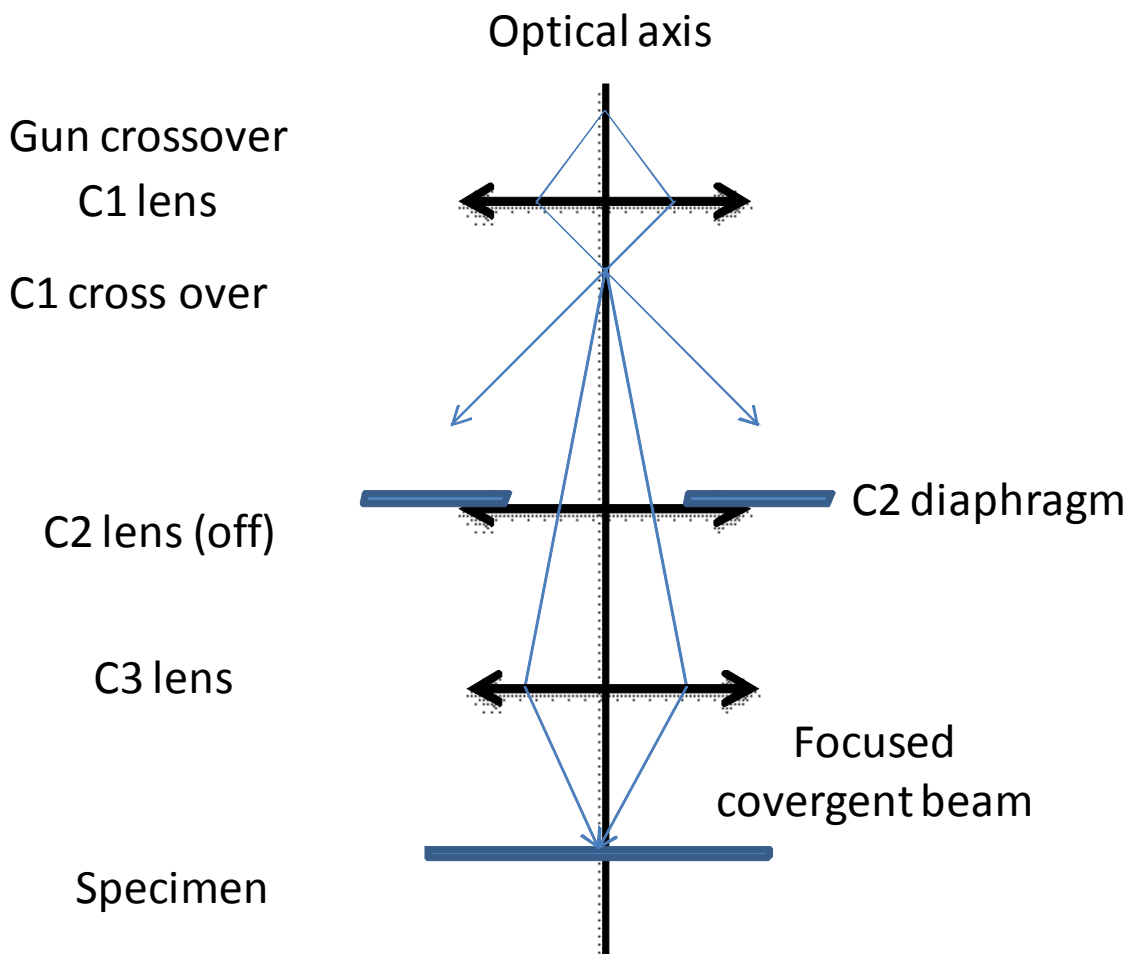


Figure 2.9 Ray diagram showing the convergent-beam/probe mode in the TEM (adapted from Williams, see Ref. 107)

image contrast is reduced. To see the image requires the beams to be scanned, which is standard in the illumination system of STEM and AEM (Auger electron microscopy) microscopes.

When the electron beams are projected onto the viewing screen or CCD, two basic imaging operations utilizing the objective aperture can be performed to improve the quality or enhance the contrast of the imaging. The images formed by the direct beam are called bright field (BF) images, while selecting for electrons that are not in the direct beam (blocking the direct beam) will form dark field (DF) images, as shown in Figure 2.10. Only crystalline portions of the specimen are shown in the dark field image as it forms from the diffracted beam. Dark field imaging studies in TEM are useful to study crystallinity and crystallite defects, and even for the imaging of individual atoms.

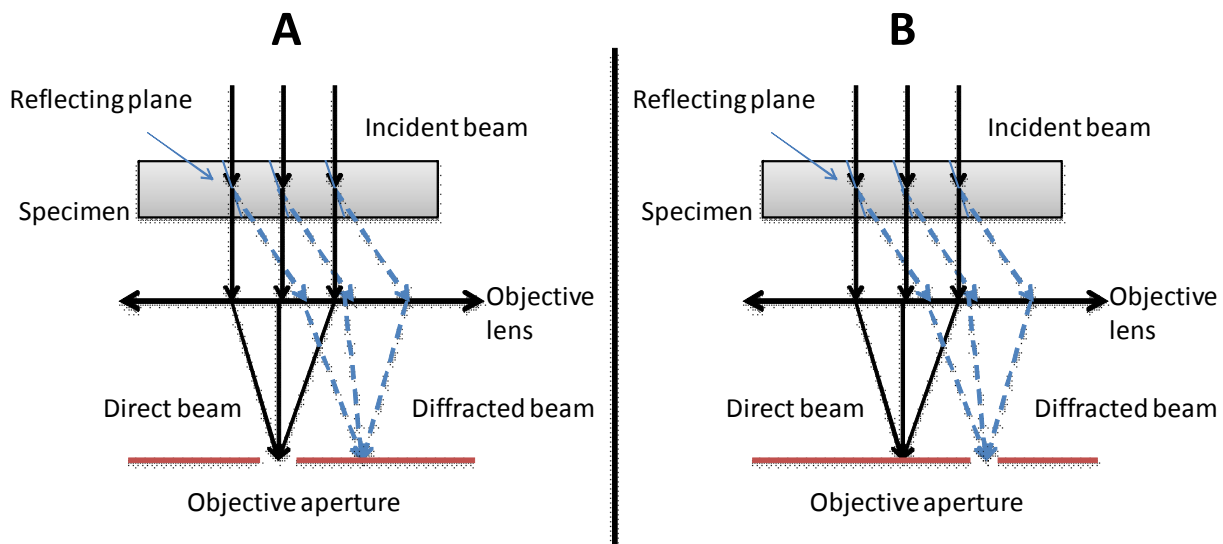


Figure 2.10 Ray diagrams showing how to produce (A) a bright-field (BF) image from the direct beam and (B) a dark-field (DF) image from the diffracted beam, by controlling the objective aperture (adapted from Williams, see Ref. 107).

Energy dispersive X-ray spectroscopy (EDS or EDX) is a common analytical technique used in TEM or STEM for the elemental analysis or chemical characterization of a sample. The technique relies on the evaluation of the X-ray emission from the sample. As shown in Figure 2.4 and Figure 2.6, characteristic X-rays can be generated when high energy electron beams hit specimen. The technique is based on the fact that each element has a unique atomic structure, which results in a unique set of peaks in the X-ray spectrum, as shown in **Figure 2.11**. The excited X-rays can be detected by the EDS accessory on the TEM. A common Si(Li) X-ray detector cooled to cryogenic temperatures with liquid nitrogen will convert X-ray energy into voltage signals and then send them to a pulse processor, which measures the signals. A new X-ray detector called silicon drift detector (SDD), is now equipped in modern systems. This consists of a high-resistivity silicon chip to drive electrons to a small collecting anode for high signal count rates and processing.

Several factors can affect the accuracy of the EDS technique including the overlapping of peaks for some elements and the composition and structure of the sample. The accuracy can be reduced in inhomogeneous and rough samples because of a relatively large spot size are needed to get good counting statistics in reasonable times. For practical analysis, EDS is not suitable for light elements with atomic numbers less than 4, due to the absorption of these X-rays generated by the Be window of the detector.

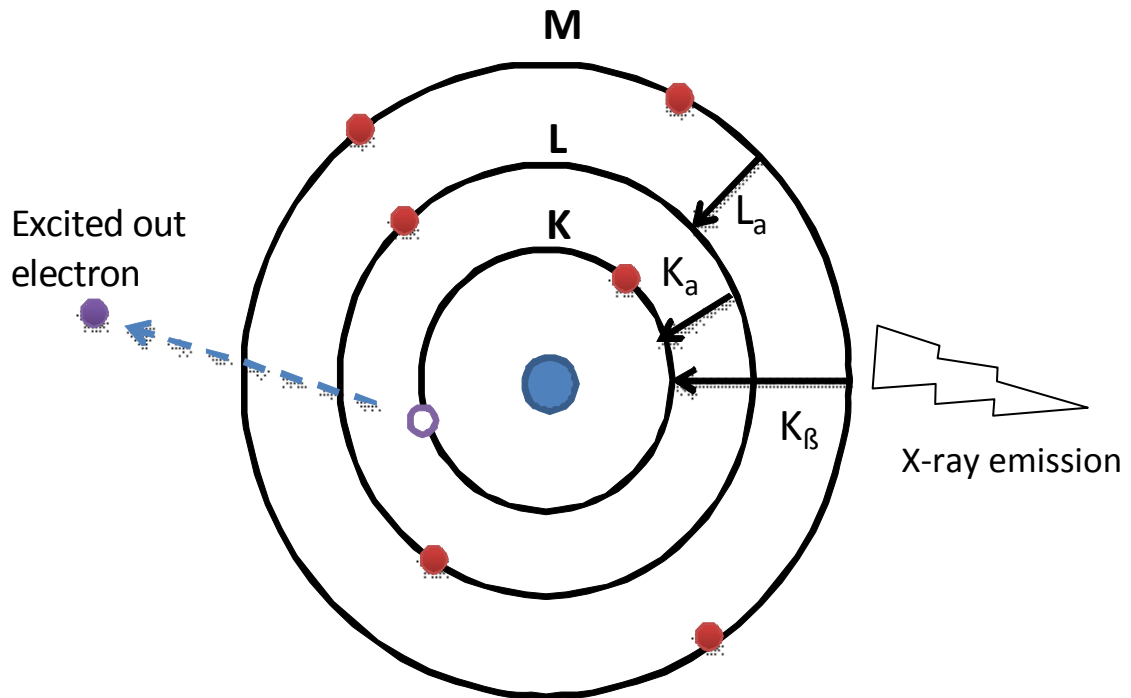


Figure 2.11 The working principles of EDS

In addition to imaging, the TEM can also be used to determine sample crystal structure and the crystal growth direction by examining diffracted electrons. In diffraction mode, the imaging-system lenses need to be adjusted to see the diffraction pattern so that the back-focal plane (BFP) can perform as the objective plane for the intermediate lens, as shown in Figure 2.12(A). For image mode, the intermediate lens needs to be readjusted so that the objective plane is the image plane of the objective lens, as shown in Figure 2.12(B). However, if the diffraction pattern in Figure 2.13(A) contains the electrons from the whole specimen illuminated with the beam, such a pattern is not useful, because the intensity of the direct beam is so strong that the view screen or CCD of the camera system will be damaged. For practical applications, a specific area of the specimen is selected and the intensity of the direct beam will be reduced to optimize

the final diffraction pattern. The SAED pattern consists of rings for a polycrystalline sample or a 2-D spot matrix for single crystal samples (single nanocrystal, orientated array of nanocrystals). The d-spacing of the specific lattice plane can be calculated from the diameter of the ring for

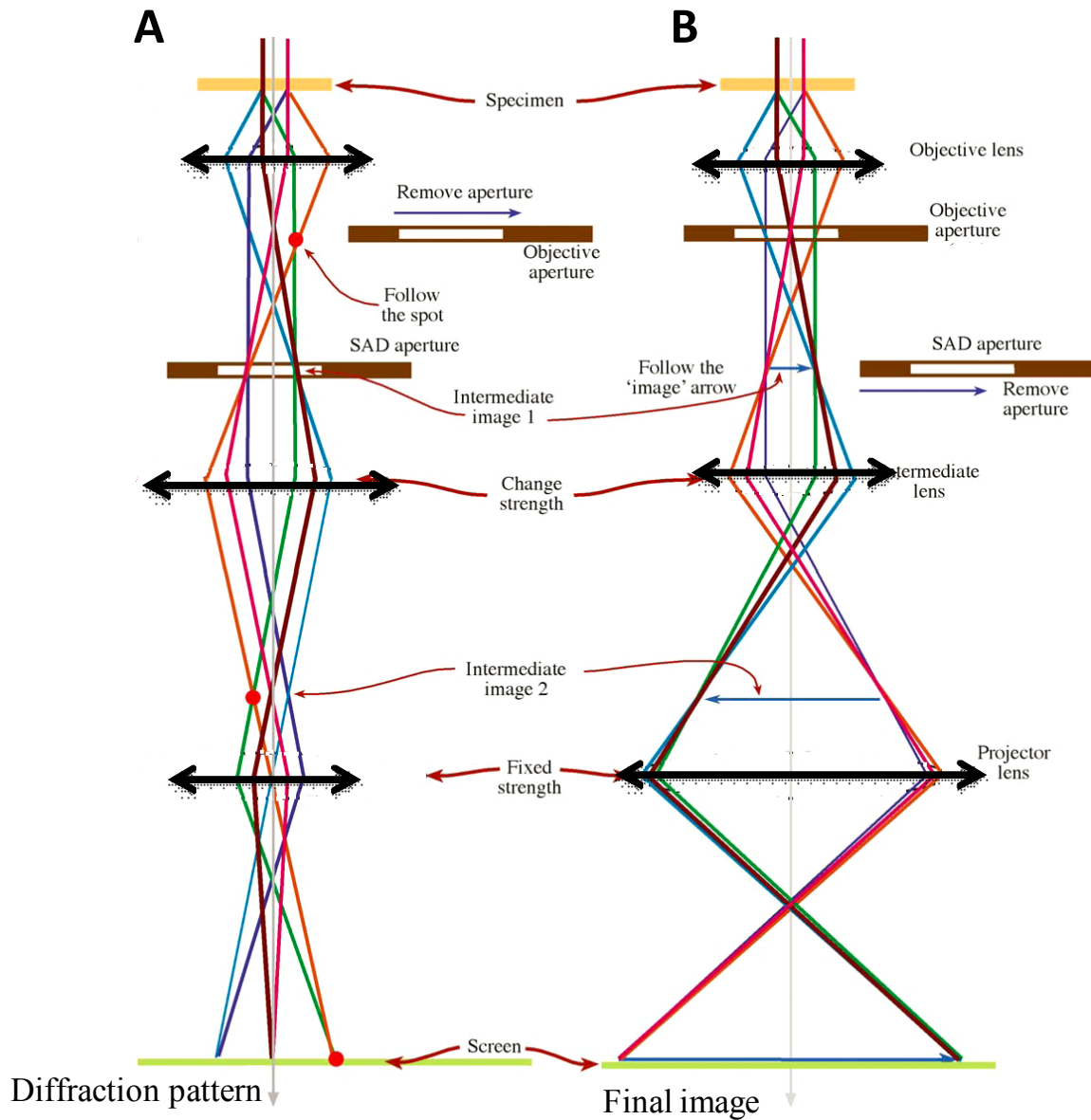


Figure 2.12 Ray diagram showing the two basic operations of the TEM imaging system: (A) diffraction mode and (B) image mode (adopted from Williams, Ref. 107)

polycrystalline samples, or the distance between the two spots across the center of an imaginary ring for single crystal samples.

In this dissertation research, TEM images were obtained with a JEOL 2010 HR TEM with the operation voltage set at 200 kV. Specimens were prepared by placing one drop of chloroform containing a dispersion of nanoparticles onto a Cu grid coated with a carbon film. EDS data were analyzed with an SDD detection unit, made by EDAX, Inc., is attached to the JEOL 2010 TEM. The analyzing software is EDAX Genesis v1.0.

2.3.5 High-Angle Annular Dark-Field (HAADF) Microscopy

In traditional dark-field imaging, only electrons scattering through the object aperture will be collected, while the main beam is blocked. In annular dark-field imaging with STEM, an annular dark-field detector is used to collect the scattered electrons that are not Bragg diffracted, from an annulus around the main beam. Thus, it is possible to sample far more scattering electrons than just those passing through the objective apertures, as shown in Figure 2.13.^{68, 70} The signal collection efficiency will be improved and the main beam can be allowed to travel to an EELS detector, which means both types of measurements can be simultaneously performed. The average atomic number of the specimen encountered by the incident probe strongly affects the contrast of HAADF images. Other factors, including the extent of defocusing or sample thickness, will also influence the image contrast. The spatial resolution of the HAADF is confined by the size of the focused incident probe. For most high resolution imaging applications, the specimen must be less than 40 nm thick.

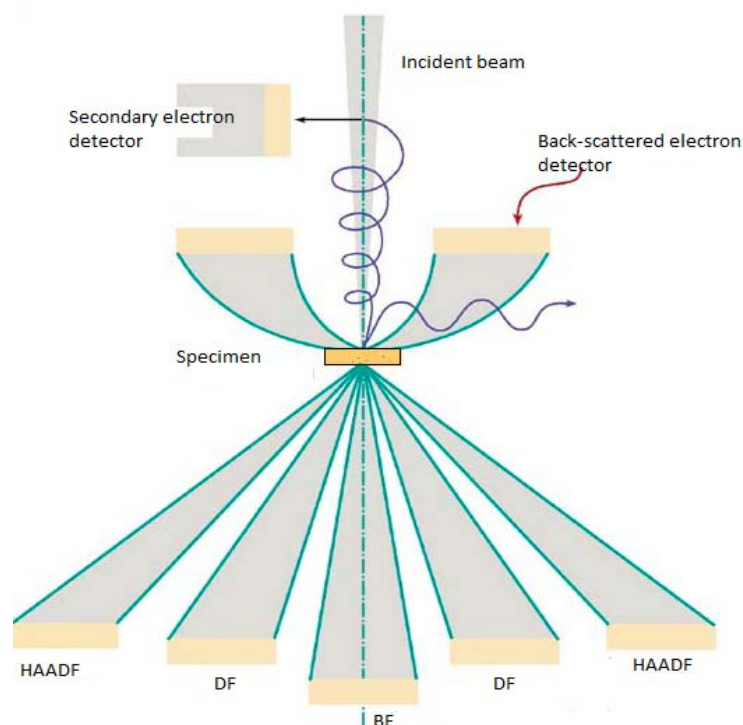


Figure 2.13 A schematic diagram showing the various types of electron detectors in a STEM (adapted from Williams, Ref. 107).

The properties of the HAADF make it widely used in (1) quantitative elemental mapping (as we use in this dissertation research), (2) supported catalyst characterization, (3) compositional imaging/modulation of semiconductor interfaces or superconductors, and (4) observation of lattice dislocations, precipitates and grain boundary segregations of the crystals, etc. In this dissertation research, to understand the composition and the interface of the core-shell structure in MnAs, we performed HAADF on MnAs nanoparticles using a FEI Titan 80-200 TEM/STEM with ChemiSTEM Capability at Oregon State University with the help of Dr. Yi Liu. This instrument uses a field emission electron source and has a resolution capability of 0.24 nm for TEM images and 0.16 nm for STEM. With the EDS units (four embedded Bruker silicon

drift detector (SDD) detectors), the chemical composition, elemental distribution mapping and line profile element analysis can be analyzed simultaneously using ChemiSTEM technology.

2.3.8 Magnetic Measurements

There are two basic methods for acquiring magnetic measurements: DC magnetic measurements, which determine the equilibrium value of the magnetization for the sample and AC magnetic measurements, in which a small AC driven magnetic field is applied to a sample, causing a time-dependent AC magnetic moment to form in the sample. AC measurements can provide more information about the magnetization dynamics, which are not obtained from DC magnetic measurements because the moment of the sample is constant during the measuring time.

Superconducting Quantum Interference Device (SQUID) DC Magnetometry

Among various magnetometers that are used to measure the magnetic properties of materials, those using a SQUID are the most sensitive and effective for measuring subtle magnetic properties. The sensitivity of SQUIDs to measure magnetic fields can be as low as 5 aT (1 aT = 10^{-18} T). Figure 2.15 shows the general schematic diagram of a SQUID magnetometer. The DC SQUID was invented after the discovery of the Josephson Effect and is made of a Josephson junction, where two superconductors are separated by a thin insulator. The DC SQUID consists of two Josephson junctions in parallel inserted in a superconducting loop. As shown in Figure 2.15A, when the magnetic flux in the superconducting loop changes, the output voltage will also change and the signal is proportional to the change of magnetic flux.

In SQUID systems, common superconductor magnets are made of Niobium and are operated in a cryogenic environment cooled by liquid He (4.2 K). The magnetic field in the instrument can be varied as the sample temperature. As shown in Figure 2.14(A), the magnetic flux in the instrument is directly related to the applied magnetic field and the variation in effective cross-sectional area. When the sample is loaded inside the superconducting coil, the magnetic flux will change as the sample is raised and lowered. The SQUID in the instrument is not directly linked with the magnetic field but coupled to it with superconducting wire detection coils (Figure 2.14B)⁷¹ which are sensitive to the change of the magnetic flux of the specimen. A voltage will be generated alongside the change in magnetic flux, which will cause a quantum phase change across the Josephson junctions. The final current change is recorded and reflects the magnetic moments of the specimen.

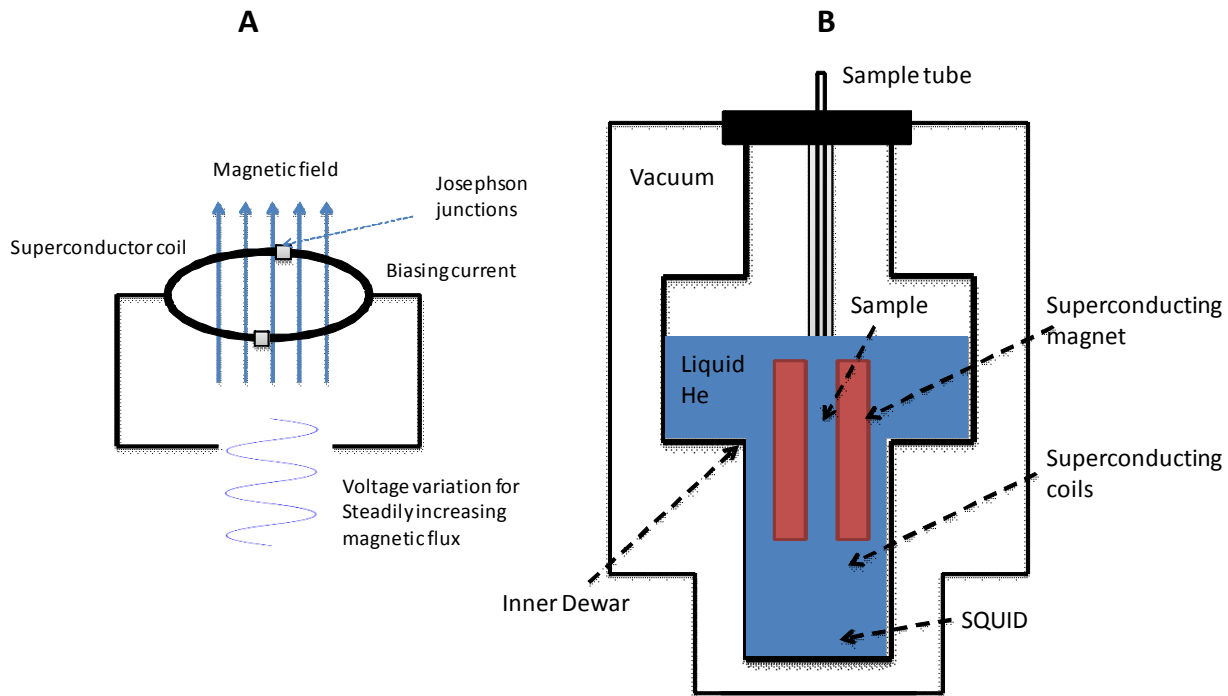


Figure 2.14 General schematic diagram for (A) a SQUID detection coil and (B) a SQUID magnetometer (adapted from Clark, see ref.110)

AC Magnetic Measurements

As shown in Figure 2.15, the AC magnetic susceptometer contains an AC-drive coil set that provides an alternating AC excitation field and a detection coil set that responds inductively to the combined sample moments and the excitation field. When the frequency of AC drive field is very low, the AC measurement is similar to DC magnetometry. In this case, the sample magnetic moment follows the same kind of $M(H)$ curve that can be measured in a DC experiment, as shown in Equation 2.5. As the AC measurements are sensitive to the slope of $M(H)$ curve (The magnetic susceptibility, χ) and not to the absolute value, small magnetic shifts can be detected even when the absolute moment is large.

$$M_{AC} = (dM / dH) \cdot H_{AC} \sin(\omega t) \quad (2.5)$$

H_{AC} is the amplitude of the driving field, ω is the driving frequency and $\chi = dM/dH$ is the slope of the $M(H)$ curve, called the susceptibility, which is the quantity of interest in AC magnetometry.

At higher frequencies, the AC magnetic moment of the sample will not strictly follow the DC magnetization curve because of dynamic effects shown in the sample. For this reason, the AC magnetic susceptibility is also known as the dynamic susceptibility. Basically, the AC magnetic susceptibility measurement at high frequencies yields two quantities: χ (the magnitude of the susceptibility) and ϕ (the phase shift, relative to the drive signal). Thus, the AC susceptibility has two components: χ' (in-phase, real) and χ'' (out-of-phase, imaginary). The relationships are described in Equation 2.6. In ferromagnets, a nonzero χ'' can reflect the irreversible domain wall movement (as shown in Figure 1.9). Both of χ' and χ'' are very sensitive to the transformations of thermodynamic phase, and can be used to determine the transition temperatures of magnetic materials.

$$\chi' = \chi \sin\phi \quad (2.6)$$

$$\chi'' = \chi \cos\phi$$

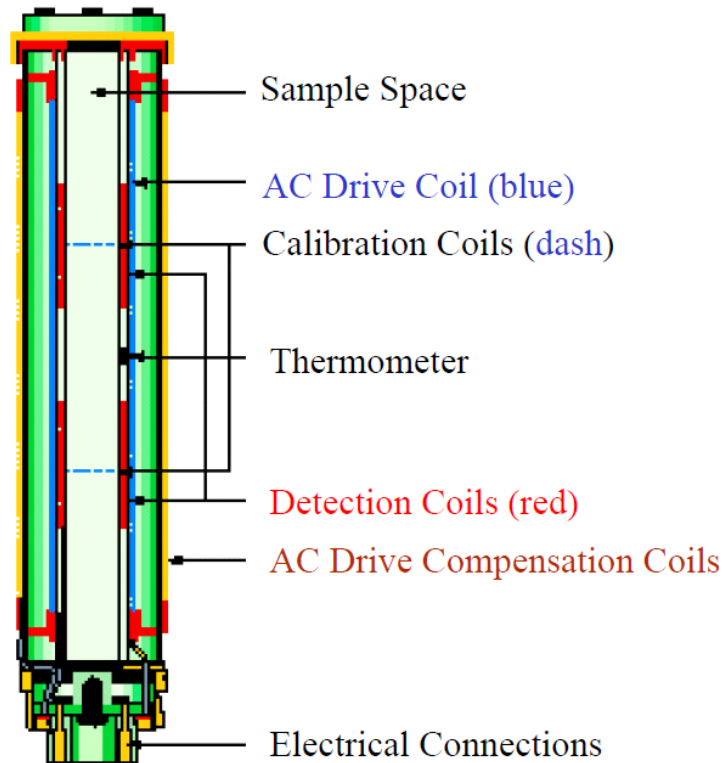


Figure 2.15 A general schematic diagram of a coil set for AC magnetic susceptibility measurements (adapted from Handbook of PPMS, Quantum Design, Inc.)

In this dissertation research, MnAs nanoparticles are loaded in a glass capillary tube 3 mm in diameter, evacuated in vacuum and then sealed under argon to protect MnAs nanoparticles from oxidation. A plastic straw is used to support the sample tube. DC magnetic properties were measured using a Quantum Design MPMS-5S SQUID magnetometer under various temperatures and fields. AC magnetic susceptibilities measurements were taken using a Quantum Design Model 6000 Physical Property Measurements System (PPMS).

CHAPTER 3

The Magnetostructural Phase Transformation Behavior in Bulk and Nanoscale MnAs

3.1 Introduction

As discussed in Chapter 1, arrested precipitation syntheses of MnAs nanoparticles result in two distinct materials: type-A MnAs (prepared by slow heating) adopting the hexagonal (α) structure at room temperature, and type-B (prepared by rapid nucleation at high temperature) adopting the orthorhombic (β) structure at room temperature. Prior studies suggested that type-A MnAs nanoparticles do not undergo the characteristic phase change ($\alpha \rightarrow \beta$) upon heating to 310 K.

In this chapter, detailed structural evaluations of bulk MnAs, type-A MnAs nanoparticles and type-B MnAs nanoparticles were performed using the atomic pair distribution function (PDF) technique and Rietveld refinement as a function of temperature in the range where the magnetostructural phase transformation is expected. These data are then correlated to magnetic data. I synthesized the samples, performed routine characterization, and participated in acquisition of synchrotron data. Ambesh Dixit and Gavin Lawes from the Department of Physics and astronomy (Wayne State University), acquired the magnetic data, while Peng Tian and Simon Billinge from the Department of Physics (Michigan State University) and the Department of Physics and Applied Mathematics, Materials Science & Engineering (Columbia University) performed PDF and Rietveld analysis of synchrotron data. This work has been published as: Tian

P, Zhang Y, Senevirathne K, Brock SL, Dixit A, Lawes G, Billinge SJL. 2011. Diverse Structural and Magnetic Properties of Differently Prepared MnAs Nanoparticles. *ACS Nano* 5: 2970-2978.

3.2 Sample Preparation

3.2.1 Bulk MnAs:

The bulk MnAs we used for this study was purchased from Pfaltz & Bauer Chemicals. A chemical etching process was performed to eliminate impurities. Briefly, 1g ground bulk MnAs was put in 20 ml concentrated HCl solution, slowly heated to 80°C, and kept at that temperature for 20 minutes. After that, the sample was washed with 50 ml de-ionized water several times to remove the soluble impurities, then the purified MnAs sample was washed and reprecipitated in chloroform and ethanol.

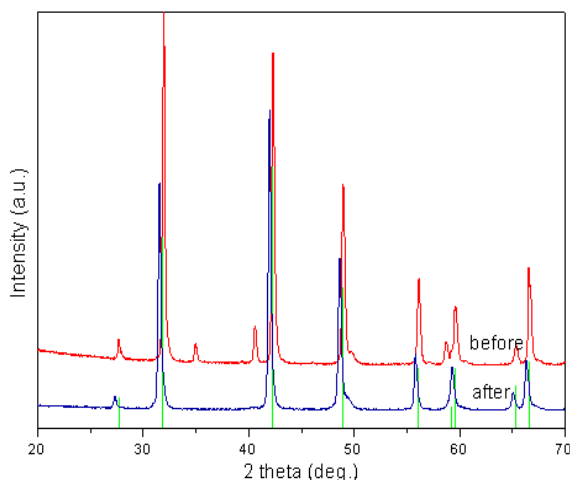


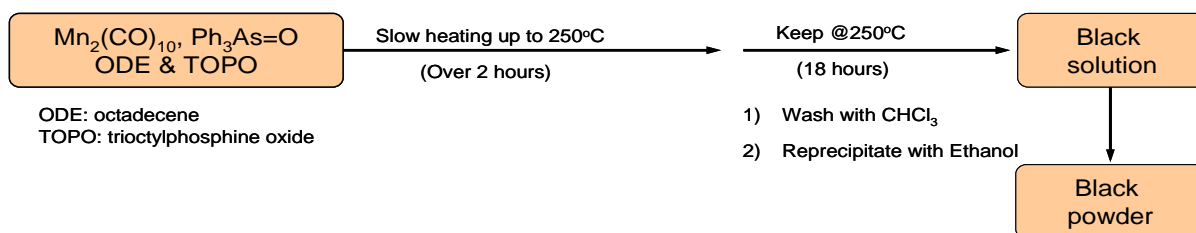
Figure 3.1 The XRD pattern of bulk MnAs before and after etching

The PXRD pattern of a chemically etched commercial bulk MnAs sample is shown in Figure 3.1. Etched MnAs adopts the α phase structure at room temperature, as expected. Before the etching, there are some extra peaks that can be attributed to impurities, most notably β -MnAs. Those are eliminated after treatment with concentrated HCl as shown in Figure 3.2.

3.2.2 Synthesis of MnAs Nanoparticles

The synthesis of MnAs nanoparticles can be achieved either by a slow heating method to produce type-A MnAs nanoparticles, or by a high temperature fast injection method to produce type-B MnAs nanoparticles. Scheme 3.1 shows the slow heating method. 0.256 mmol of $\text{Mn}_2(\text{CO})_{10}$ is mixed with 0.528 mmol $\text{Ph}_3\text{As}=\text{O}$, 8.0 ~ 10.0 ml of 1-octadecene (ODE) and 5g of trioctylphosphine oxide (TOPO) and placed in a Schlenk flask in an argon filled glove box then moved to a Schlenk line. After purging for 20 minutes, this mixture is gradually heated up to 250 °C over 2 hours. The color of the mixture changes from yellow to orange and finally black. The reaction is maintained at 250 °C for 18 h. The as-prepared nanoparticles are then isolated by centrifuging after dispersing in chloroform and precipitating in absolute ethanol. This is repeated

Scheme 3.1 The procedure for type-A MnAs nanoparticle synthesis by the slow heating method



several times until the TOPO is removed.

The fast injection method is shown in Scheme 3.2. The same amount of $\text{Mn}_2(\text{CO})_{10}$, $\text{Ph}_3\text{As}=\text{O}$ and 1-octadecene are mixed together in the glove box then moved to the Schlenk line and purged for 15 minutes. Before injection, the mixture is slightly heated with a heat-gun until the powder precursors are evenly mixed. Then the mixture is cannulated under inert conditions into hot TOPO (5.0 g) maintained at 330 °C. The reaction is kept at 330 °C for 18 hours. The isolation of MnAs prepared by the fast injection method is the same as that described for MnAs by the slow heating method.

Scheme 3.2 The procedure of type-B MnAs nanoparticle synthesis by the fast injection method

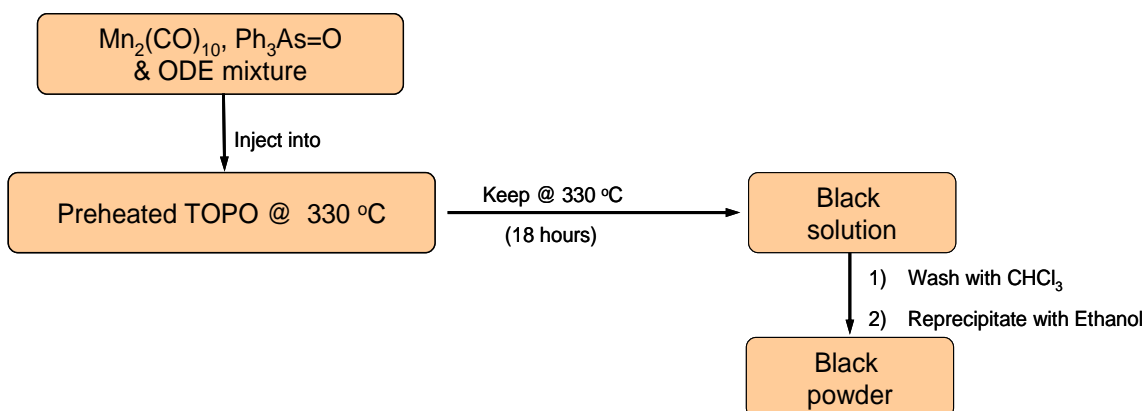


Figure 3.2 shows the powder X-ray diffraction pattern (PXRD) of synthesized type-A MnAs

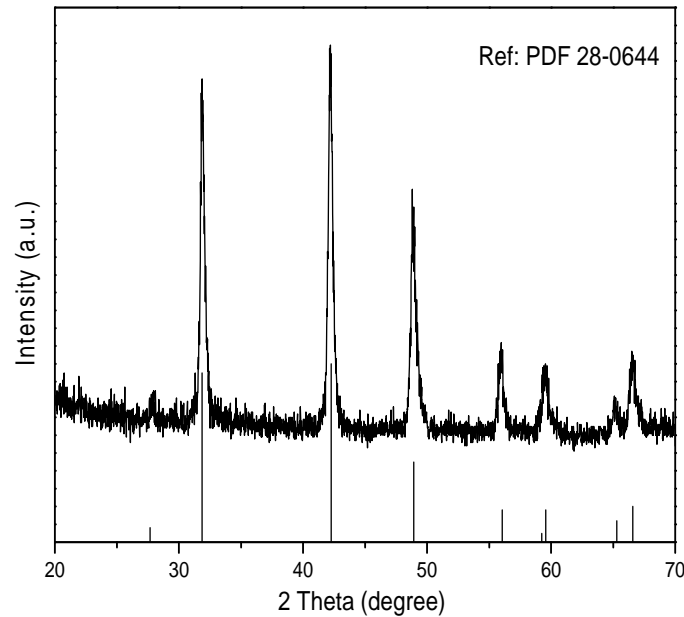


Figure 3.2 The PXRD pattern of MnAs nanoparticles synthesized by the slow heating method (type-A MnAs nanoparticles). The reference PDF corresponds to α -MnAs.

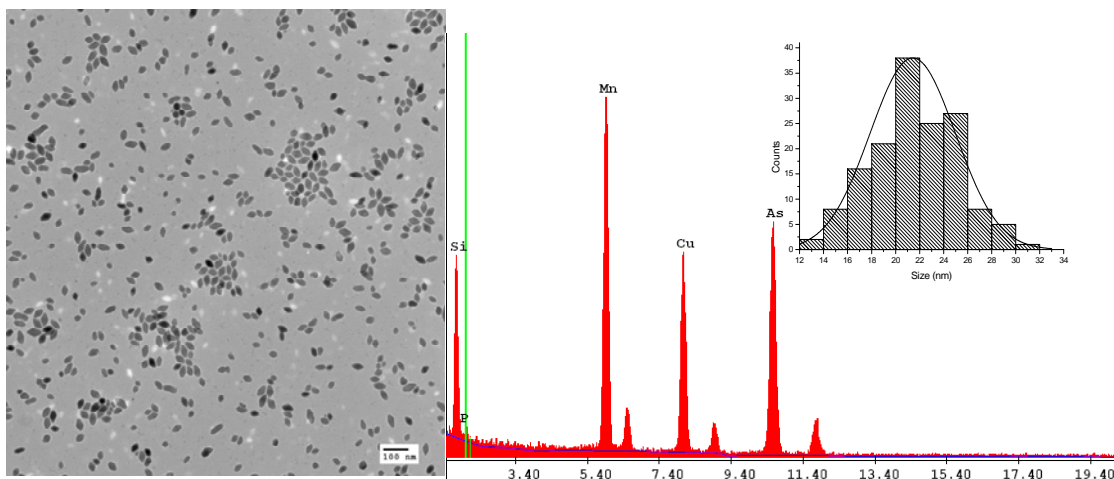


Figure 3.3 TEM image including the size distribution and the EDAX pattern of MnAs nanoparticles prepared by the slow heating method (type-A nanoparticles)

nanoparticles by slow heating at 250°C. The pattern can be indexed to the α -MnAs (hexagonal NiAs type). The crystallite size, calculated from the Debye-Scherrer equation using the full width at half maximum (FWHM) of the peak at $2\theta = 32.16^\circ$, which belongs to the (111) reflection, was estimated to be 22 nm. The TEM image and the size distribution histogram of this type-A MnAs nanoparticle sample are shown in Figure 3.3. The TEM image reveals the particles to be a core-shell type structure with a high contrast core and a low contrast shell. The synthesized type-A MnAs nanoparticles are not spherical, but adopt an elliptical shape. The average particle size for the elliptical α -MnAs was calculated by measuring the diameter of the cores along the small axis, which is approximately 21.7 nm and is in good agreement with the size computed from PXRD data.

Type-B MnAs nanoparticles synthesized by the rapid injection method at 330°C are also crystalline and can be indexed to the β -MnAs (orthorhombic MnP-type) structure, as shown in Figure 3.4. There is only a slight difference in the peak positions for the two types of phases.

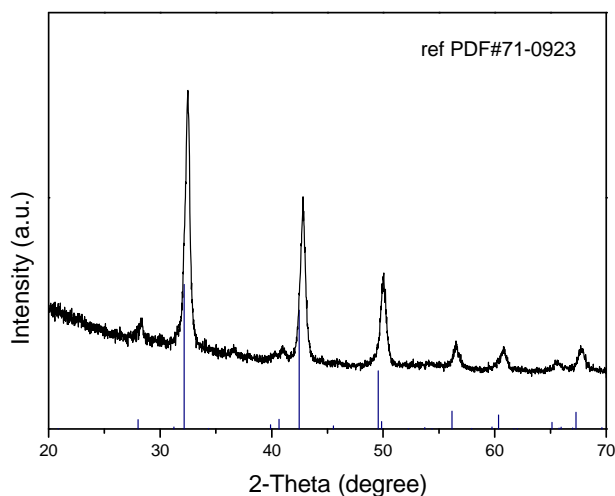


Figure 3.4 The PXRD pattern of type-B MnAs nanoparticles prepared by the rapid injection method. The reference PDF corresponds to β -MnAs.

Compared to α -MnAs, there are two characteristic peaks appearing at 39.8 and 40.7° in β -MnAs structure, which helps to distinguish the phase of MnAs. According to the Scherrer Equation, the computed size of synthesized type-B MnAs is about 18 nm. Similar to type-A MnAs nanoparticles, these type-B MnAs nanoparticles also show a core-shell type structure, but look to be more spherical, as shown in the TEM image of β -MnAs in Figure 3.5. However, due to aggregation, the detailed size distribution cannot be provided.

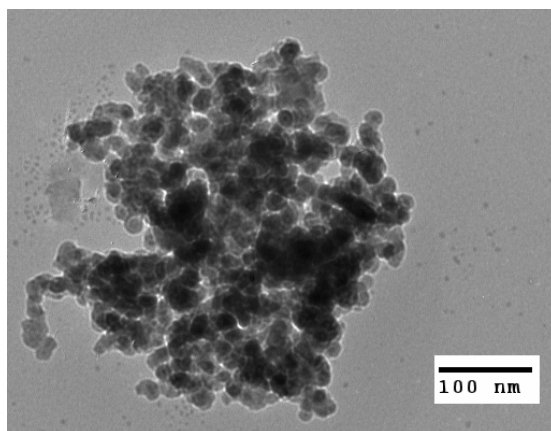


Figure 3.5 TEM image of MnAs nanoparticles prepared by the rapid injection method.

Atomic Pair Distribution Functional Analysis

Total scattering powder x-ray diffraction characterization for selected bulk MnAs, 22 nm type-A MnAs nanoparticles and 18 nm type-B MnAs nanoparticles were performed at the 11-ID-B beam-line at the Advanced Photon Source (APS) at Argonne National Lab. For bulk MnAs, the Rietveld analysis using an α -MnAs model is shown in Figure 3.6 (left subfigure). It is obvious that the α model fit at 295 K is much better than the fit at 335 K for the bulk sample, indicating that bulk MnAs prefers the α structure at 295 K but not at 335 K. This is expected

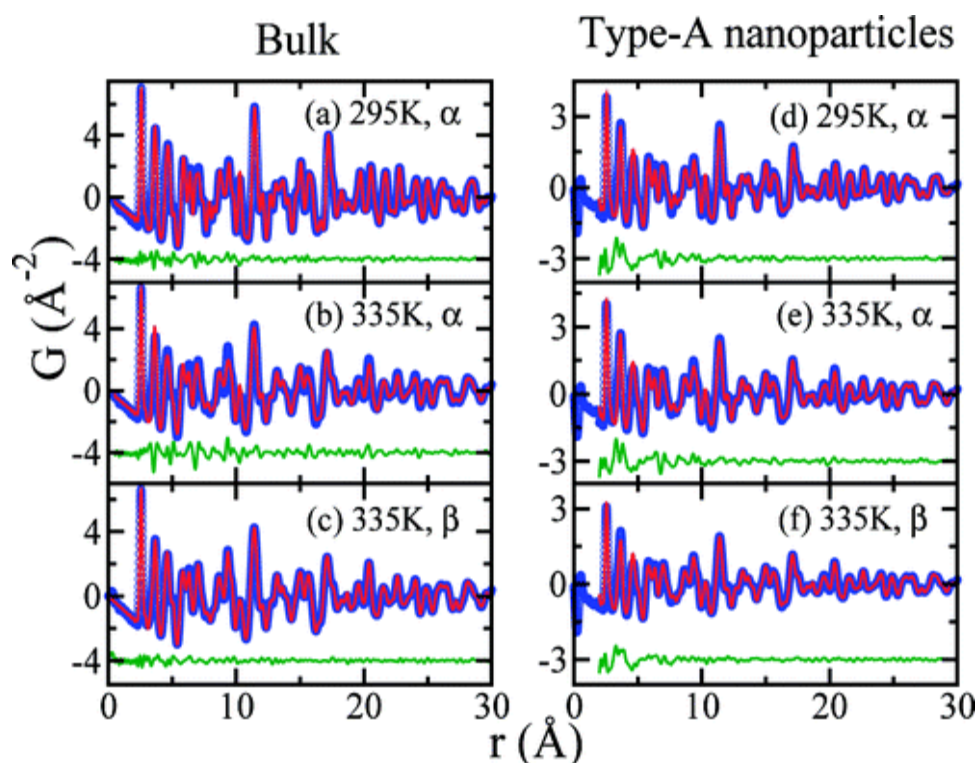


Figure 3.6 PDF refinements on the bulk MnAs (left) and type-A MnAs nanoparticles (right). The blue curve represents the experimental PDF data and the red line is the calculated PDF data from Rietveld refinement. The green curve is the difference curve between the experimental data and calculated model data

based on the reported data on bulk MnAs.⁵⁴ With the same analysis performed, type-A

nanoparticles showed similar fitting as the bulk material. At 295 K, which is below the Curie temperature, the calculated α -model data fits the experimental data well, whereas at 335 K, the calculated β -model data provides the better fit to the experimental data for type-A MnAs nanoparticles. For a more detailed comparison, the difference curve for the experimental diffraction data at 295 K and 335 K is shown in Figure 3.7(a) for bulk MnAs and in Figure 3.7(b) for type-A MnAs nanoparticles. Figure 3.7(c) shows an overlay of the difference curves from Figure 3.7(a) and Figure 3.7(b), scaled by the factor of 4. The different curves match very well suggesting a similar structural change is occurring in both materials, although the change in the

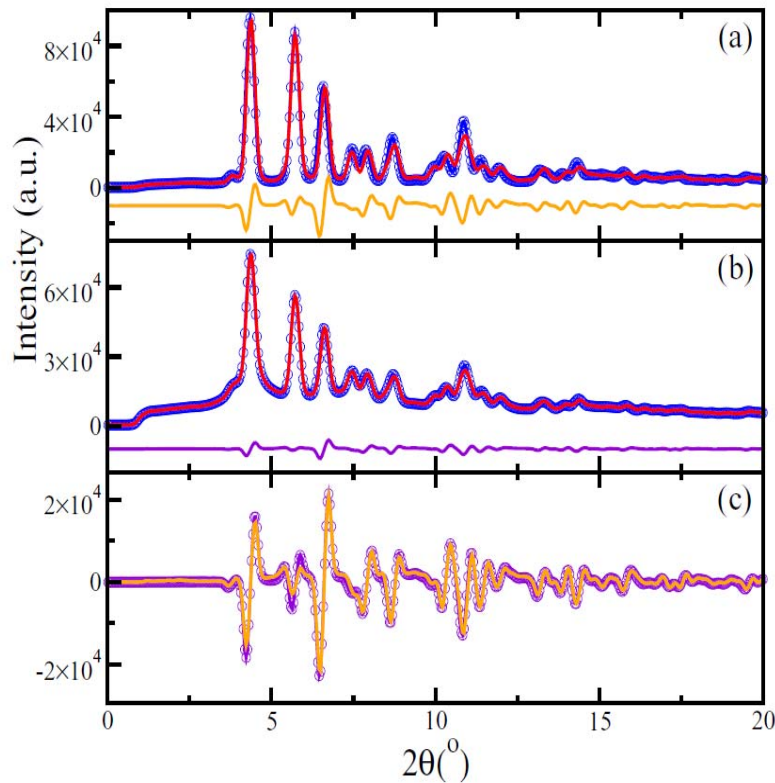


Figure 3.7 (a) The difference curves (orange) of diffraction data for bulk MnAs between 295 K (blue) and 335 K (red); (b) The difference curves (violet) of diffraction data for type-A MnAs nanoparticles between 295 K (blue) and 335 K (red); (c) Comparison of the (a) and (b) curves (the (b) curve is scaled by a factor of 4 for direct comparison)

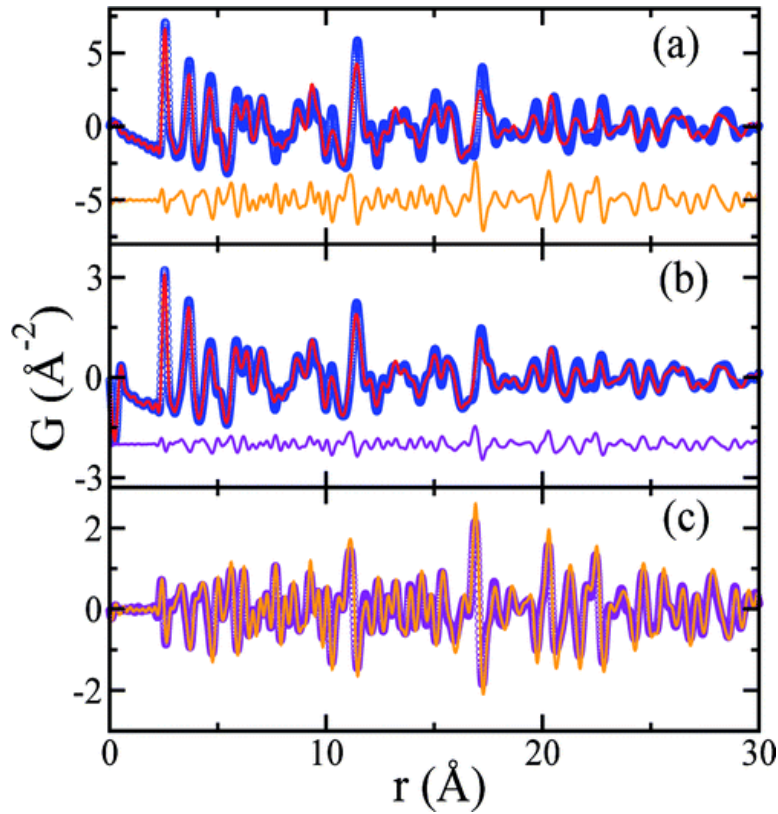


Figure 3.8 (a) The difference curves (orange) of PDF data for bulk MnAs between the PDF at 295 K (blue) and 335 K (red); (b) The difference curves (violet) of PDF data for type-A MnAs nanoparticles between the PDF at 295 K (blue) and 335 K (red); (c) Comparison of the curve (a) and (b) (scaled by a factor of 4).

nanoparticles is noticeably smaller (smaller difference curve). In order to verify whether the structural phase transition in bulk MnAs and type -A MnAs nanoparticles is the same, the change in the PDF for bulk MnAs and type-A MnAs for data acquired at 335 K and 295 K was also compared, as shown in Figure 3.8. The difference curves overlap perfectly when the type-A MnAs nanoparticles data is scaled up by a factor of 4. Thus, the established temperature induced $\alpha \rightarrow \beta$ transition in bulk MnAs appears to also be happening in type-A MnAs nanoparticles.

More evidence for $\alpha \rightarrow \beta$ phase changes in bulk and type-A MnAs nanoparticles can be obtained from Rietveld sequential refinements to the α model performed on the data collected on bulk MnAs in the range from 295 K to 335 K (Figure 3.9). Based on the characteristic hysteresis in lattice parameter changes and isotropic thermal parameters (U_{iso}) shown, there is a structural phase transformation occurring. The a lattice parameter undergoes an abrupt decrease whereas the c lattice parameter abruptly increases. The thermal parameters for both Mn and As increase

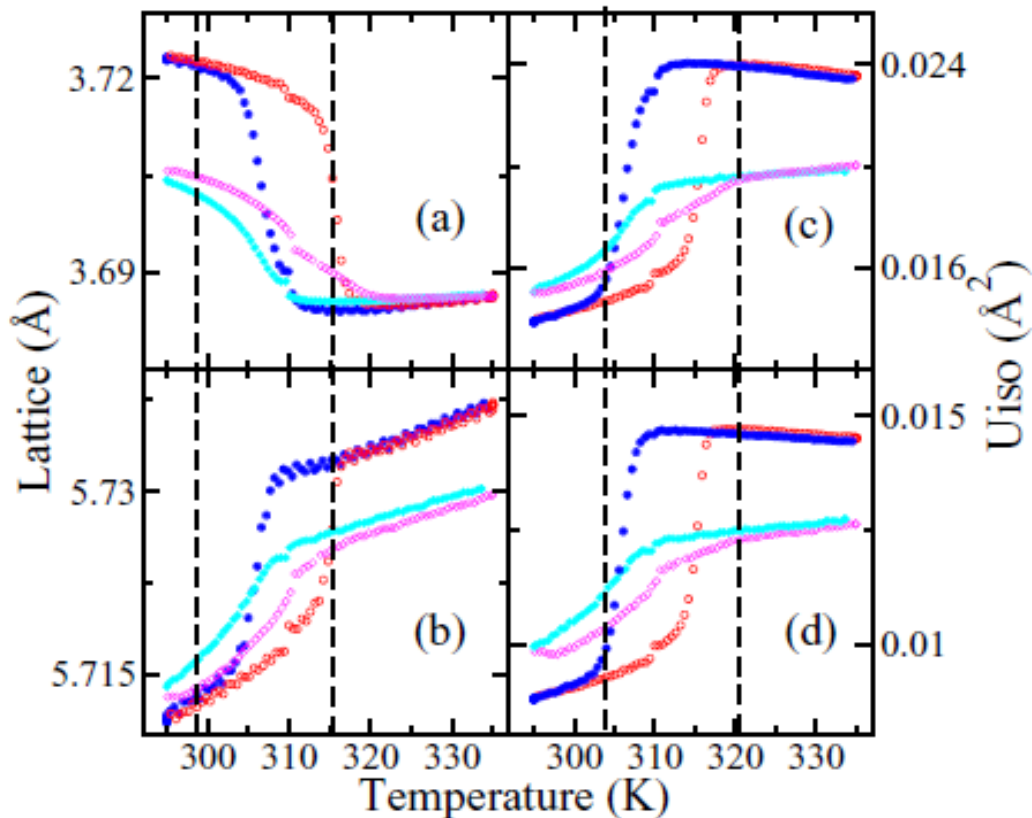


Figure 3.9 Comparison of lattice parameters and atomic displacement factors from Rietveld refinements of the bulk MnAs and type-A MnAs nanoparticles to the α -phase structure model upon heating from 295 K to 335 K (red for bulk and cyan for type-A nanoparticles on heating) and cooling back from 335 K to 295 K (blue for bulk and magenta for type-A nanoparticles): (a) lattice parameter a , (b) lattice parameter c , (c) U_{iso} for Mn, (d) U_{iso} for As.

abruptly and substantially, consistent with the expectation that the α model does not provide a good fit at higher temperatures. The temperature range of the hysteresis, starting at 303 K and ending at 317 K, matches the reported data for bulk MnAs.⁷² As a comparison, the α -MnAs model Rietveld refinement was also applied to type-A nanoparticles. For type-A MnAs nanoparticles, a similar hysteresis was observed, indicating that a phase transition occurs for type-A MnAs nanoparticles similar to that in the bulk MnAs. However, the magnitude of the change is smaller for type-A MnAs nanoparticles and the hysteresis is a little bit broader.

As a comparison, the PDF analysis of type-B MnAs nanoparticles is shown in Figure 3.10. It can be quantitatively observed from the difference plots that at both 295 K and 335 K,

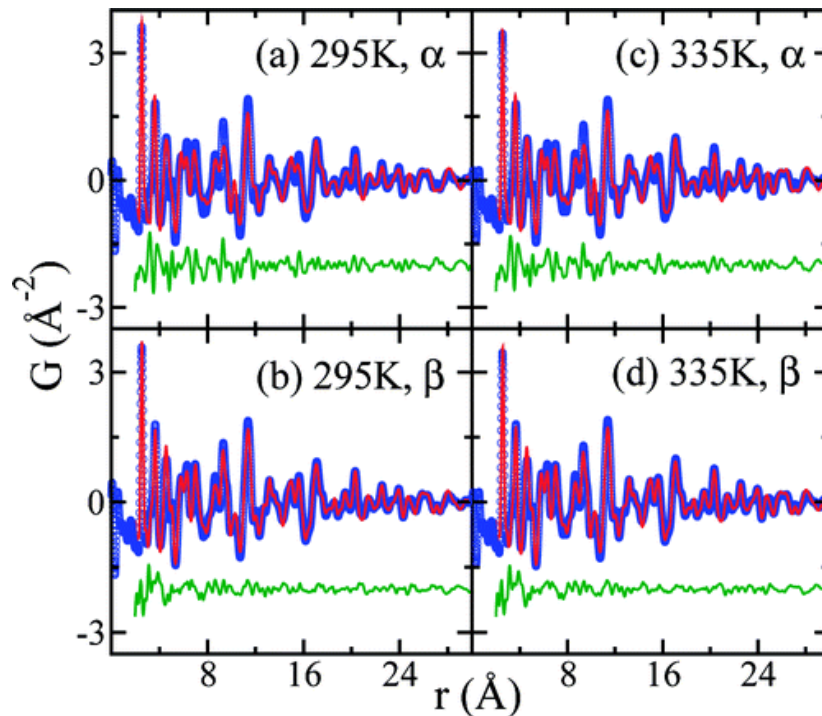


Figure 3.10 PDF refinements for type-B MnAs nanoparticles at (a) 295 K with α model fitting, (b) 295 K with β -model fitting, (c) 335 K with α model fitting and (d) 335 K with β model fitting. The colors correspond to the same curve representations as shown in Figure 3.6

the β -model data fits better than the α -model data at both temperatures, indicating that type-B MnAs may not be exhibiting a phase transformation process in this temperature range, in contrast to what is observed in bulk MnAs and type-A MnAs.

A comparison of the difference curves from diffraction of bulk MnAs and β -MnAs nanoparticles is shown in Figure 3.11, while the comparison of the corresponding PDFs is shown in Figure 3.12. It is observed that the difference curves for either diffraction data or PDF data of bulk MnAs cannot be matched to that of type-B MnAs nanoparticles. These comparison results suggest that type-B MnAs nanoparticles do not undergo the same structural phase transition as bulk MnAs does in this temperature range. Moreover, the very low intensity of the difference

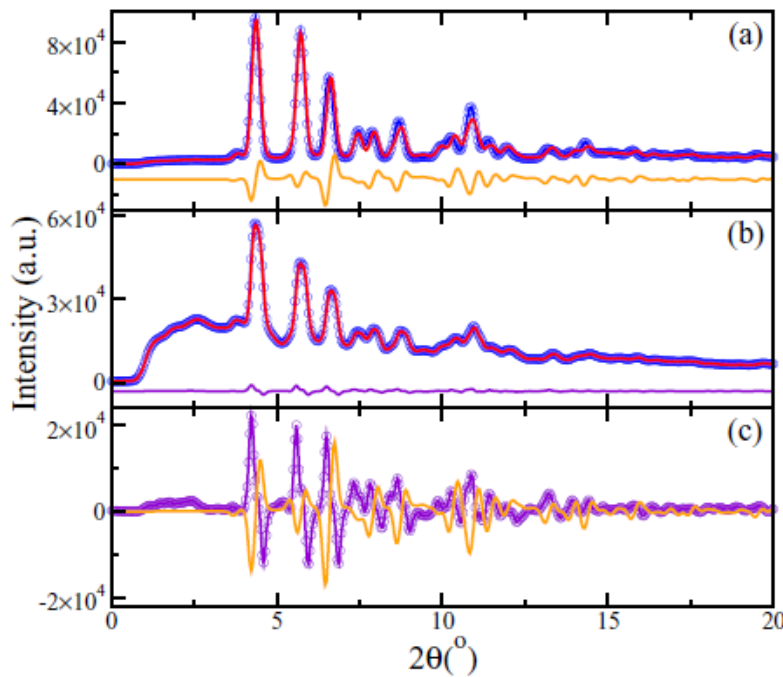


Figure 3.11 (a) The difference curves (orange) of diffraction data for bulk MnAs at 295 K (blue) and at 335 K (red); (b) The difference curves (violet) of diffraction data for type-A MnAs nanoparticles at 295 K (blue) and 335 K (red); (c) comparison of the (a) and (b) difference curves. The orange curve has been enlarged by a factor of 10.

plot for type-B MnAs nanoparticles (the curve had to be expanded 10 times for comparison to bulk MnAs) suggests the structural changes in type-B within this temperature range are small.

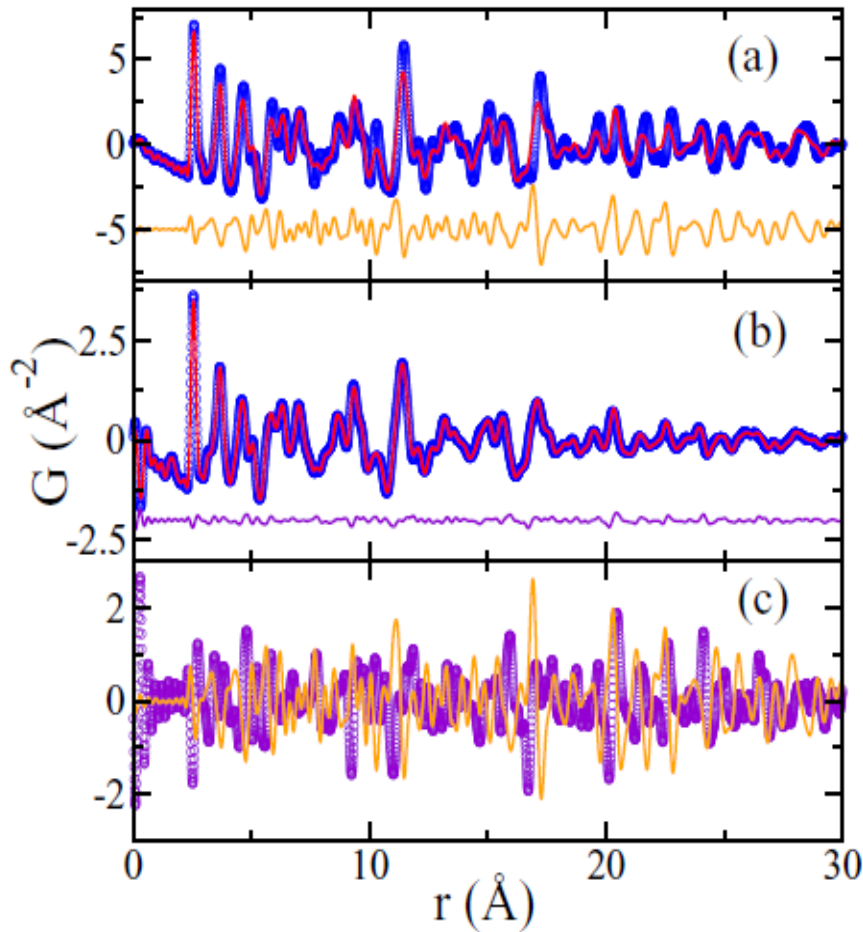


Figure 3.12 (a) The difference curves (orange) of PDF data for bulk MnAs between at 295 K (blue) and at 335 K (red); (b) The difference curves (violet) of PDF data for type-B MnAs nanoparticles at 295 K (blue) and 335 K (red); (c) comparison of the difference curves from (a) and (b). The orange curve has also been enlarged by a factor of 10 to enable a meaningful comparison.

Moreover, if a β model fit is applied to bulk MnAs and type-B MnAs nanoparticles over the same temperature range (Figure 3.13), no similarities in the lattice parameter changes are found as was the case for bulk MnAs and type-A MnAs nanoparticles. Bulk MnAs demonstrates an abrupt increase in \underline{a} , and decrease in \underline{b} and \underline{c} , all accompanied by a substantial hysteresis when the temperature is varied in the range from 305 K to 320 K. In contrast, type-B MnAs nanoparticles show a gradual increase in lattice parameters upon heating, attributed to regular thermal expansion, and only a small degree of irreversibility upon cooling.

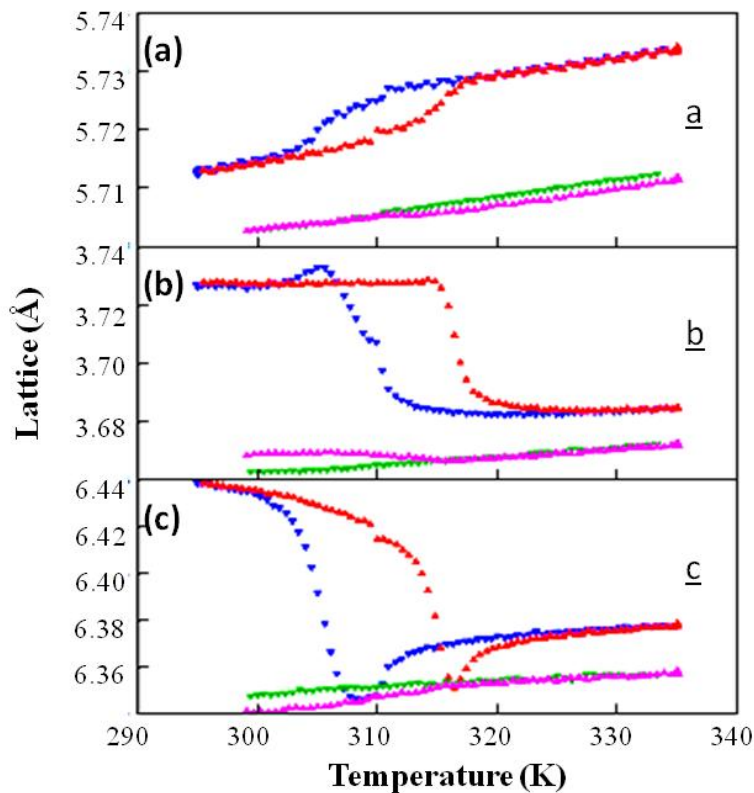


Figure 3.13 Comparison of lattice parameters from PDF refinements of bulk MnAs and type-B MnAs nanoparticles to the β -phase structure model upon heating from 295 K to 335 K (red for bulk and cyan for type-B nanoparticles) and cooling back from 335 K to 295 K (blue for bulk and green for type-B nanoparticles): (a) lattice parameter \underline{a} , (b) lattice parameter \underline{b} , (c) lattice parameter \underline{c} .

Considering that the transformation in MnAs between α and β is a first order magneto-structural phase transformation, the structural changes observed between 295 K and 335 K in bulk and type-A MnAs nanoparticles should be coupled to changes in the magnetism. The magneto-structural coupling data is shown in Figure 3.14. The structure parameter shown in this figure is the volume of the unit cell (α -model), while the magnetic parameter is the magnetic susceptibility. The red and blue curves in Figure 3.14(a) and (b), which reflect the structural and magnetic transitions of bulk MnAs, are strongly correlated. The curves colored with cyan and magenta show the transition of the type-A nanoparticles. Although the hysteresis of the structural change is smaller than that of the magnetic, the magnetic and structural transitions still appear to be coupled. When compared to bulk MnAs, the increase in the magnetization upon cooling is smaller, which is correlated with the smaller magnitude of the cell volume change. The hysteresis width for the magnetic data in type-A MnAs nanoparticles (1 K), is much narrower than that in bulk MnAs, whereas the width of the structural hysteresis in type-A MnAs nanoparticles is wider than that for bulk MnAs. These observations indicate that the structural and magnetic transitions for type-A MnAs nanoparticles are qualitatively, but not quantitatively, correlated.

The magnetic susceptibility data for the type-B MnAs nanoparticles is also plotted in Figure 3.14, and is distinct from type-A MnAs nanoparticles and bulk MnAs. At 335 K, the magnetic susceptibility of type-B nanoparticles is small, consistent with the low-spin paramagnetic state expected for the β -phase (and observed in bulk and type-A nanoparticles above the magnetic transition temperature). However, as the temperature decreases, there is a

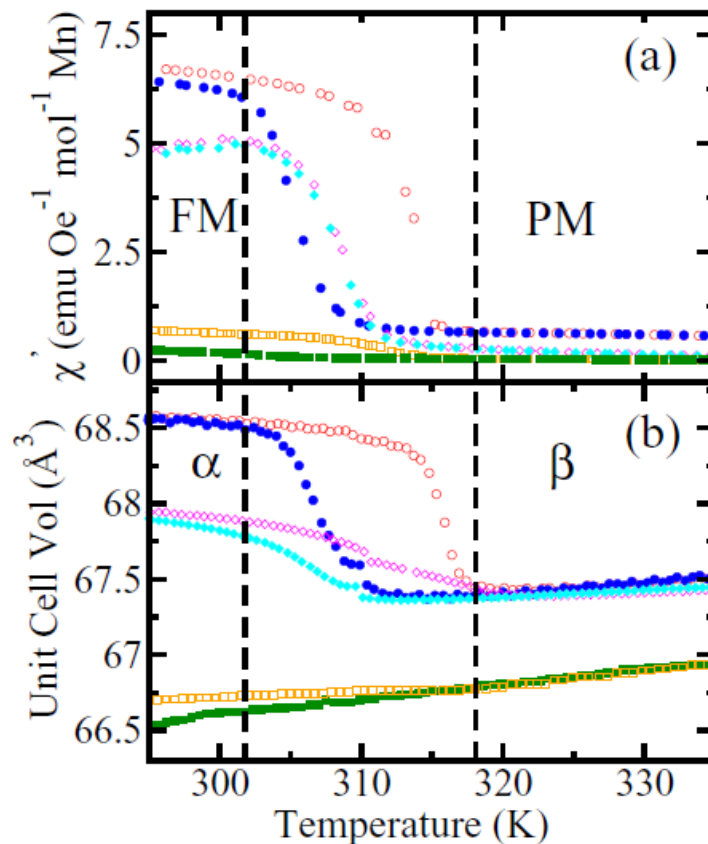


Figure 3.14 Comparison of AC magnetization (a) and unit cell volume (b) in bulk MnAs, type-A MnAs nanoparticles and type-B MnAs nanoparticles. All unit cell volumes are based on the refinements of the α -model. Dashed lines at 303 K and 317 K indicate the temperature range of the first order structural transitions of the bulk MnAs. The color settings are: blue (cooling, bulk), red (heating, bulk), cyan (cooling, type-A nanoparticles), magenta (heating, type-A nanoparticle), green (cooling, type-B nanoparticles) and orange (heating, type-B nanoparticles)

small but distinct increase in susceptibility that is not fully reversible, giving rise to a small hysteresis upon warming, also seen in lattice parameters. Thus, type-B MnAs nanoparticles are very different from type-A MnAs nanoparticles and bulk MnAs. Understanding the origin of the unique behavior of type-B MnAs nanoparticles is the subject of the next chapter.

3.4 Conclusion

PDF analysis and Rietveld refinement confirms that the structural transition and the magnetic transition are highly correlated in bulk MnAs and suggest that for type-A MnAs nanoparticles, there is a similar magneto-structural phase transition occurring in the same temperature region as that for bulk MnAs. This is in contrast to prior data conducted using traditional PXRD methods in the same temperature region. For type-B MnAs nanoparticles, the β -model fits well over the entire temperature range, distinct from both bulk MnAs and type-A MnAs nanoparticles. The absence of a magneto-structural phase transition in type-B MnAs nanoparticles is consistent with that type-B MnAs nanoparticles being kinetically trapped in the β -structure. The stability of type-B MnAs nanoparticles is the focus of the next chapter.

CHAPTER 4

Probing the Stability of MnAs Nanocrystals Prepared by Rapid Precipitation

4.1 Introduction

First-order structural phase transitions are of considerable academic and practical interest in mechanical engineering,⁷³ microelectronics,⁷⁴ magnetic refrigeration,⁷⁵ etc. Currently, studies of first order structural transitions in both bulk and nanoscale materials are mainly focused on the effect of external pressure,⁷⁶ a magnetic⁷⁷ or electric field⁷⁸ and temperature.⁷⁹ These studies indicate that the first order structural transition is highly dependent on external conditions applied and can be reversed as those conditions are changed. For nano-structured materials, due to the decrease in size, the energy barrier for the transformation is greatly reduced compared to the bulk material. If the energy barrier becomes small enough, structural fluctuations will occur between the two equilibrium structures^{80,9,10}. Recently, Zheng et al reported the trajectories of structural transformations in single nanocrystals with atomic resolution by electron microscopy techniques⁸¹ and reported that the decrease in particle size will help to stabilize the metastable intermediate structure. More and more details of the fluctuation dynamics in nucleation, phase propagation and pinning of structural domains by defects, is being revealed.⁸²

MnAs is of particular interest as a first order magneto-structural phase change material due to its near room-temperature transition temperature. The first-order magnetostructural phase transition for bulk MnAs from high spin ferromagnetic hexagonal structure (NiAs-type, α) to the low spin paramagnetic orthorhombic structure (MnP-type, β) occurs at 313-317 K, as shown in chapter 1, which makes MnAs a good candidate for information storage⁸³ and room temperature magnetic refrigeration applications.⁵³ In 2003, Mira et al reported that stabilization of the α -

MnAs phase above the phase transition temperature can be achieved by the application of an external magnetic field, indicating that the magnetic ordering and structural ordering are highly correlated, as expected for a magneto-structural transformation.⁸⁴ A recent density functional theory study revealed that giant spin-phonon coupling plays a crucial role in the mechanism of the type $\alpha \rightarrow \beta$ phase transition in MnAs.⁸⁵ This transformation is also a negative thermo-expansion process, as β -MnAs has a smaller unit cell than α -MnAs.

Intriguingly, when prepared on the nanoscale by arrested precipitation reactions at 250 – 330 °C, materials corresponding to either α or β -phase can be isolated at room temperature (298 K).^{38d} As described in Chapter 3, those samples that form the α -MnAs structure at room temperature (type-A MnAs nanoparticles) behave like bulk MnAs, and show the characteristic magnetostructural transition, whereas those samples that adopt the β -phase (type-B MnAs nanoparticles) do not show a structural transition in the range (295 K – 335 K), but do show a ferromagnetic transition close to that for type-A MnAs (315 K).⁸⁶ A previous study showed that over several months at room temperature, the type-B MnAs nanoparticles partially converted from the β -phase to the thermodynamically stable α -phase, consistent with metastability in type-B MnAs.^{38d} However, the process is very slow and samples do not always convert completely, and sometimes do not convert at all. In order to understand the mechanism of the phase transition in metastable type-B MnAs nanoparticles, we seek to determine the relationship between the transition temperature and the size of the nanoparticles. Here we report the synthesis of different sizes of type-B MnAs nanoparticles and the effect of size on the phase transformation temperature ($\alpha \rightarrow \beta$) and temperature range of the co-existence region of the two phases (hysteresis). These data are correlated with temperature dependent magnetic susceptibility data.

In this dissertation research, I synthesized the type-B MnAs nanoparticles with different sizes and performed routine characterization. Dixit, Rajesh and Lawes acquired the magnetic measurements.

4.2 Results and discussion

4.2.1 Synthesis and characterization of type-B MnAs

Type-B MnAs nanocrystals with different sizes were synthesized following the previous reported method with a modified procedure.^{38d} 1 mmol of $\text{Mn}_2(\text{CO})_{10}$, and 10 ml of 1-octadecene are mixed together in the glove box, then placed in a Schlenk flask. Before injection, the mixture is slightly warmed with a heat gun until the powder precursors are dissolved. The mixture is then cannulated under inert conditions into hot solvent containing 5 g TOPO and 1 mmol of triphenylarsine oxide maintained at 330 °C. The reaction time was varied between 1 to 15 hours to control the final particle size. Changing the reactant amount of $\text{Mn}_2(\text{CO})_{10}$ and triphenylarsine oxide also produces different sizes of nanocrystals, as shown in Table 4.1.

Type-A MnAs nanoparticles are synthesized as follows: 1 mmol of $\text{Mn}_2(\text{CO})_{10}$, 1 mmol triphenylarsine oxide, 10 ml of 1-octadecene and 5 g TOPO are mixed together in one Schlenk flask, which then was placed under vacuum and flushed with argon for 15 mins. After purging, the Schlenk flask was gradually heated to 250 °C at 1 °C/min. The final product was dispersed in chloroform and reprecipitated with ethanol before drying.

Table 4.1 Effects of reaction time and amount of coordinating ligand on the size of as-prepared type-B MnAs nanocrystals

	5g TOPO	10 g TOPO
1 hour	12 nm	8 nm
2 hour	18 nm	14 nm
5 hour	21 nm	-
10 hour	30 nm	-

X-ray diffraction (XRD) measurements were employed to determine the phase and the size of synthesized Type-B MnAs nanocrystals. Data as shown in Figure 4.1 were acquired on a Rigaku 200 B model X-ray diffractometer equipped with a rotating Cu anode source. The peak positions match the drop-lines for the β -MnAs standard (PDF# 710923). The average size of the nanocrystals was estimated using the Debye-Scherrer equation and using the full width at half maximum (FWHM) of the $2\theta = 32.1^\circ$ reflection (the (202) reflection).

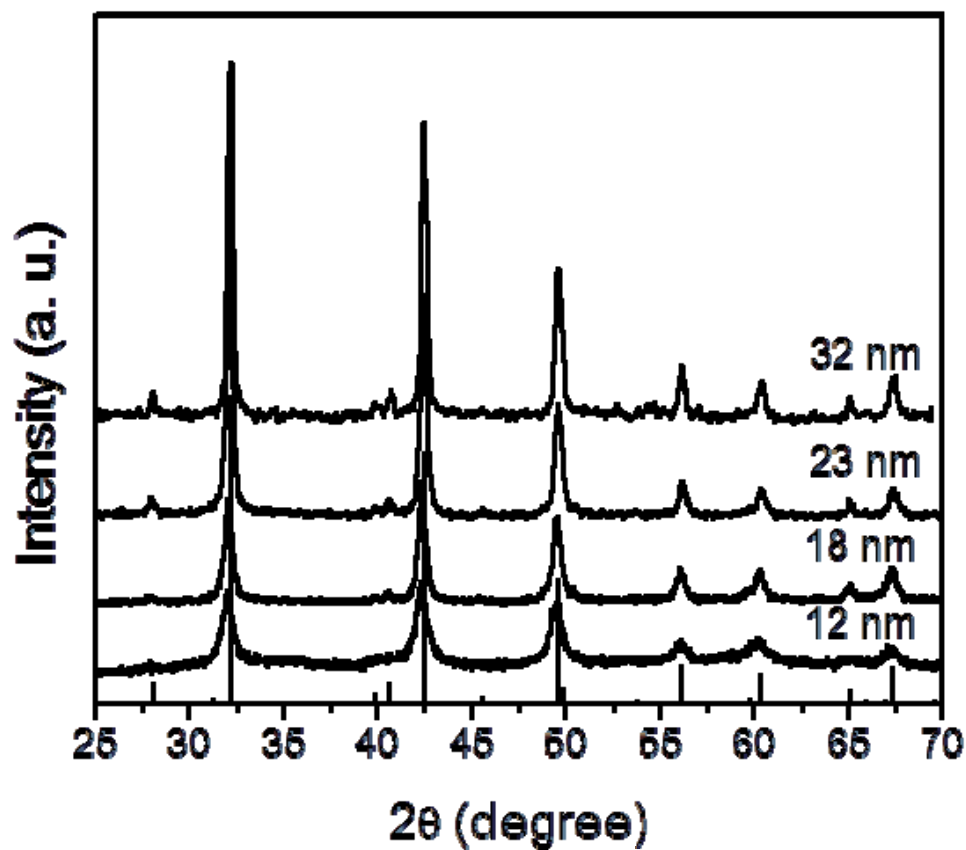


Figure 4.1 The XRD patterns of synthesized Type-B MnAs nanocrystals prepared using 5g of TOPO at different times. The drop lines indicate the reference spectrum of the β -MnAs standard (PDF# 71-0923).

TEM images of these synthesized Type-B MnAs nanocrystals are recorded using a JEOL 2010 HR transmission electron microscope operated at 200 kV. The samples for TEM were prepared by placing one drop of chloroform containing the dispersion of as prepared nanoparticles onto a 200 mesh Cu grid coated with a carbon film. Figure 4.2 shows the morphology and monodispersity of the Type-B MnAs nanocrystal samples. In Figure 4.3, the average crystallite sizes with standard deviations as determined from TEM are indicated. The nanoparticle sizes are measured from the core, as the shell is non-crystalline. The sizes measured from TEM match those obtained by PXRD, within 1 – 2 nm.

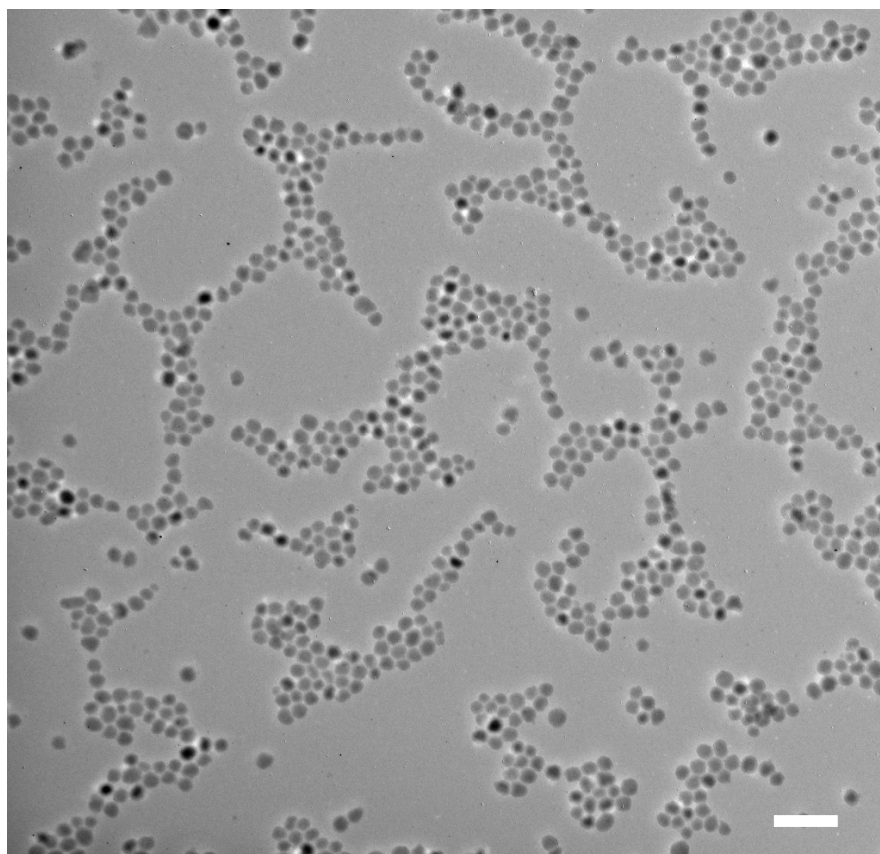


Figure 4.2 TEM image of type-B MnAs nanoparticles indicating highly uniform 18 nm samples are prepared (scale bar = 100 nm).

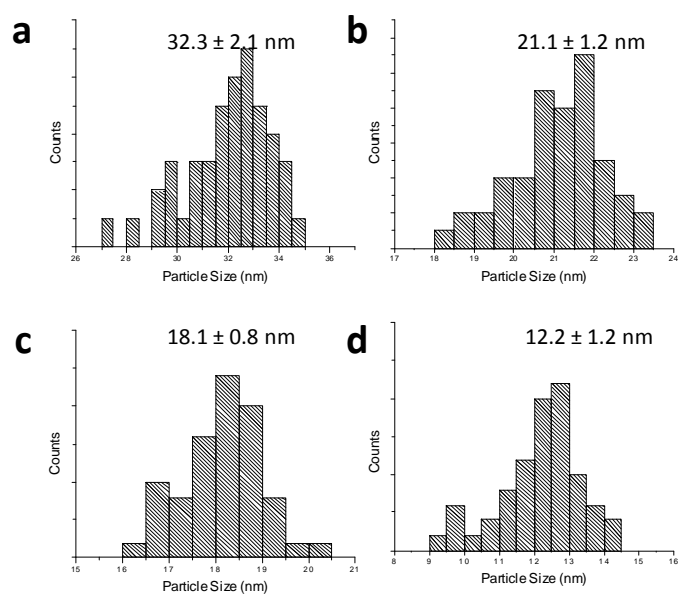
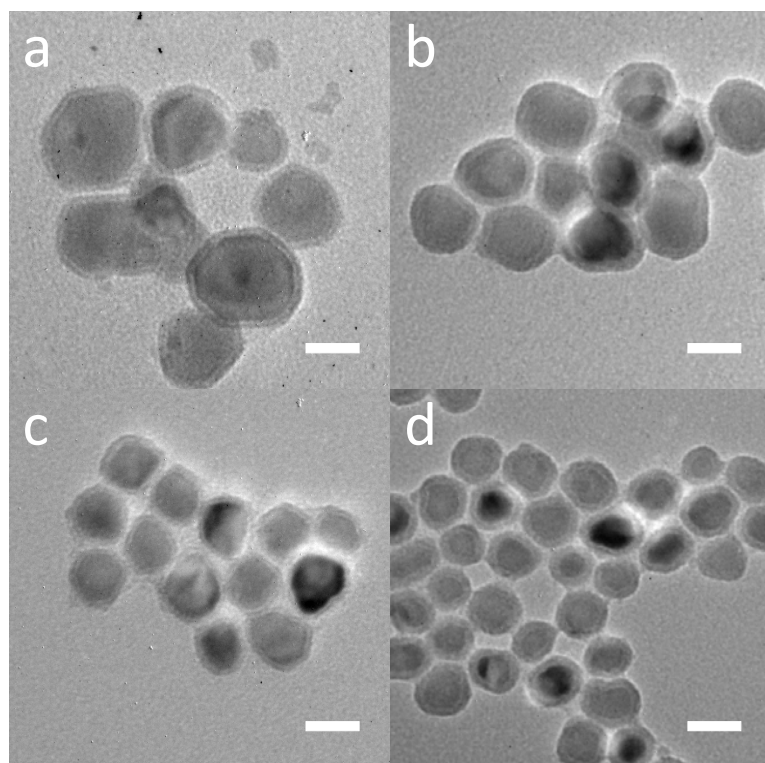


Figure 4.3 TEM images and size distribution histograms of synthesized Type-B MnAs nanoparticles with different sizes (the scale bar is 20 nm): (a) 32 nm; (b) 21 nm; (c) 18 nm; (d) 12 nm.

4.2.2 The stability of type-B MnAs

In order to access the thermodynamically stable α phase in type-B MnAs nanocrystals, we sought to overcome the kinetic barrier by heating. However, even heating up to 120 °C does not seem sufficient, since the sample remains unchanged, as shown in Figure 4.4. This suggests that the transformation of β to α in type-B MnAs nanocrystals cannot be simply explained by a thermal energy barrier.

A careful structural evaluation of type-B MnAs nanoparticles reveals a compression of lattice parameters relative to bulk β -MnAs at 295 – 335 K. Compared to bulk-MnAs, the unit cell volume in type-B MnAs nanoparticles has shrunk by 2.71% at 295 K (below T_P for bulk MnAs) and 0.89% at 335 K (above T_P) for the β structure model fit; as for type-A MnAs nanoparticles, the shrinkage is only 0.7% at 295 K and 0 at 335 K (no shrinkage) compared to bulk MnAs for the α structure model fit. At 335 K (above T_P), the lattice parameter a obtained from the fits to

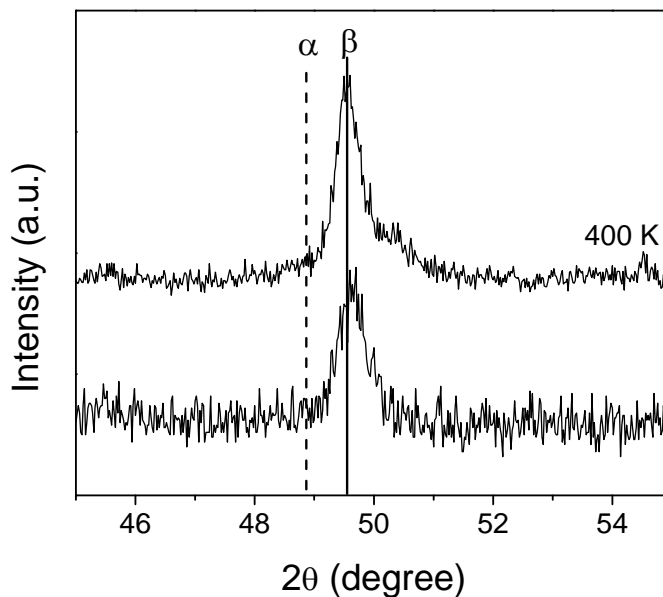


Figure 4.4 XRD image of 21 nm β MnAs nanocrystal before and after heating at 393 K

the β -MnAs structure in bulk MnAs, converted type-A MnAs nanoparticles and type-B MnAs nanoparticles are 5.734 Å, 5.728 Å and 5.713 Å, respectively.⁸⁶ Accordingly, we hypothesized that T_P for type-B MnAs nanoparticles may occur at a lower temperature due to the lattice parameter compression. The lattice parameter compression could arise from surface strain or incorporation of an impurity. In order to evaluate whether type-B MnAs nanoparticles are inadvertently doped, the elemental composition of MnAs nanocrystals was analyzed using high angle annular dark field scanning transmission electron microscopy (HAADF-STEM) and elemental analysis (EDS). HAADF-STEM data was collected by Dr. Yi Liu at Oregon State University using a FEI Titan 80-200 TEM/STEM with ChemiSTEM Capability. Figure 4.5

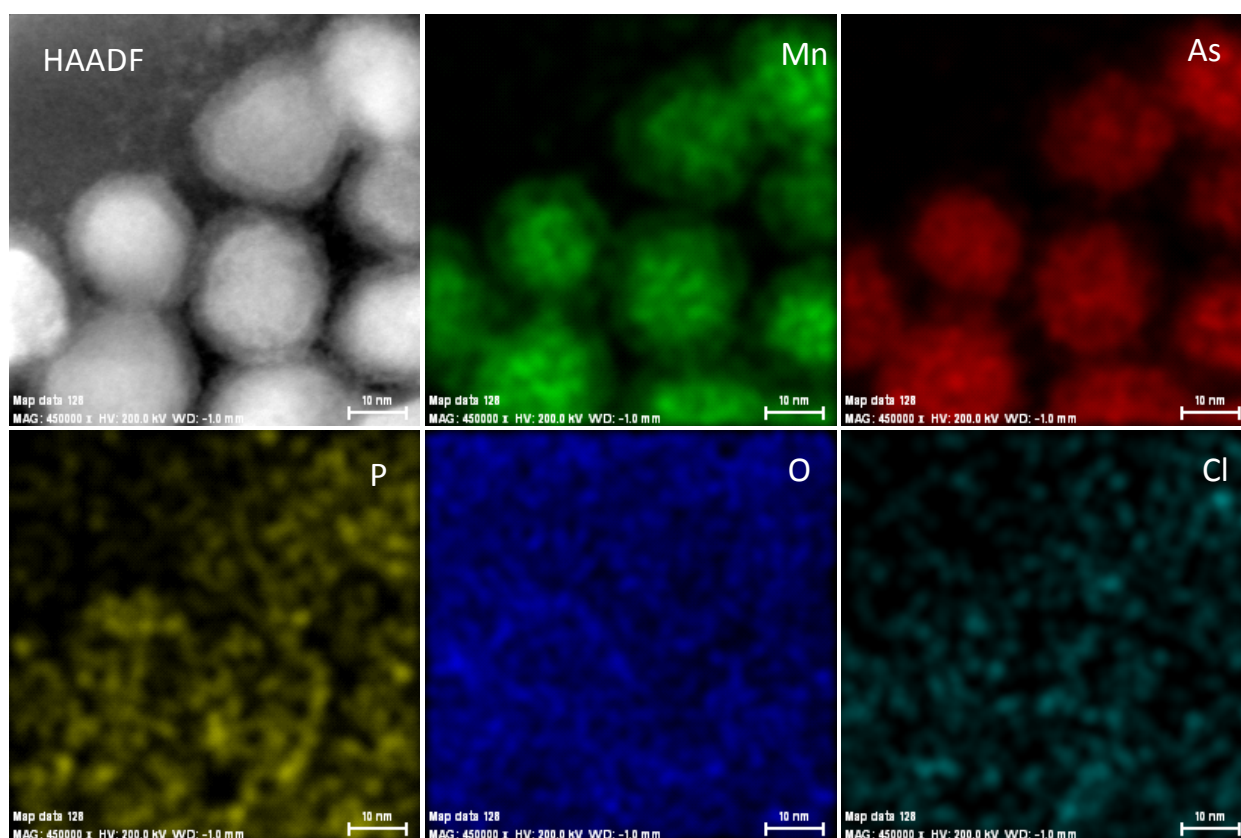


Figure 4.5 HAADF of type-B MnAs nanoparticles and elemental analysis maps for Mn, As, O, P and Cl, respectively.

shows a high angle annular dark field scanning transmission electron microscopy (HAADF-STEM) image and elemental mapping (EDS) for type-B MnAs.

For Mn and As, the signal is very intense in both the crystalline core and the amorphous shell of the nanoparticles. However, there is also some trace amount of P in the shell and the lattice, presumably arising from the decomposition of the coordinating solvent, TOPO, used in the reaction.⁸⁷ EDS chemical analysis shows there is trace amount of P exist (see Figure 4.6). Atomic substitution of P for As is known to decrease the lattice parameter and consequently the $\alpha \rightarrow \beta$ transition temperature.⁸⁸ Cl and O are also found as background signals attributed to the solvent CHCl_3 and ethanol/air oxidation, respectively. In contrast, HAADF-STEM analyses of type-A MnAs (see Figure 4.7), do not show P incorporation or chemical doping in the lattice.

The line profile elemental analysis also been performed for several single Type-B MnAs nanoparticles in a line (Figure 4.8). The data shows that there is no obvious difference for P distribution in the type-B MnAs nanoparticles, suggesting that the P could exist in both core and shell of the nanoparticles.

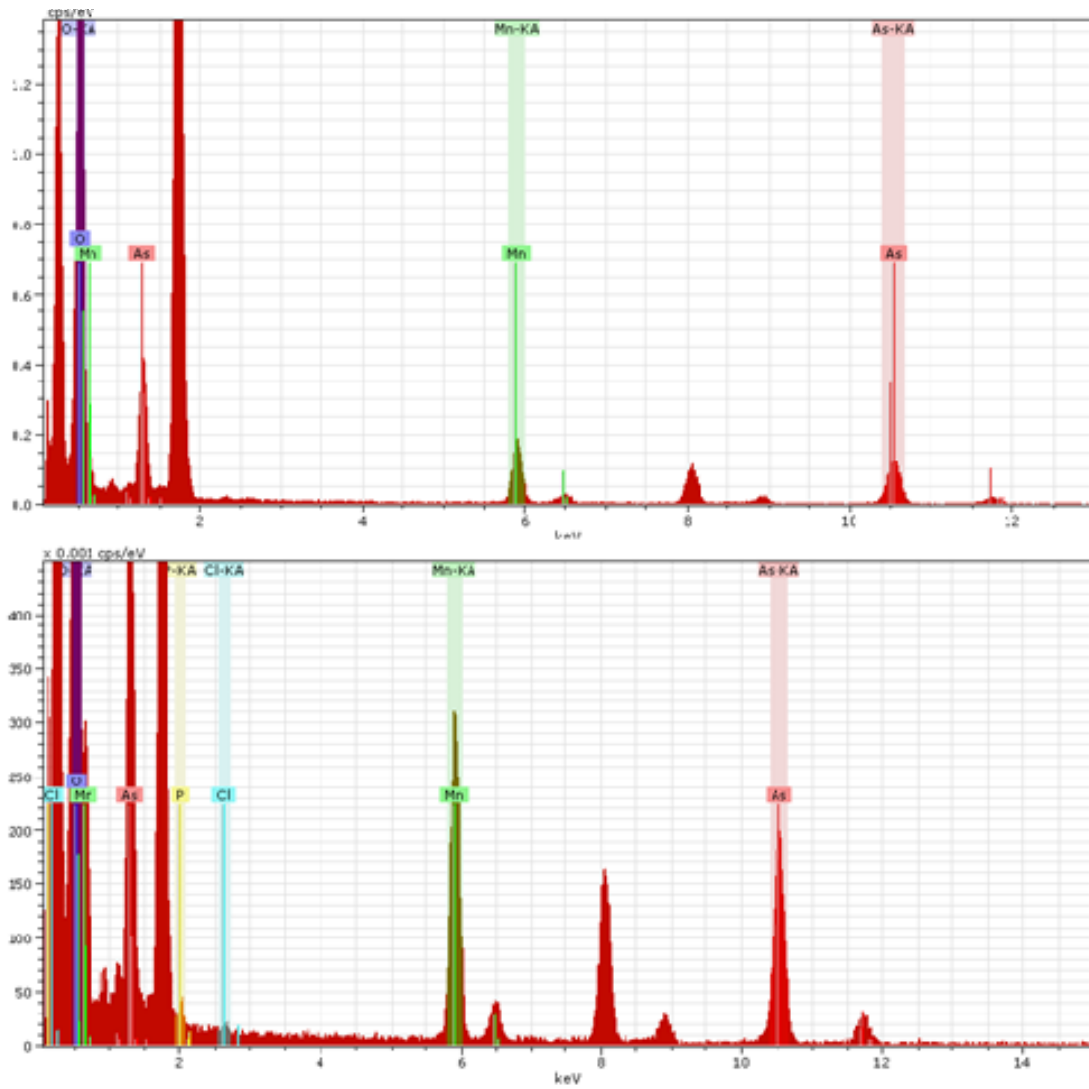


Figure 4.6 EDAX comparison of the composition for type-A (top) and type-B (bottom) MnAs nanoparticles

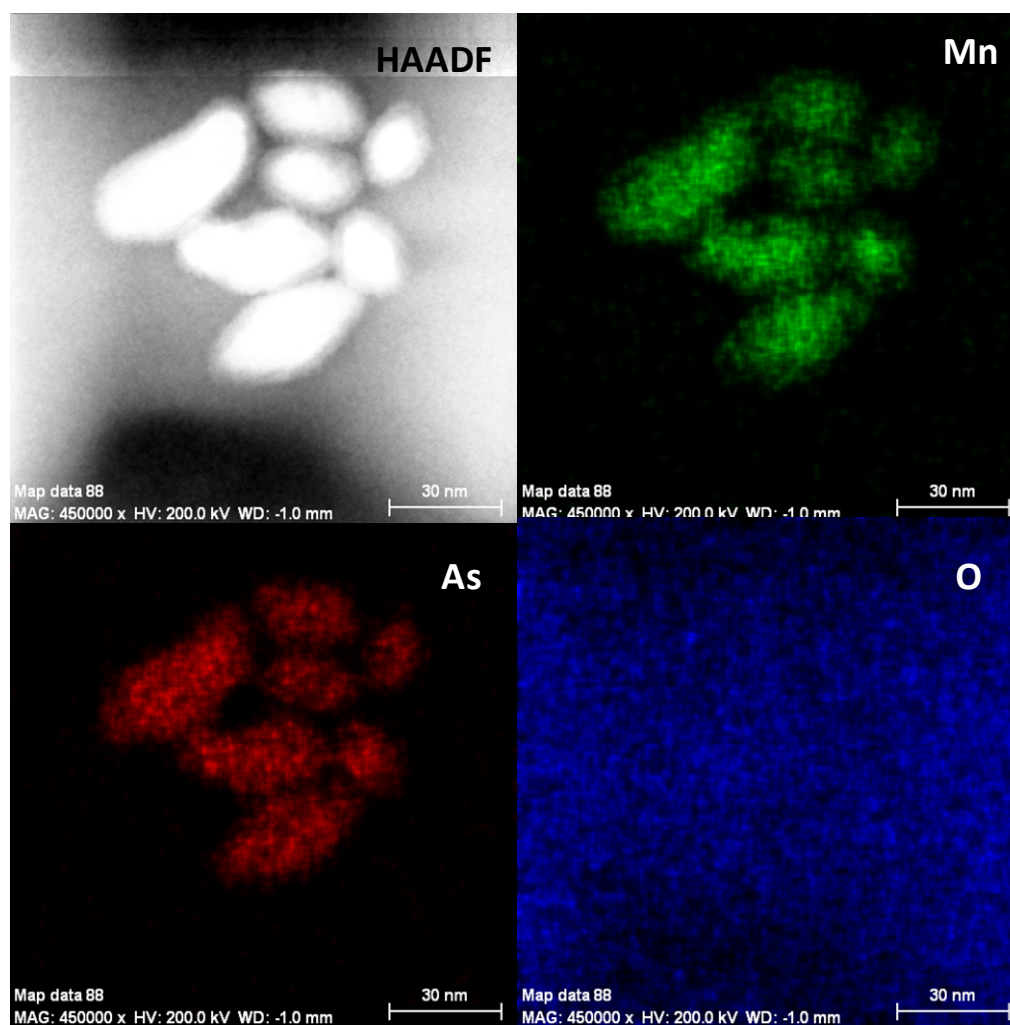


Figure 4.7 HAADF image and EDS map for type-A MnAs nanoparticles (no P or Cl is detected)

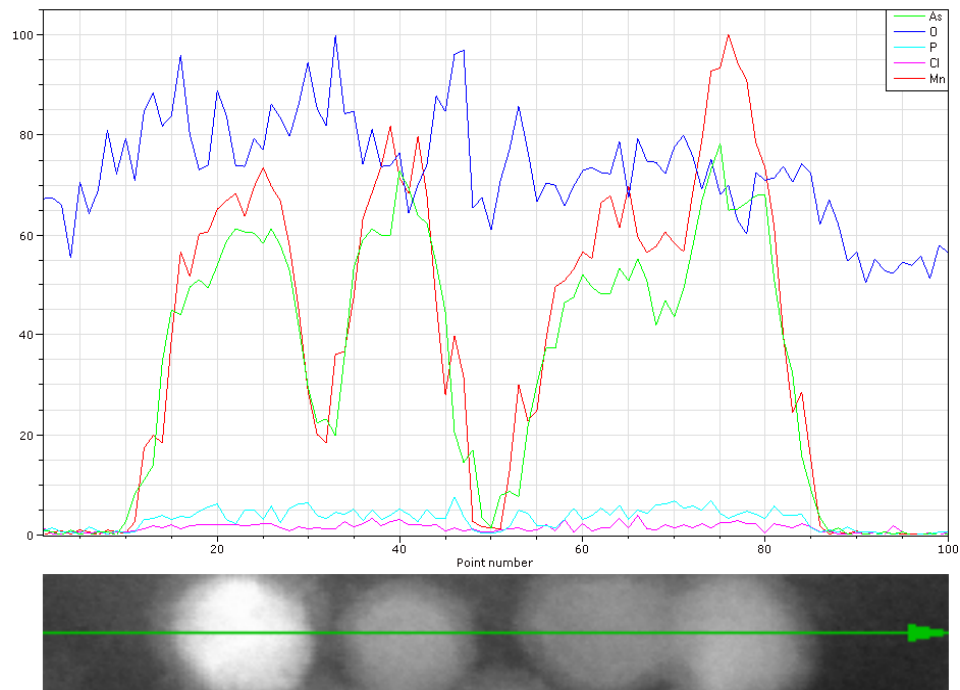


Figure 4.8 Line profile elemental analysis for several single Type-B MnAs nanoparticles.

In order to assess whether the room temperature stability of β -MnAs in type-B nanocrystals is due to a lowering of the phase transition temperature (T_P), due to contraction of the lattice upon doping, T-dependent XRD studies were undertaken. Figure 4.9 shows the temperature dependent XRD of the synthesized type-B MnAs upon cooling. Upon cooling to $-30 \sim -120$ °C, the (013) peak of β -MnAs disappears and a new peak grows in corresponding to the (110) reflection of α -MnAs, which indicates that the type-B phase has converted from β to α . However, when warmed back to room temperature, only part of the transformed α phase converts back to the β phase. The full conversion back to the β structure only happens when the temperature is increased to 50 °C. This suggests that the transformation of type-B MnAs

nanoparticles from β to α on cooling is reversible upon warming, but with a large hysteresis. Accordingly, the coexistence of the α structure and β structure depends on the temperature and the process history (cooling or warming) of the sample.

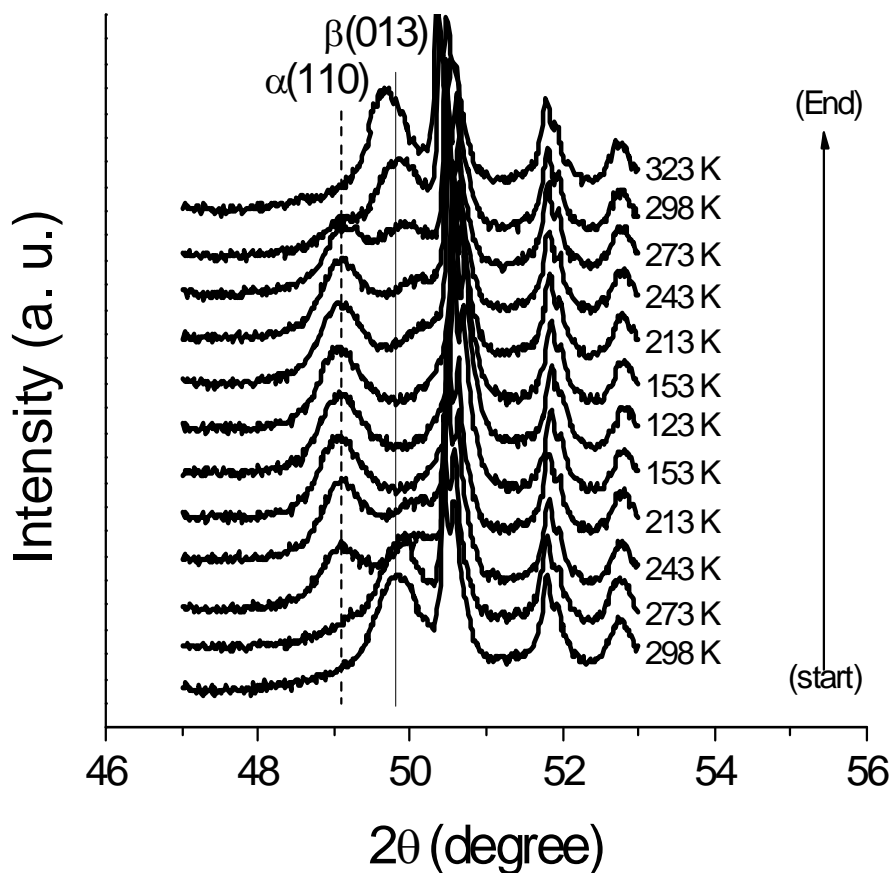


Figure 4.9 Temperature dependent XRD for type-B MnAs nanoparticles cooling to $-150\text{ }^{\circ}\text{C}$ and then warming back to room temperature (from bottom to top)

As mentioned before, type-B MnAs nanoparticles are not stable and will gradually transform from the β structure to the α structure at room temperature. However, it usually takes several months and the transformation is not always complete. As shown in Figure 4.10, the

effect of aging (several months) on structure for type-B MnAs and the effect of applying a cooling process (77 K for several hours followed by warming back to room temperature) are compared, the cooling process results in an enhanced and rapid conversion of the β phase to the α phase (< 3 hours). This is likely due to the establishment of a new quasi-equilibrium in the system.

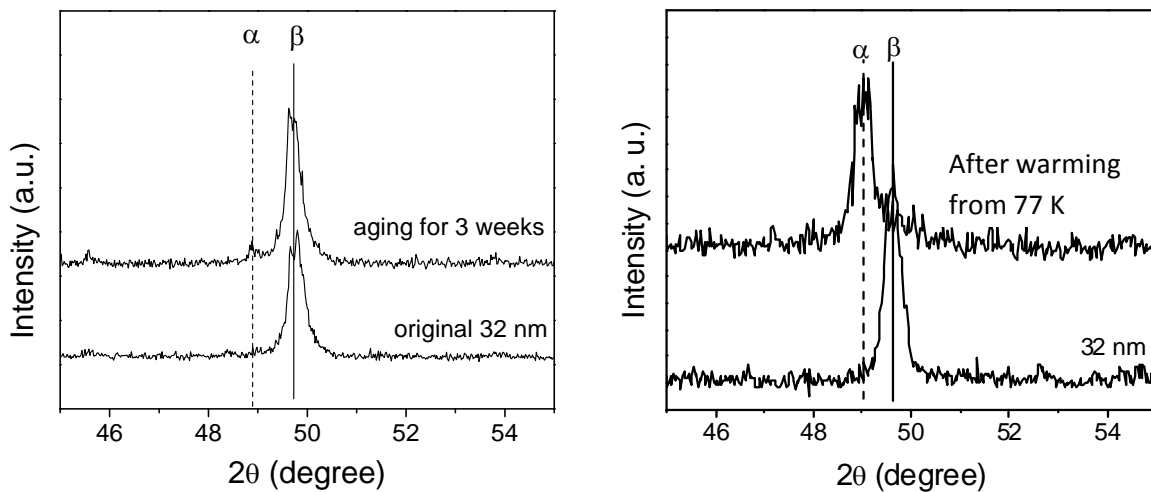


Figure 4.10 XRD image comparison for 32 nm nanocrystals after aging for 3 weeks (left) and after cooling at 77 K and then rewarming to room-temperature (right).

Figure 4.11 shows the high-resolution transmission electron microscopy (HRTEM) images of a representative type-B MnAs nanocrystal taken before and after cooling. Fast Fourier Transform (FFT) processing of the images reveals that the phase has been converted from the

orthorhombic β structure to the standard hexagonal α structure, confirming the transformation has occurred.

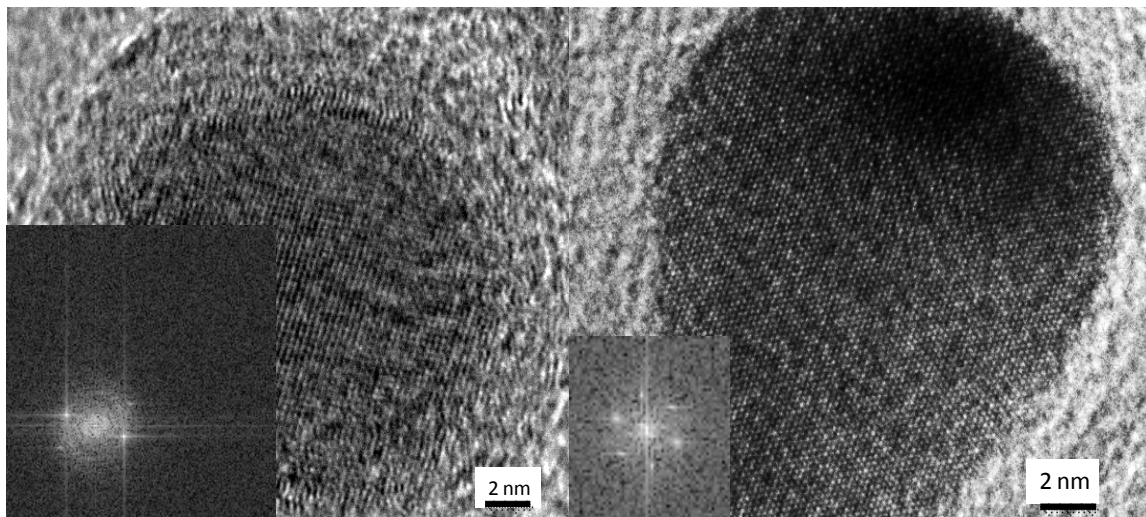


Figure 4.11 High resolution TEM images and FFT processing of a type-B MnAs nanocrystal before cooling (left) and after warming to room temperature from 77 K (right).

4.2.3 Magnetic Measurements

Since the structure and the magnetic properties are highly correlated in MnAs, magnetic measurements also shed light on the structural transition. Bulk MnAs is paramagnetic at and above 315 K when it adopts the β structure, while the lower-temperature magnetic properties of the β -MnAs structure are unknown because the phase is not stable below 315 K (or above 373 K) under ambient conditions (the α structure is formed). However, when the size is decreased to the nanoscale, the β structure of MnAs can be stabilized at lower temperatures and appears to be ferromagnetic. This is not unexpected as MnP, which adopts the β structure over a large T range,

is revealed to be ferromagnetic with a T_C of 290 K. Molar magnetic susceptibility data on type-B MnAs nanocrystals adopting the β structure are shown in Figure 4.12. The curves for each sample with transition temperature indicated are shown in Figure 4.16. It is evident that the type-B MnAs nanocrystals are ferromagnetic, as previously reported, but with a lower T_C on cooling than seen in type-A MnAs nanocrystals adopting the α structure (311 K). The hysteresis of 18 nm sample have two mixed features may be caused by the α -MnAs impurity. On the other hand, these data explain our erroneous report that $T_c(A) = T_c(B)$,^{38d} because data on type-B MnAs were acquired upon heating from 10 K. Presumably, at this temperature, the type-B MnAs nanoparticles converted from β to α , and the α structure will be retained due to the enlarged hysteresis, thus the magnetic data were acquired on α -phase in type-B MnAs.

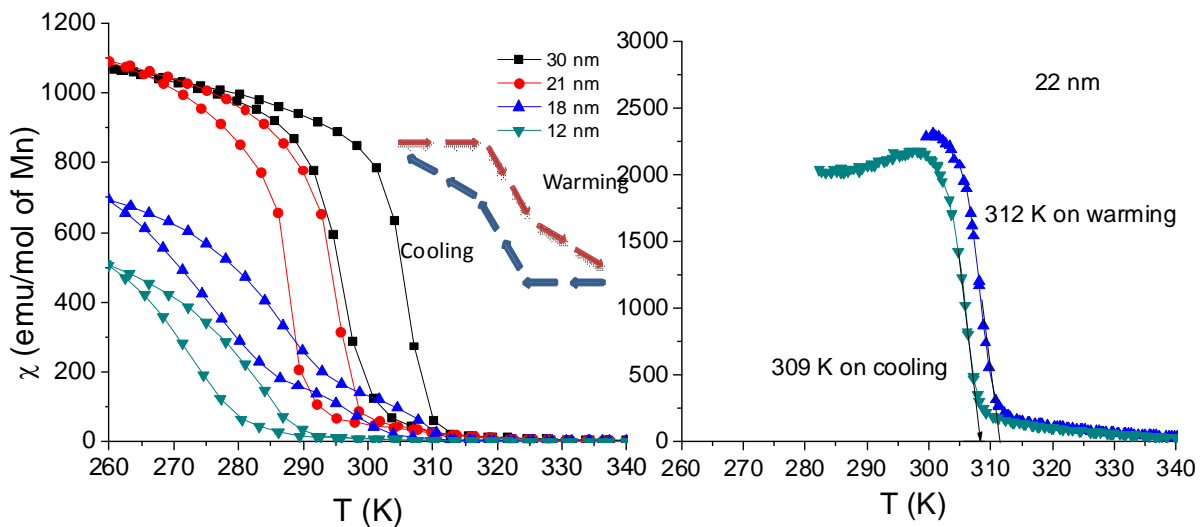


Figure 4.12 Comparison of the T-dependent magnetic susceptibility (magnetic susceptibility per mole of Mn) for type-B MnAs nanocrystals (from 12 to 30 nm, left) and type-A MnAs nanoparticles (22 nm, right)

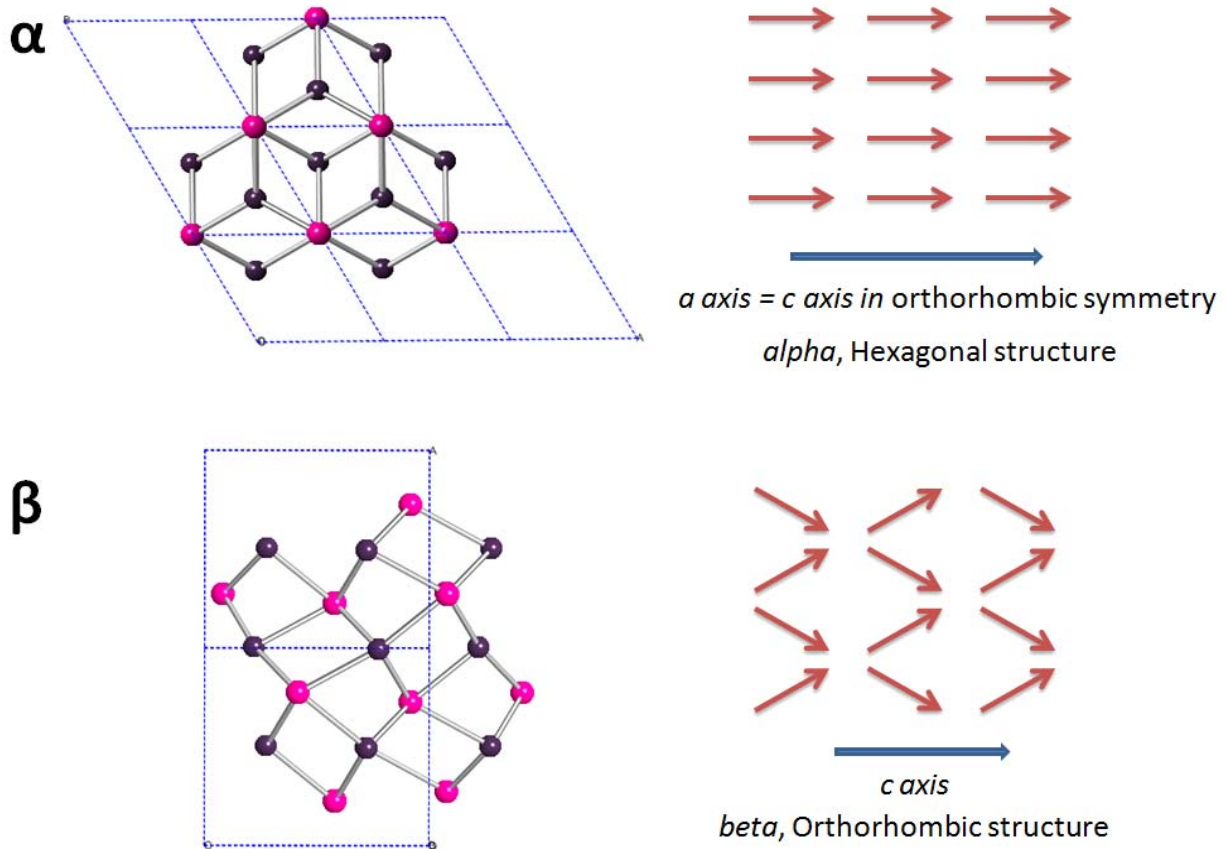


Figure 4.13 Modeling of magnetic structure of α and β MnAs (the spin orientation are in the same direction).

Previous neutron diffraction data shows the canted magnetic structure in orthorhombic $\text{MnAs}_{0.92}\text{P}_{0.08}$ structure.⁸⁹ As the β structure of MnAs is the same structure as MnP,^{47b} the magnetic structure of the ferromagnetic phase can be inferred as shown in Figure 4.13. When a reduced symmetry is chosen for both α and β structures, it is clear that the moment direction is the same in both structures. However, in the β -MnAs structure, the canting of the spin orientation

leads to a reduced magnetic moment in β -MnAs relative to α . Indeed we see moments of 1100 emu/mol for the type-B MnAs nanoparticles, relative to 2300 emu/mol for type-A nanoparticles at 260 K. These data are consistent with those observed. In the $\text{MnAs}_{1-x}\text{P}_x$ solid solution study, in which the saturated magnetization in $\text{MnAs}_{1-x}\text{P}_x$ adopting β -MnAs structure when $x > 0.03$, is about half of the magnetic moment in hexagonal α -MnAs.^{80a} Accordingly, we expected that the structural phase transition will have a corresponding magnetic moment change.

Figure 4.14 shows the magnetic moment of the 21 nm type-B MnAs after cooling to 77 K. A clear increase by 25% of the saturated magnetic moment is consistent with the retained phase transformation and this is confirmed by XRD (Figure 4.14 right) which shows a portion of the sample now adopts the α -MnAs structure at room temperature. The area of retained α peak is

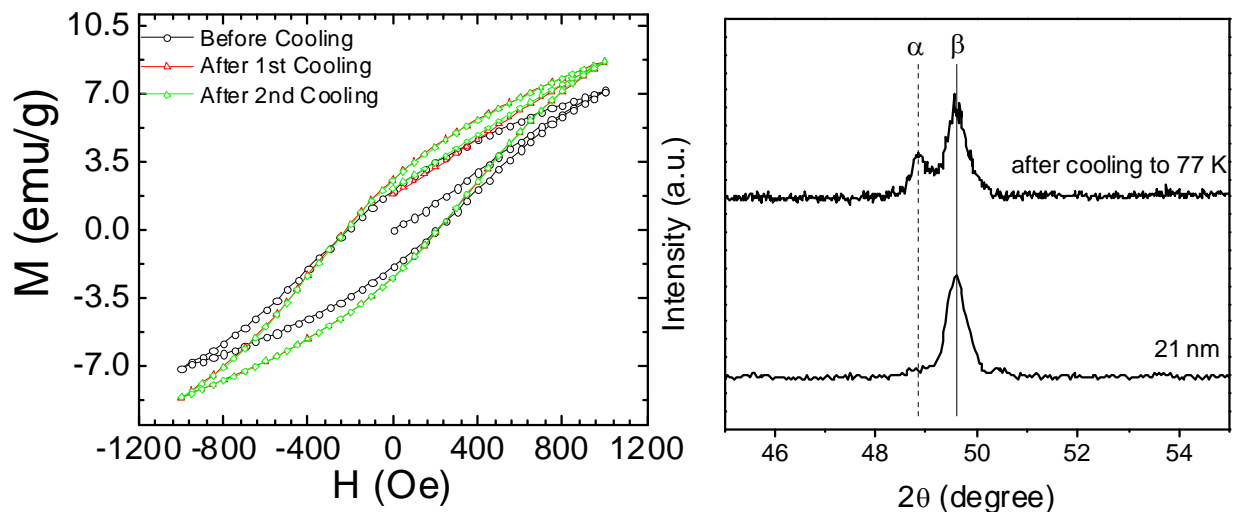


Figure 4.14 (left) DC magnetization acquired at 300 K for 21 nm type-B MnAs nanoparticles before and after cooling to 77 K and returning to room-temperature; (right) XRD of 21 nm type-B MnAs nanoparticles at room temperature before and after cooling to 77 K.

about 1/3 of the remaining β peak, suggesting there is about 25% phase change. Considering,

based on the above analysis, the moment of Mn in α MnAs is about twice that in β MnAs, the magnetic moment change matches the XRD peak area change very well.

For MnAs, the phase transformation can be caused by either temperature or applied magnetic field. To clarify that the hysteresis is enhanced due to the decreased size, an external field of 5 T was applied to as prepared type-B MnAs nanoparticles of size 21 nm in diameter. After applying the external 5 T magnetic-field, there is a distinct increase in the magnetic moment and a shift in the T_c onset from 291 K to 297 K, suggesting the transformation has occurred. In order to verify that the increased moment was not just due to magnetic alignment, we re-measured the magnetic moment after removing the applied field, and found the moment to be unchanged. The saturated magnetization was also the same when the same sample was re-

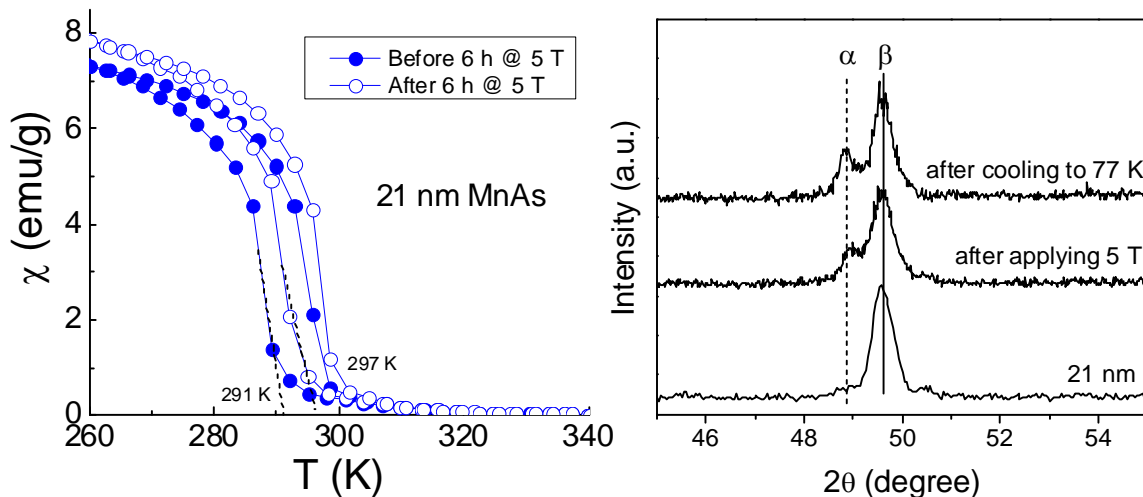


Figure 4.15 XRD data comparison for 21 nm type-B MnAs nanoparticles after cooling and returning to room-temperature and after being under a 5 T field.

measured after 4 days without applying any magnetic field. The corresponding XRD images for samples either cooled or to which 5 T field was applied are shown in Figure 4.15 and show that

the transformations induced by cooling or by applying an external field are comparable. As with the T-dependent XRD data (Figure 4.9), we surmise this history-dependent phase stability arises from applying perturbations to sample, within the phase coexistence temperature region.

4.2.4 Size dependent magneto-structural phase transformation

Previous studies of pressure-induced phase transformations have shown that pressure is inversely related to size in phase transformation.^{76a} For example, in CdSe nanocrystals, the

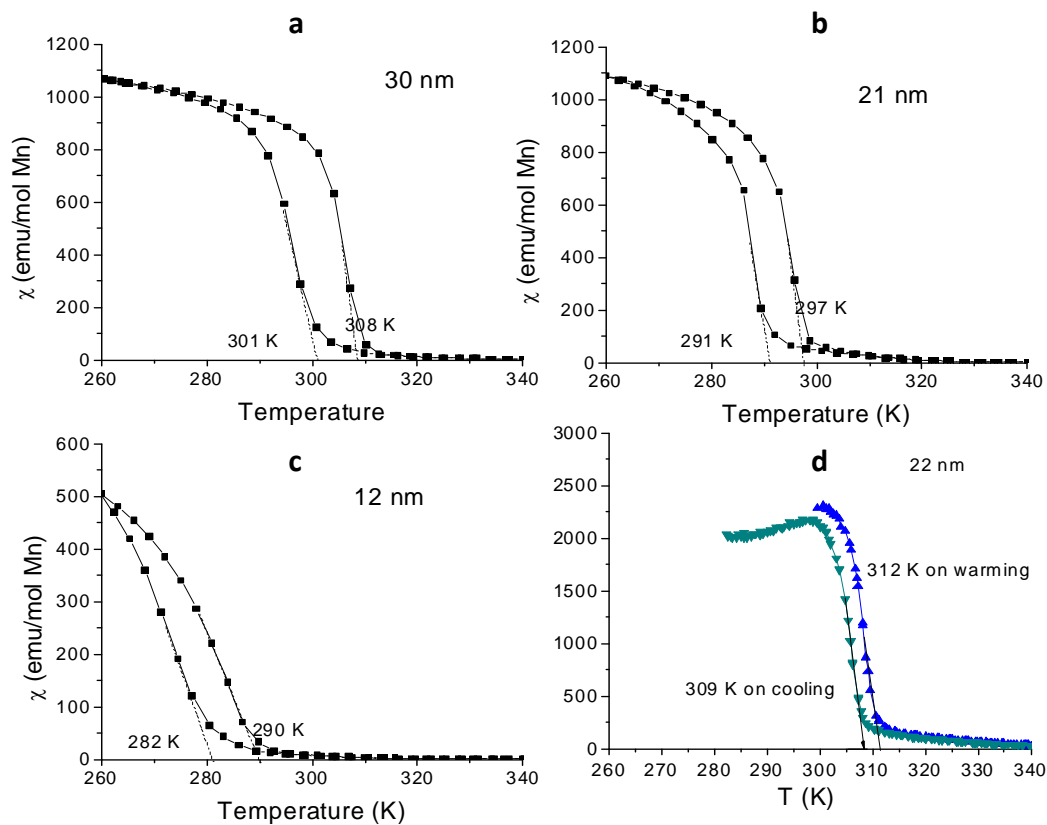


Figure 4.16 Magnetic moment measurements of MnAs nanoparticles: (a) 30 nm type-B, (b) 21 nm type-B, (c) 12 nm type-B, and (d) 22 nm type-A.

stability of the structure to with stand the applied pressure is about 2-3 times greater for

nanocrystal than for the bulk material⁹⁰. To explore the effect of size on the $\beta \rightarrow \alpha$ phase transformation of MnAs nanoparticles and assuming a strong correlation between the magnetic transition and the structure change, the magnetic susceptibility data of different sizes of type-B MnAs nanoparticles were acquired and data are shown in Figure 4.16 and summarized in Table 4.2. As the nanoparticle size increases from 10 nm to 30 nm, both the magnetic moment and the T_C increase, which indicates that the magneto-structural phase transformation in type-B MnAs nanoparticles is also size dependent. The portion of the α -phase retained after warming back will rely on the size of the particles. As shown In Figure 4.17, for the 32 nm samples, the α phase converted from the β phase during cooling is completely retained upon returning to room temperature, whereas for the 21 nm samples, only part of the α structure is retained after reheating, and for the 12 nm sample, none of the α is retained. These data suggest that the larger the nanocrystal size is, the more bulk-like the sample is (The T_p will be closer to that of bulk MnAs, $\sim 313 - 317$ K). In Figure 4.18, evaluation of a polydisperse sample with 32 nm average diameter (by XRD) after cooling at 77 K and reheating to room temperature indicates only part of the sample retains the α -structure, in contrast to what is seen for a monodisperse sample. Careful evaluation of the peak breadths suggests that it is the larger particles (avg. 58.4 nm calculated from the Scherrer Equation) that retain the α structure, whereas smaller particles (avg. 16.1 nm) converted to β upon reheating. The fact that only large nanoparticles retain the α phase while small nanoparticles retain the β structure upon warming from low temperature, indicates differences of the phase transformation temperature and hysteresis regions for different sizes.

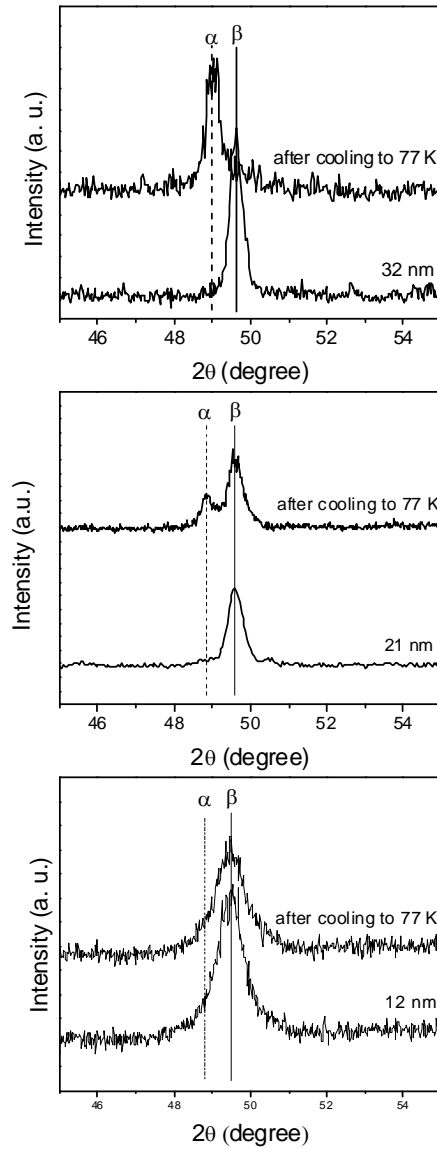


Fig. 4.17 XRD measurements of different sizes of type-B MnAs nanoparticles upon warming to room temperature from 77 K. To clearly differentiate the structure, a $2\theta = 45^\circ \sim 55^\circ$ window is selected out for comparison. The solid drop-lines are the standard β -phase MnAs reference (PDF# 71-0923) and the dash drop-lines are the standard α -phase MnAs reference (PDF# 28-0644).

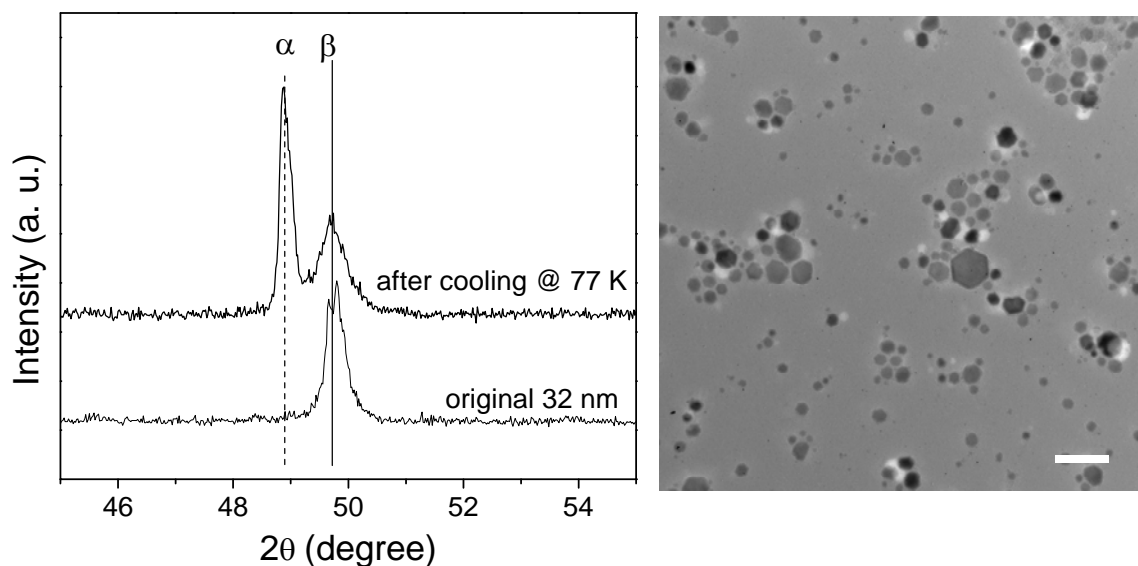


Figure 4.18 Room temperature XRD patterns (left) and TEM images (right) of polydisperse 32 nm (average) type-B MnAs nanoparticles before and after cooling to 77 K

The difference of the transition temperature could be caused by the lattice parameter change, which could be related to finite size effects and/or impurities. Both structural and magnetic order can be affected by the finite size of nanoparticles.⁹¹ Near the nanoparticle free surface, the average lattice parameter is reduced due to the contraction of the bonds. Thus, the magnitude of the magnetic moment per atom near the surface is reduced drastically due to the band narrowing.⁹² The surface coordination for smaller nanoparticles is more affected by the increased overlapping of the orbitals and decreased magnetic moment, thus β structure is more preferred. Previous studies of MnAs films on GaAs by Iikawa and coworkers have confirmed that GaAs could distort the MnAs film by contraction of the lattice parameter, which results in a reduction of the T_p .⁹³ In order to understand the origin of the size dependent T_p , detailed studies of size-dependent lattice parameters and quantification of dopants is needed.

Table 4.2 Comparison of the magnetic data for 12 nm, 21 nm, 30 nm (type-B), and 22 nm (type-A) MnAs nanoparticles. (T_C values were estimated from the onsets)

	12 nm type-B	21 nm type-B	30 nm type-B	22 nm type-A
T_c on cooling (K)	282	291	301	309
T_c on warming (K)	290	297	308	312
Average (K)	286	294	304	311
Mag. Sus. @ 260 K (emu/mol Mn)	500	1100	1100	2200

4.4 Conclusions

In summary, we have observed that type-B MnAs nanoparticles prepared by rapid arrested precipitation undergo a transformation from β to α upon cooling to 77 K. Temperature dependent XRD studies and magnetic measurements suggest that the T_P is suppressed to lower temperatures and that the transformation is reversible but has an enhanced phase hysteresis, which results in the coexistence of both the α and β structure when temperature is warmed back. Presumably, the transformation temperature depends on the lattice parameter change in the type-B MnAs nanoparticles, which is influenced by the particle size or chemical doping. Testing of this hypothesis will be the subject of future experiments.

Chapter 5

General Synthesis of Transition Metal Arsenide Nanoparticles

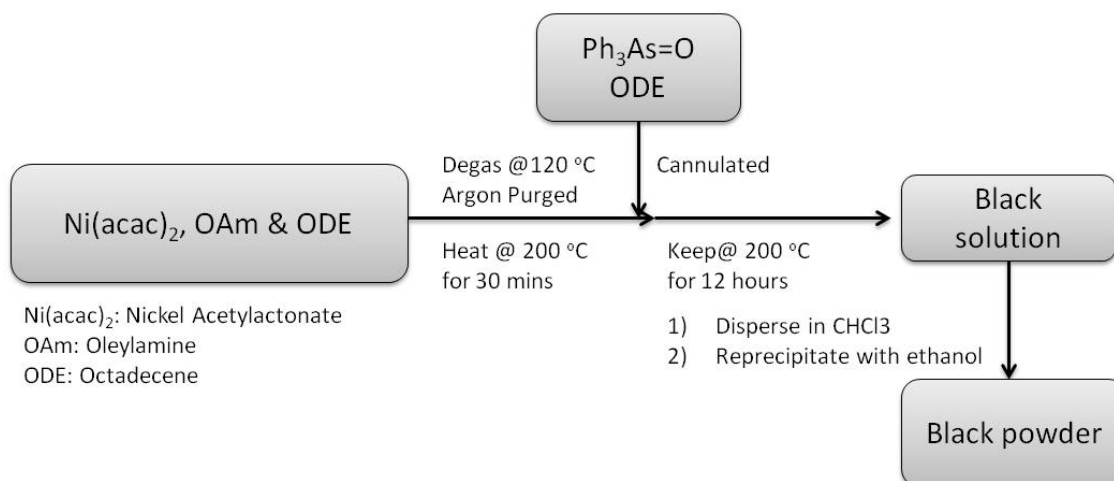
5.1 Introduction

In Chapter 1, the progress of synthetic methods for metal phosphide nanoparticles was summarized and the fact that a similar procedure can be adopted in the synthesis of metal arsenide nanoparticles was presented. However, there are a number of practical problems that result in considerably slower progress when nanoscale arsenides are targeted. One issue is the arsenic source. As trioctylarsine is not commercially available and triphenylarsine is too reactive at ≥ 250 °C, the arsenic source selected in the dissertation research was triphenylarsine oxide, which has been successfully used in MnAs nanoparticle synthesis. The other main problem is controlling the size and monodispersity during the synthesis, as triphenylarsine oxide is not a long chain compound and cannot serve as a sterically bulky coordinating ligand like TOP to prevent inhomogeneous growth. In this chapter, we will discuss synthetic strategies for transition metal arsenide nanoparticles enabling control of the size and polydispersity and application to arsenides of Fe, Co and Ni. FeAs and CoAs in bulk form are considered as antiferromagnetic/paramagnetic. For FeAs, antiferromagnetic behavior was observed below $T_N = 70$ K and for CoAs, there is no long range magnetic order shown in the bulk. As nanoparticles are confined in the short range, to synthesize the FeAs and CoAs nanoparticles will enable the studies of intrinsic magnetic orders or structures for these materials.⁹⁴ Besides, NiAs is shown the highest thermal/electric conductivity among 3-d transition metal arsenide materials, it will also be interesting to explore the size-dependent properties of these materials.⁹⁴

5.2 Metal Arsenide Nanoparticle Synthesis from Conversion of Metal Nanoparticles

For metal phosphide nanoparticle synthesis, the current popular general method was developed by Schaak and co-workers and involves producing metal nanoparticles first and converting them into metal phosphide nanoparticles.⁹⁵ In addressing the third aim of the dissertation research, I sought to apply this methodology to the synthesis of transition metal arsenide nanoparticles, as shown in Scheme 5.1.

Scheme 5.1 The synthesis of NiAs nanocrystals by metal nanoparticle conversion



Scheme 5.1 shows the general steps for the synthesis of transition metal arsenide nanocrystals, with NiAs synthesis as a prototype example. First, 1 mmol of reagent (Ni(acac)₂) was dissolved in 2 ml pre-dried oleylamine and 10 ml octadecene. The solution was heated and kept at 200 °C. During this time, the solution gradually turned black, suggesting Ni nanoparticle formation has occurred. Meanwhile, the As precursor was prepared by adding 1 mmol of triphenylarsine oxide into 10 ml octadecene. The preheated (80 °C) triphenylarsine oxide slurry was directly cannulated into the solution containing the Ni nanoparticles and then the reaction temperature was raised to 300-330 °C. The reaction temperature was maintained for 12 hours. The as-prepared sample was dispersed in chloroform and reprecipitated with

ethanol, followed by centrifugation. The final product was isolated as a black powder after drying. For FeAs and CoAs, the synthesis steps are almost the same except $\text{Fe}(\text{CO})_5$ and $\text{Co}_2(\text{CO})_8$ are used as the organometallic precursors for FeAs and CoAs, respectively. Figure 5.1 shows the PXRD patterns for the NiAs, FeAs and CoAs nanocrystals synthesized according to Scheme 5.1. The diffraction patterns match the reference patterns very well, indicating that the targeted transition metal arsenide phases have been formed. Moreover, unassigned peaks that could indicate impurity phase formation are not evident. Figure 5.2 shows TEM micrographs for various metal arsenide nanocrystals. Due to the growth speed and the structure difference, the size and morphologies vary for the different metals. For NiAs, the average size is about 35 nm, with some cube shaped nanocrystals; for FeAs, the particles resemble faceted plates of varying sizes (10-100 nm), and for CoAs, the product consists of spheres and aggregates with an average size of about 10 nm. In all cases, the samples are highly polydisperse.

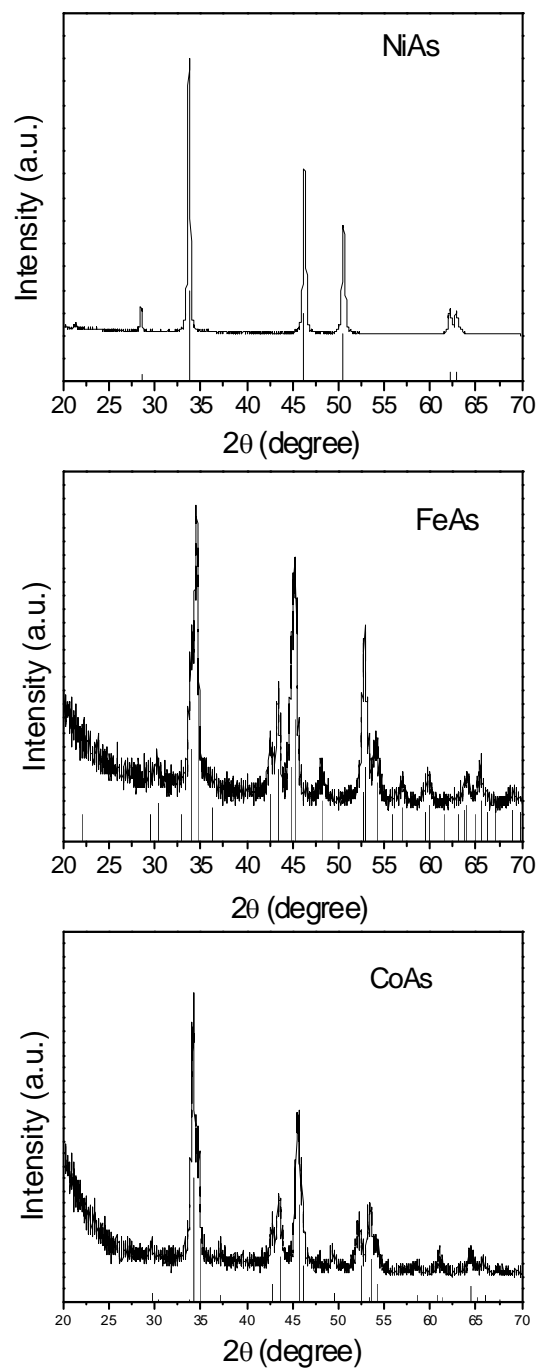


Figure 5.1 PXRD patterns for synthesized transition metal arsenide nanocrystals (from top to bottom): NiAs, FeAs and CoAs. The solid drop lines are the reference patterns for NiAs (PDF# 75-0603), FeAs (PDF# 71-2216) and CoAs (PDF# 77-1351).

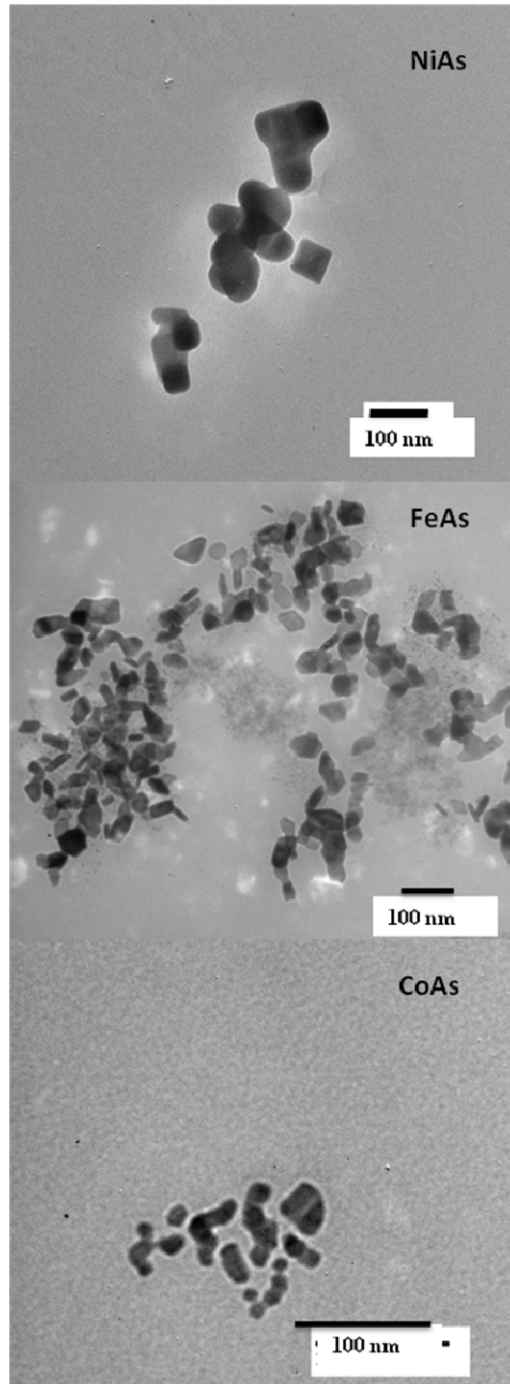
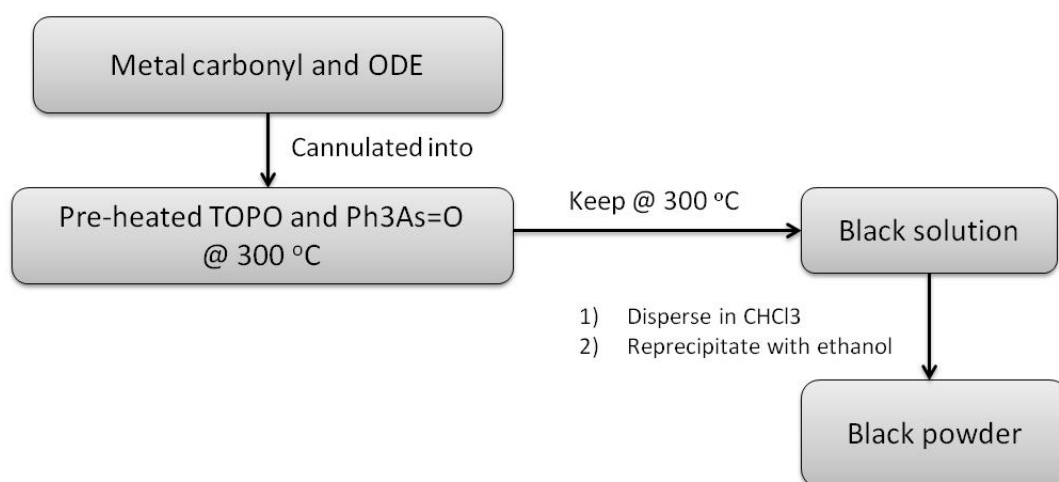


Figure 5.2 TEM micrographs for transition metal nanocrystals (from top to bottom): NiAs, FeAs and CoAs

5.3 Direct Reaction Synthesis of Transition Metal Arsenide Nanoparticles

There are several problems with the transition metal arsenide nanoparticle synthesis based on metal nanoparticle conversion that make this method less desirable than for phosphides. In metal phosphide nanoparticle syntheses, the TOP actually plays two roles in the reaction. It is both the phosphorus source and the coordinating ligand that controls the size of the formed metal nanoparticles. For metal arsenide nanoparticles, the arsenide source, triphenylarsine oxide, has shorter carbon chains/rings than the trioctylphosphine, which reduces its ability to help control the size of the formed metal nanoparticles. To avoid these issues, I instead pursued a reaction in which the metal precursor is injected into the arsenic precursor in a coordinating solvent, as shown in Scheme 5.2.

Scheme 5.2 The synthesis steps for preparation of metal arsenide nanoparticles by direct reaction



With the direct reaction method, the arsenic precursor is “pre-activated” and fully dissolved within the coordinating solvent system by preheating it in TOPO. During this time, the mixture color turns from a white to a dark-brown. The advantage of this process is that once the metal precursor is injected into the solution, it can directly react with the arsenic precursor without going through the metal nanoparticle formation and conversion process, and this can efficiently protect overgrowth. Figure 5.3 shows the PXRD patterns for FeAs and CoAs nanocrystals synthesized according to Scheme 5.2. The diffraction patterns match the reference patterns very well, indicating that the target transition metal arsenide phases have been formed. The TEM images of the synthesized nanoparticles are shown in Figure 5.4. Compared with the nanoparticles in Figure 5.3, it is clear that the nanoparticle sizes can be maintained below 20 nm and are more monodisperse.

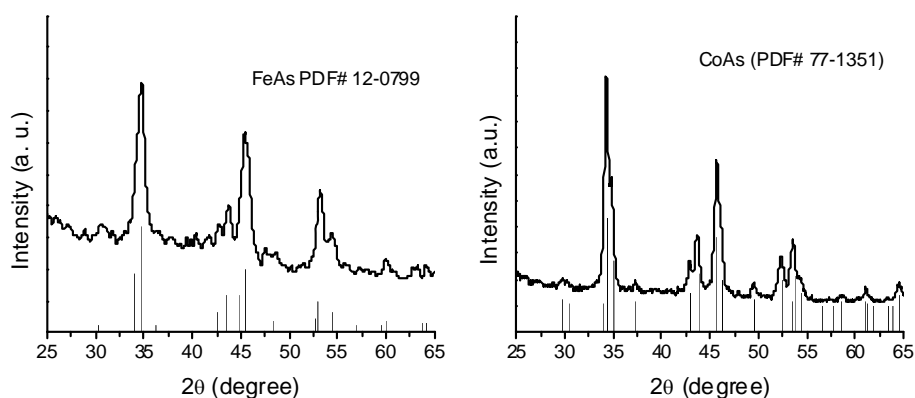


Figure 5.3 XRD patterns for synthesized transition metal arsenide nanocrystals: FeAs (left) and CoAs (right). The solid drop lines are the reference patterns for FeAs (PDF# 71-2216) and CoAs (PDF# 77-1351).

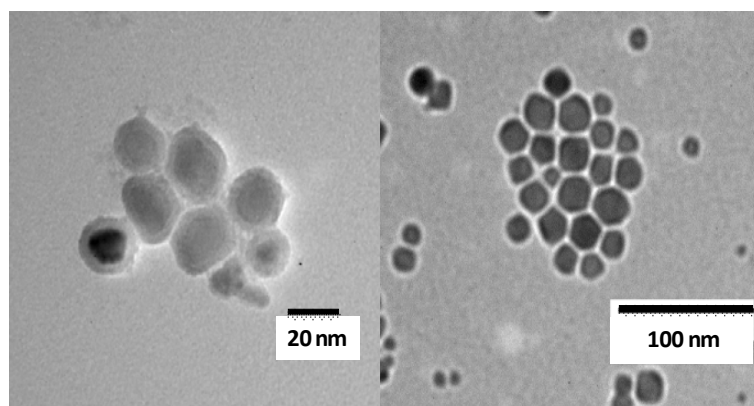


Figure 5.4 TEM images of transition metal arsenide nanocrystals: FeAs (left) and CoAs (right)

For the case of Ni, as $\text{Ni}(\text{CO})_4$ is highly toxic and not commercially available Bis(cyclooctadiene)nickel(0) ($\text{Ni}(\text{COD})_2$) was used instead. The XRD and TEM images for nickel arsenide nanoparticles prepared by this method are shown in Figure 5.5. In this case, the $\text{Ni}_{11}\text{As}_8$ phase was obtained perhaps a consequence of starting with a Ni(0) source instead of Ni(II), as used in the metal nanoparticle conversion strategy. Compared to the Figure 5.2, the size and dispersity has been controlled.

This method is also suitable for monodisperse MnAs nanoparticle synthesis. MnAs nanoparticles cannot be converted from Mn nanoparticles directly because Mn is very active and reacts with even small amounts of adventitious oxygen. In the previous MnAs synthesis, the nanoparticles are synthesized by injecting the metal and arsenic precursors together into the hot TOPO solvent. However, triphenylarsine oxide does not dissolve in octadecene, and the consequent heterogeneous mixtures do not lead to uniform nanoparticle samples, as shown in Figure 3.5 in Chapter 3. With this new method, because the arsenic precursor has been homogeneously dissolved in the solvent, it can be evenly reduced by $\text{Mn}_2(\text{CO})_{10}$ and form MnAs nanoparticles instantly, which gives rise to

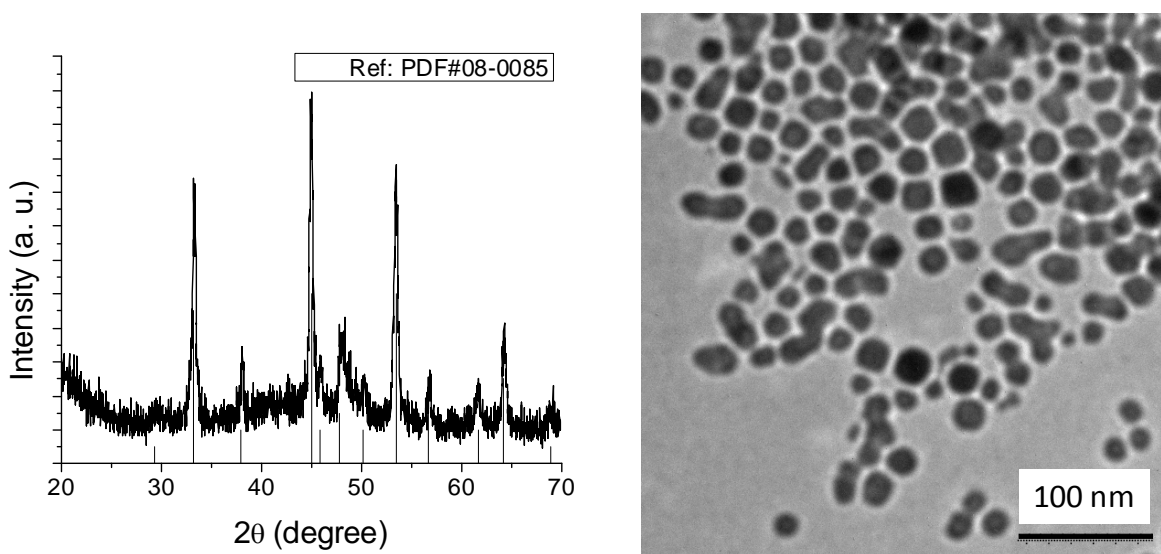


Figure 5.5 The XRD pattern (left) and TEM image (right) of nickel arsenide ($\text{Ni}_{11}\text{As}_8$) nanoparticles

monodisperse samples that are easily controlled and reproduced, as shown in Figure 4.2 and Figure 4.3 in Chapter 4.

5.4 Conclusion

In this chapter, I have successfully synthesized a series of transition metal arsenide nanocrystals ($\text{Ni}_{11}\text{As}_8$, FeAs and CoAs) by directly injecting the metal precursor into pre-reacted As precursors. This new method enables more control of the nanoparticle growth and monodispersity than that achieved by the direct conversion of metal nanoparticles. This opens the door to study of the size-dependent properties of these phases.

CHAPTER 6

Conclusions and Prospectus

6.1 Conclusions

During the last two decades, nanomaterials have drawn considerable interest and study due to their size and shape tunable physical properties (electronic, magnetic, catalytic, etc.). However, despite a good understanding of the bulk properties of binary pnictides, their nanoscale properties are still relatively unexplored, due in part to a lack of methodologies that enable size control on this scale. Hence, recent attention has turned to the development of synthetic methods to prepare nanoscale materials of transition metal pnictides. Among these methods, the solution phase arrested precipitation (SPAP) method has been proven effective for transition metal phosphide nanoparticles synthesis. However, the synthesis of nanoscale transition metal arsenides remains less studied relative to the related oxides, chalcogenides, and even phosphides, due in part to the metalloid nature of arsenic.

Among transition metal arsenides, bulk MnAs has been extensively studied for a long time due to its interesting first-order magneto-structural transformation properties and potential applications in information storage and energy devices. The temperature of the first-order phase transition in MnAs is sensitively influenced by the bond distances between Mn-Mn and Mn-As, and can be tuned by external pressure or internal chemical pressure (i.e. by doping). Current research on nanoscale MnAs is focused on epitaxially grown MnAs particles or disks on semiconducting thin films or nanowires. However, these MnAs nanomaterials are subject to external pressure due to lattice strain from the substrate. In order to discern the intrinsic magnetic

and structural properties of discrete unstrained MnAs nanoparticles, the Brock group synthesized MnAs nanoparticles with sizes from 9-23 nm in solution by reaction of dimanganesedecacarbonyl ($\text{Mn}_2(\text{CO})_{10}$) and triphenylarsine oxide ($((\text{C}_6\text{H}_5)_3\text{As}=\text{O})$) in coordinating solvents at temperatures ranging from 523-603 K. Intriguingly, either the α or β phase can be isolated at room temperature, depending on the synthesis temperature employed and whether the synthesis was conducted by slow heating (type-A MnAs nanoparticles) or rapid injection (type-B MnAs nanoparticles). Magnetic measurements of the type-A MnAs nanoparticles reveal a transition at 315 K. However, temperature dependent X-ray diffraction suggests that in type-A MnAs nanoparticles, there is no structural phase transition from α to β , even when the temperature is increased up to 343 K; this behavior is distinct from bulk materials, where the magneto-structural phase transition is observed at 313-317 K. Moreover, the type-B MnAs nanoparticles also appear to show ferromagnetic behavior with a phase transition near 315 K, which is distinct from bulk paramagnetic β -MnAs, but remarkably similar to type-A MnAs nanoparticles.

Another observation is that metastable type-B MnAs nanoparticles will convert, at least partially, from the β phase to the thermodynamically stable α phase over time at room temperature. Previous studies investigated size-dependent phase stability and transformation properties in other systems, mainly focusing on external pressure, field or internal chemical doping. However, there have been no studies of size-dependent stability in MnAs nanoparticles.

This dissertation research had three specific objectives: (1) to explore the interesting first-order magneto-structural phase transformation in bulk and nanoscale MnAs by combining the advanced Pair Distribution Function (PDF) method to probe the intrinsic atomic structure of MnAs and temperature-dependent magnetic susceptibility measurements; (2) to evaluate the

size-dependent metastability in type-B MnAs nanoparticles by studying the effect of post-synthesis processing conditions on phase stability at room temperature will be evaluated by employing variable temperature X-ray powder diffraction experiments and magnetic characterization; (3) to establish a general methodology for preparation of transition metal arsenides as discrete nanoparticles.

The first objective of this dissertation research was focused on relating the synthetic method for MnAs nanoparticles (to yield type-A vs type-B materials) to magnetic and structural properties. This goal was achieved by the synthesis of different room-temperature stable phases of MnAs nanoparticles (α or β) by employing slow heating or rapid injection methodologies, respectively. PDF analysis and Rietveld refinement confirms that the structural transition and the magnetic transition are highly correlated in bulk MnAs and suggest that for type-A MnAs nanoparticles, there is a similar magneto-structural phase transition occurring in the same temperature region as that for bulk MnAs. This is in contrast to prior data conducted using traditional PXRD methods in the same temperature region. For type-B MnAs nanoparticles, the β -model fits well over the entire temperature range, distinct from both bulk MnAs and type-A MnAs nanoparticles. The absence of a magneto-structural phase transition in type-B MnAs nanoparticles is consistent with type-B MnAs nanoparticles being kinetically trapped in the β -structure.

The second objective was to extend our synthesis of phase-pure, discrete and monodisperse type-B MnAs nanoparticles to produce nanoscale samples of varying sizes and discern the relationships among particle size, magnetic properties and structural phase in the absence of epitaxially imposed strain. Low and high temperature processing, as well as aging (at room-temperature) was employed in order to study the structural transformations of the type-B

MnAs nanoparticles. Temperature dependent PXRD studies were performed to assess the reversibility of the $\beta \rightarrow \alpha$ transition. The results suggested that the $\beta \rightarrow \alpha$ transition temperature, T_p , is depressed in type-B MnAs nanoparticles; while fully reversible, there is a large temperature hysteresis. The transformation temperature depends on the particle size, with smaller particles exhibiting a lower T_p than larger particles. Evaluation of a ca. 20 nm diameter sample reveals that the lattice parameter are compressed (PDF analysis) and that trace amounts of P are incorporated (STEM). P-incorporation is not noted in type-A MnAs. The incorporation of the P into MnAs lattice is unexpected but interesting, as previous studies have shown significant difficulties in achieving chemical doping during nanoparticle synthesis. The ability to induce transition temperature changes and vary the hysteresis through control of size/doping suggests the practicality of this material for room-temperature magneto-caloric applications.

In addressing the third objective, I have successfully synthesized a series of transition metal arsenide nanocrystals (MnAs, Ni₁₁As₈, FeAs and CoAs) by directly injecting the metal precursor into pre-reacted As precursors. This new method enables more control of the nanoparticle growth and monodispersity than that can be achieved by the direct conversion of metal nanoparticles. These nanoparticles open the door to the study of short range magnetic properties for these materials and comparison to the paramagnetic bulk materials.

6.2 Prospectus

6.2.1 Size-doping-property relationships

In this dissertation research, by reducing the size of MnAs into nanoparticles, the metastable orthorhombic MnAs structure can be kinetically trapped at room temperature, which

provides another example showing that the stability of materials (under pressure, electromagnetic field, or temperature) is related to the size. The size-dependency for the magneto-structural phase transformation of type-B MnAs nanoparticles revealed a reduced transition temperature and enhanced hysteresis, possibly related to lattice compression. In addition to lattice parameter changes due to size effect, the P dopant, which was detected by STEM, is another factor that causes the lattice compression of MnAs. It is necessary to establish if T_P is dependent only on doping or both doping and size. Previous work on chemical doping in bulk MnAs has shown the P doping could reduce the transition temperature,⁹⁶ however, in nanoparticles, the lattice compression can also come from the finite size effect. Future work should establish a relationship between the degree of chemical doping and the nanoparticle size. Also, the lattice expansion on the stability of type-B MnAs probed by the incorporation of larger anions like Sb, should be studied to see if this can increase the phase transition temperature and the hysteresis.⁹⁷

6.2.2 Synthesis Transition Metal Antimonides and Ternary Phases

This dissertation research also provides a general synthetic method for transition metal arsenide nanoparticles synthesis. A similar method can be applied in other transition metal pnictide nanoparticles syntheses, like transition metal antimonide nanoparticles due to magnetic and optical properties have been observed in these materials. The structure can also be changed by metal doping, for example $Fe_xMn_{1-x}As$, the ternary transition metal arsenides, has shown enhanced magneto-caloric properties relative to MnAs.⁹⁸ The transition temperature and the hysteresis vary with different x .

REFERENCES

1. Buzea, C.; Pacheco, I.; Robbie, K., Nanomaterials and nanoparticles: Sources and toxicity. *Biointerphases* **2007**, *2* (4), MR17-MR71.
2. Melosh, N. A.; Boukai, A.; Diana, F.; Gerardot, B.; Badolato, A.; Petroff, P. M.; Heath, J. R., Ultrahigh-Density Nanowire Lattices and Circuits. *Science* **2003**, *300* (5616), 112-115.
3. (a) Gleich, B.; Weizenecker, J., Tomographic imaging using the nonlinear response of magnetic particles. *Nature* **2005**, *435* (7046), 1214-1217; (b) Hyeon, T., Chemical synthesis of magnetic nanoparticles. *Chem. Commun.* **2003**, (8), 927-34.
4. (a) Kelly, K. L.; Coronado, E.; Zhao, L. L.; Schatz, G. C., The Optical Properties of Metal Nanoparticles: The Influence of Size, Shape, and Dielectric Environment. *J. Phys. Chem. B* **2002**, *107* (3), 668-677; (b) Seol, Y.; Carpenter, A. E.; Perkins, T. T., Gold nanoparticles: enhanced optical trapping and sensitivity coupled with significant heating. *Opt. Lett.* **2006**, *31* (16), 2429-31.
5. (a) Berseth, P. A.; Harter, A. G.; Zidan, R.; Blomqvist, A.; Araújo, C. M. s.; Scheicher, R. H.; Ahuja, R.; Jena, P., Carbon Nanomaterials as Catalysts for Hydrogen Uptake and Release in NaAlH₄. *Nano Lett.* **2009**, *9* (4), 1501-1505; (b) Buil, M. a. L.; Esteruelas, M. A.; Niembro, S.; Oliván, M.; Orzechowski, L.; Pelayo, C.; Vallribera, A., Dehalogenation and Hydrogenation of Aromatic Compounds Catalyzed by Nanoparticles Generated from Rhodium Bis(imino)pyridine Complexes. *Organometallics* **2010**, *29* (19), 4375-4383.
6. Klaine, S. J.; Alvarez, P. J. J.; Batley, G. E.; Fernandes, T. F.; Handy, R. D.; Lyon, D. Y.; Mahendra, S.; McLaughlin, M. J.; Lead, J. R., Nanomaterials in the environment: Behavior, fate, bioavailability, and effects. *Environ. Toxicol. Chem.* **2008**, *27* (9), 1825-1851.

7. (a) Nanomedicine: A matter of rhetoric? *Nat. Mater.* **2006**, 5 (4), 243-243; (b) Wagner, V.; Dullaart, A.; Bock, A.-K.; Zweck, A., The emerging nanomedicine landscape. *Nat Biotech* **2006**, 24 (10), 1211-1217.
8. (a) Swanson, R. M., Photovoltaics Power Up. *Science* **2009**, 324 (5929), 891-892; (b) Sun, B.; Marx, E.; Greenham, N. C., Photovoltaic Devices Using Blends of Branched CdSe Nanoparticles and Conjugated Polymers. *Nano Lett.* **2003**, 3 (7), 961-963.
9. Hameroff, S. R., Ultimate computing. Biomolecular consciousness and nano Technology. **1987**.
10. Akyildiz, I. F.; Jornet, J. M., Electromagnetic wireless nanosensor networks. *Nano Communication* **2010**, 1 (1), 3-19.
11. Portney, N. G.; Ozkan, M., Nano-oncology: drug delivery, imaging, and sensing. *Anal. Bioanal. Chem.* **2006**, 384 (3), 620-630.
12. El-Ghannam, A.; Ahmed, K.; Omran, M., Nanoporous delivery system to treat osteomyelitis and regenerate bone: Gentamicin release kinetics and bactericidal effect. *J Biomed Mater Res B* **2005**, 73 (2), 277-284.
13. (a) Coe, S.; Woo, W. K.; Bawendi, M.; Bulovic, V., United luminescence. *Nature* **2002**, 420, 800-803; (b) Sun, Q.; Wang, Y. A.; Li, L. S.; Wang, D.; Zhu, T.; Xu, J.; Yang, C.; Li, Y., Bright, multicoloured light-emitting diodes based on quantum dots. *Nat. Photonics* **2007**, 1 (12), 717-722; (c) Jang, H. S.; Yang, H.; Kim, S. W.; Han, J. Y.; Lee, S. G.; Jeon, D. Y., White Light-Emitting Diodes with Excellent Color Rendering Based on Organically Capped CdSe Quantum Dots and Sr₃SiO₅: Ce³⁺, Li⁺ Phosphors. *Adv. Mater.* **2008**, 20 (14), 2696-2702.

14. (a) Lent, C. S.; Tougaw, P. D., A device architecture for computing with quantum dots. *Proc. IEEE* **1997**, *85* (4), 541-557; (b) Kummamuru, R. K.; Orlov, A. O.; Ramasubramaniam, R.; Lent, C. S.; Bernstein, G. H.; Snider, G. L., Operation of a quantum-dot cellular automata (QCA) shift register and analysis of errors. *Electron Devices, IEEE Transactions on* **2003**, *50* (9), 1906-1913.
15. Daniel, M. C.; Astruc, D., Gold nanoparticles: assembly, supramolecular chemistry, quantum-size-related properties, and applications toward biology, catalysis, and nanotechnology. *Chem. Rev.* **2004**, *104* (1), 293.
16. (a) Brock, S. L.; Perera, S. C.; Stamm, K. L., Chemical Routes for Production of Transition-Metal Phosphides on the Nanoscale: Implications for Advanced Magnetic and Catalytic Materials. *Chem.-Eur. J.* **2004**, *10* (14), 3364-3371; (b) Gregg, K. A.; Perera, S. C.; Lawes, G.; Shinozaki, S.; Brock, S. L., Controlled synthesis of MnP nanorods: Effect of shape anisotropy on magnetization. *Chem. Mater.* **2006**, *18* (4), 879-886; (c) Brock, S. L.; Senevirathne, K., Recent developments in synthetic approaches to transition metal phosphide nanoparticles for magnetic and catalytic applications. *J. Solid State Chem.* **2008**, *181* (7), 1552-1559.
17. Burda, C.; Chen, X.; Narayanan, R.; El-Sayed, M. A., Chemistry and properties of nanocrystals of different shapes. *Chem. Rev.* **2005**, *105* (4), 1025-1102.
18. Klabunde, K. J.; Richards, R., *Nanoscale materials in chemistry*. Wiley Online Library: 2001.
19. Schmid, G., *Nanoparticles: from theory to application*. Wiley-VCH: 2011.
20. Willets, K. A.; Van Duyne, R. P., Localized Surface Plasmon Resonance Spectroscopy and Sensing. *Annu. Rev. Phys. Chem.* **2007**, *58* (1), 267-297.

21. (a) Lu, A.-H.; Schmidt, W.; Matoussevitch, N.; Bönemann, H.; Spliethoff, B.; Tesche, B.; Bill, E.; Kiefer, W.; Schüth, F., Nanoengineering of a Magnetically Separable Hydrogenation Catalyst. *Angew. Chem. Int. Ed.* **2004**, *43* (33), 4303-4306; (b) Gupta, A. K.; Gupta, M., Synthesis and surface engineering of iron oxide nanoparticles for biomedical applications. *Biomaterials* **2005**, *26* (18), 3995-4021.
22. (a) Wang, M. F.; Raghunathan, N.; Ziaie, B., A nonlithographic top-down electrochemical approach for creating hierarchical (micro-nano) superhydrophobic silicon surfaces. *Langmuir* **2007**, *23* (5), 2300-2303; (b) Walsh, S. T., Roadmapping a disruptive technology: A case study: The emerging microsystems and top-down nanosystems industry. *Technological Forecasting and Social Change* **2004**, *71* (1), 161-185; (c) Wang, Y.; Xia, Y., Bottom-up and top-down approaches to the synthesis of monodispersed spherical colloids of low melting-point metals. *Nano Lett.* **2004**, *4* (10), 2047-2050.
23. Hoepfner, S.; Maoz, R.; Cohen, S. R.; Chi, L.; Fuchs, H.; Sagiv, J., Metal Nanoparticles, Nanowires, and Contact Electrodes Self-Assembled on Patterned Monolayer Templates—A Bottom-up Chemical Approach*. *Adv. Mater* **2002**, *14* (15), 5.
24. Mijatovic, D.; Eijkel, J.; Van Den Berg, A., Technologies for nanofluidic systems: top-down vs. bottom-up—a review. *Lab on a Chip* **2005**, *5* (5), 492-500.
25. (a) Rajamathi, M.; Seshadri, R., Oxide and chalcogenide nanoparticles from hydrothermal/solvothermal reactions. *Curr. Opin. Solid State Mater. Sci.* **2002**, *6* (4), 337-345; (b) Yang, Y.; Matsubara, S.; Xiong, L.; Hayakawa, T.; Nogami, M., Solvothermal synthesis of multiple shapes of silver nanoparticles and their SERS properties. *J. Phys. Chem. C* **2007**, *111* (26), 9095-9104.

26. Wang, X.; Clark, P.; Oyama, S. T., Synthesis, characterization, and hydrotreating activity of several iron group transition metal phosphides. *J. Catal.* **2002**, *208* (2), 321-331.
27. (a) Liu, Z.; Lee, J. Y.; Chen, W.; Han, M.; Gan, L. M., Physical and electrochemical characterizations of microwave-assisted polyol preparation of carbon-supported PtRu nanoparticles. *Langmuir* **2004**, *20* (1), 181-187; (b) Zhu, J.; Palchik, O.; Chen, S.; Gedanken, A., Microwave assisted preparation of CdSe, PbSe, and Cu_{2-x}Se nanoparticles. *J. Phys. Chem. B* **2000**, *104* (31), 7344-7347.
28. (a) Sun, T. M.; Du, J. Z.; Yan, L. F.; Mao, H. Q.; Wang, J., Self-assembled biodegradable micellar nanoparticles of amphiphilic and cationic block copolymer for siRNA delivery. *Biomaterials* **2008**, *29* (32), 4348-4355; (b) Luan, Y.; Xu, G.; Sun, Z.; Dai, G.; Chen, Y.; Yu, L., Comparative Studies of AOT and NaDEHP by Fluorescence Technique and z-Potential (ζ) Measurements. *J. Dispersion Sci. Technol.* **2005**, *26* (3), 285-290.
29. (a) Qi, L.; Cölfen, H.; Antonietti, M., Synthesis and characterization of CdS nanoparticles stabilized by double-hydrophilic block copolymers. *Nano Lett.* **2001**, *1* (2), 61-65; (b) Peter, L. M.; Wijayantha, K. G. U.; Riley, D. J.; Waggett, J. P., Band-edge tuning in self-assembled layers of Bi₂S₃ nanoparticles used to photosensitize nanocrystalline TiO₂. *J. Phys. Chem. B* **2003**, *107* (33), 8378-8381.
30. Rodriguez, A.; Amiens, C.; Chaudret, B.; Casanove, M. J.; Lecante, P.; Bradley, J. S., Synthesis and isolation of cuboctahedral and icosahedral platinum nanoparticles. ligand-dependent structures. *Chem. Mater.* **1996**, *8* (8), 1978-1986.
31. Sau, T. K.; Murphy, C. J., Room temperature, high-yield synthesis of multiple shapes of gold nanoparticles in aqueous solution. *J. Am. Chem. Soc.* **2004**, *126* (28), 8648-8649.

32. (a) Dumestre, F.; Chaudret, B.; Amiens, C.; Respaud, M.; Fejes, P.; Renaud, P.; Zurcher, P., Unprecedented Crystalline Super-Lattices of Monodisperse Cobalt Nanorods. *Angew. Chem. Int. Ed.* **2003**, *42* (42), 5213-5216; (b) Liu, J.; Guo, Z.; Jia, Y.; Meng, F.; Luo, T., Triethylenetetramine (TETA)-assisted synthesis, dynamic growth mechanism, and photoluminescence properties of radial single-crystalline ZnS nanowire bundles. *J. Cryst. Growth* **2009**, *311* (5), 1423-1429.
33. (a) Puentes, V. F.; Krishnan, K. M.; Alivisatos, A. P., Colloidal nanocrystal shape and size control: The case of cobalt. *Science* **2001**, *291* (5511), 2115-2117; (b) Henkes, A. E.; Vasquez, Y.; Schaak, R. E., Converting metals into phosphides: A general strategy for the synthesis of metal phosphide nanocrystals. *J. Am. Chem. Soc.* **2007**, *129* (7), 1896-1897.
34. Klimov, V. I., *Semiconductor and metal nanocrystals: synthesis and electronic and optical properties*. CRC: 2003; Vol. 87.
35. (a) Murray, C.; Kagan, C.; Bawendi, M., Synthesis and characterization of monodisperse nanocrystals and close-packed nanocrystal assemblies. *Annu. Rev. Mater. Sci.* **2000**, *30* (1), 545-610; (b) LaMer, V. K.; Dinegar, R. H., Theory, production and mechanism of formation of monodispersed hydrosols. *J. Am. Chem. Soc.* **1950**, *72* (11), 4847-4854.
36. Myers, H. P., *Introductory solid state physics*. CRC: 1997.
37. Hulliger, F., Crystal chemistry of the chalcogenides and pnictides of the transition elements. *Struct. Bond.* **1968**, 83-229.
38. (a) Oyama, S. T., Novel catalysts for advanced hydroprocessing: transition metal phosphides. *J. Catal.* **2003**, *216* (1), 343-352; (b) Yang, J.; Kamaraju, K.; Yelon, W.; James, W.; Cai, Q.; Bollero, A., Magnetic properties of the MnBi intermetallic compound.

- Appl. Phys. Lett.* **2001**, 79 (12), 1846-1848; (c) Sweeney, C. M.; Stamm, K. L.; Brock, S. L., On the feasibility of phosphide generation from phosphate reduction: The case of Rh, Ir, and Ag. *J. Alloys Compd.* **2008**, 448 (1), 122-127; (d) Senevirathne, K.; Tackett, R.; Kharel, P. R.; Lawes, G.; Somaskandan, K.; Brock, S. L., Discrete, Dispersible MnAs Nanocrystals from Solution Methods: Phase Control on the Nanoscale and Magnetic Consequences. *ACS Nano* **2009**, 3 (5), 1129-1138.
39. Byrne, E. K.; Parkanyi, L.; Theopold, K. H., Design of a monomeric arsinogallane and chemical conversion to gallium arsenide. *Science* **1988**, 241, 332-334.
40. Gammon, D.; Snow, E.; Shanabrook, B.; Katzer, D.; Park, D., Homogeneous linewidths in the optical spectrum of a single gallium arsenide quantum dot. *Science* **1996**, 87-89.
41. (a) Zhang, X.; Wang, C.; Qian, X.; Xie, Y.; Qian, Y., Synthesis of nanocrystalline iron monoarsenide via a reductive recombination pathway. *J. Solid State Chem.* **1999**, 144 (2), 237-239; (b) Battaglia, D.; Peng, X., Formation of high quality InP and InAs nanocrystals in a noncoordinating solvent. *Nano Lett.* **2002**, 2 (9), 1027-1030.
42. (a) Takahashi, H.; Igawa, K.; Arii, K.; Kamihara, Y.; Hirano, M.; Hosono, H., Superconductivity at 43 K in an iron-based layered compound $\text{LaO}_{1-x}\text{F}_x\text{FeAs}$. *Nature* **2008**, 453 (7193), 376-378; (b) Rotter, M.; Tegel, M.; Johrendt, D., Superconductivity at 38 K in the Iron Arsenide $(\text{Ba}_{1-x}\text{K}_x)\text{Fe}_2\text{As}_2$. *Phys. Rev. Lett.* **2008**, 101 (10), 107006.
43. (a) Oppeneer, P.; Antonov, V.; Kraft, T.; Eschrig, H.; Yaresko, A.; Perlov, A. Y., First-principles study of the giant magneto-optical Kerr effect in MnBi and related compounds. *J. Appl. Phys.* **1996**, 80 (2), 1099-1105; (b) Buschow, K.; Van Engen, P.;

- Jongebreur, R., Magneto-optical properties of metallic ferromagnetic materials. *J. Magn. Mater.* **1983**, *38* (1), 1-22.
44. Koyano, M.; Kito, D.; Sakai, K.; Ariga, T., Synthesis and Electronic Properties of Thermoelectric and Magnetic Nanoparticle Composite Materials. *J. Electron. Mater.* **2011**, *40* (5), 1078-1082.
45. (a) Toprak, M. S.; Stiewe, C.; Platzek, D.; Williams, S.; Bertini, L.; Müller, E.; Gatti, C.; Zhang, Y.; Rowe, M.; Muhammed, M., The impact of nanostructuring on the thermal conductivity of thermoelectric CoSb₃. *Adv. Funct. Mater.* **2004**, *14* (12), 1189-1196; (b) Sun, P.; Oeschler, N.; Johnsen, S.; Iversen, B. B.; Steglich, F., Huge Thermoelectric Power Factor: FeSb₂ versus FeAs₂ and RuSb₂. *arXiv preprint arXiv:0910.0784* **2009**; (c) Bentien, A.; Johnsen, S.; Madsen, G. K. H.; Iversen, B. B.; Steglich, F., Colossal Seebeck coefficient in strongly correlated semiconductor FeSb₂. *EPL (Europhysics Letters)* **2007**, *80* (1), 17008.
46. (a) Yunle, G.; Fan, G.; Yitai, Q.; Huagui, Z.; Ziping, Y., A solvothermal synthesis of ultra-fine iron phosphide. *Mater. Res. Bull.* **2002**, *37* (6), 1101-1105; (b) Xie, Y.; Su, H.; Qian, X.; Liu, X.; Qian, Y., A mild one-step solvothermal route to metal phosphides (metal= Co, Ni, Cu). *J. Solid State Chem.* **2000**, *149* (1), 88-91; (c) Qian, X.; Xie, Y.; Qian, Y.; Zhang, X.; Wang, W.; Yang, L., Organo-thermal preparation of nanocrystalline cobalt phosphides. *Mater. Sci. Eng., B* **1997**, *49* (2), 135-137; (d) Wang, C.; Qian, X.; Zhang, X.; Li, Y.; Xie, Y.; Qian, Y., A new chemical route to prepare nanocrystalline cobalt monoarsenide. *Mater. Res. Bull.* **1999**, *34* (7), 1129-1133.
47. (a) Perera, S. C.; Fodor, P. S.; Tsoi, G. M.; Wenger, L. E.; Brock, S. L., Application of de-silylation strategies to the preparation of transition metal pnictide nanocrystals: the

- case of FeP. *Chem. Mater.* **2003**, *15* (21), 4034-4038; (b) Perera, S. C.; Tsoi, G.; Wenger, L. E.; Brock, S. L., Synthesis of MnP nanocrystals by treatment of metal carbonyl complexes with phosphines: A new, versatile route to nanoscale transition metal phosphides. *J. Am. Chem. Soc.* **2003**, *125* (46), 13960-13961.
48. (a) Muthuswamy, E.; Kharel, P. R.; Lawes, G.; Brock, S. L., Control of Phase in Phosphide Nanoparticles Produced by Metal Nanoparticle Transformation: Fe₂P and FeP. *ACS Nano* **2009**, *3* (8), 2383-2393; (b) Muthuswamy, E.; Brock, S. L., Solid-state phase transformations in solution: templated conversion of nanoscale nickel phosphides. *Chem. Commun.* **2011**, *47* (45), 12334-12336.
49. Malik, M.; O'Brien, P.; Norager, S.; Smith, J., Gallium arsenide nanoparticles: synthesis and characterisation. *J. Mater. Chem.* **2003**, *13* (10), 2591-2595.
50. (a) Pokrant, S.; Herwig, C.; Hihara, T.; Becker, J. A., Electronic spin-spin coupling in rare earth doped semiconductor and semimetal clusters. *Eur. Phys. J. D* **1999**, *9* (1), 509-512; (b) Gama, S.; Alves, C. S.; Coelho, A. A.; Ribeiro, C. A.; Persiano, A. I. C.; Silva, D., On the determination of the phase composition of the Gd₅Ge₂Si₂ alloy. *J. Magn. Magn. Mater.* **2004**, *272-76*, 848-849.
51. Ishikawa, F.; Koyama, K.; Watanabe, K.; Wada, H., Field induced structural transformation in MnAs. *Jpn J Appl Phys 2* **2003**, *42* (8A), L918-L920.
52. Chernenko, V. A.; Wee, L.; McCormick, P. G.; Street, R., Giant magnetoelastic response in MnAs. *J. Appl. Phys.* **1999**, *85* (11), 7833-7837.
53. De Campos, A.; Rocco, D. L.; Carvalho, A. M. G.; Caron, L.; Coelho, A. A.; Gama, S.; Da Silva, L. M.; Gandra, F. C. G.; Dos Santos, A. O.; Cardoso, L. P.; Von Ranke, P. J.;

- De Oliveira, N. A., Ambient pressure colossal magnetocaloric effect tuned by composition in $Mn_{1-x}Fe_xAs$. *Nat. Mater.* **2006**, 5 (10), 802-804.
54. Goodenough, J. B.; Kafalas, J. A., High-Pressure Study of the First-Order Phase Transition in MnAs. *Physical Review* **1967**, 157 (2), 389.
55. Ramsteiner, M.; Hao, H. Y.; Kawaharazuka, A.; Zhu, H. J.; Kastner, M.; Hey, R.; Daweritz, L.; Grahn, H. T.; Ploog, K. H., Electrical spin injection from ferromagnetic MnAs metal layers into GaAs. *Phys. Rev. B: Condens. Matter* **2002**, 66 (8), -.
56. Sun, N. K.; Cui, W. B.; Li, D.; Geng, D. Y.; Yang, F.; Zhang, Z. D., Giant room-temperature magnetocaloric effect in $Mn_{1-x}Cr_xAs$. *Appl. Phys. Lett.* **2008**, 92 (7), -.
57. (a) Ploog, K. H., Interplay of elastic and magnetic properties in MnAs/GaAs heterostructures. *Physica E* **2004**, 24 (1-2), 101-106; (b) Yokoyama, M.; Ohya, S.; Tanaka, M., Growth and magnetic properties of epitaxial MnAs thin films grown on InP(001). *Appl. Phys. Lett.* **2006**, 88 (1), -; (c) Ramlan, D. G.; May, S. J.; Zheng, J. G.; Allen, J. E.; Wessels, B. W.; Lauhon, L. J., Ferromagnetic self-assembled quantum dots on semiconductor nanowires. *Nano Lett.* **2006**, 6 (1), 50-54; (d) Hai, P. N.; Sakata, Y.; Yokoyama, M.; Ohya, S.; Tanaka, M., Spin-valve effect by ballistic transport in ferromagnetic metal (MnAs)/semiconductor (GaAs) hybrid heterostructures. *Phys. Rev. B: Condens. Matter* **2008**, 77 (21), -.
58. Takagaki, Y.; Herrmann, C.; Wiebicke, E.; Herfort, J.; Daweritz, L.; Ploog, K. H., Slow relaxation of magnetization in MnAs nanomagnets on GaAs(001). *Appl. Phys. Lett.* **2006**, 88 (3), -.
59. <http://www.chem.purdue.edu/chemsafety/SafetyClass/Injury/lecture/chapii.htm>.
60. <http://www.ilpi.com/inorganic/glassware/vacline.html>.

61. Cullity, B. D.; Stock, S. R., *Elements of X-ray Diffraction*. Prentice hall Upper Saddle River, NJ: 2001; Vol. 3.
62. West, A. R., *Basic solid state chemistry*. Wiley New York: 1988.
63. Patterson, A., The Scherrer formula for x-ray particle size determination. *Physical Review* **1939**, *56* (10), 978.
64. (a) Le Bail, A.; Madsen, I.; Cranswick, L. M. D.; Dinnebier, R.; Billinge, S., *Powder diffraction: theory and practice*. Royal Society of Chemistry: 2008; (b) Egami, T.; Billinge, S. J. L., Preface. *Pergamon Materials Series* **2003**, *7*, vii-x.
65. (a) Toby, B.; Egami, T., Accuracy of pair distribution function analysis applied to crystalline and non-crystalline materials. *Acta Crystallogr., Sect. A: Found. Crystallogr.* **1992**, *48* (3), 336-346; (b) Chupas, P. J.; Qiu, X.; Hanson, J. C.; Lee, P. L.; Grey, C. P.; Billinge, S. J. L., Rapid-acquisition pair distribution function (RA-PDF) analysis. *J. Appl. Crystallogr.* **2003**, *36* (6), 1342-1347.
66. de Broglie, L., Waves and quanta. *Nature* **1923**, *112* (2815), 540-540.
67. Thomas, J. M.; Ducati, C., *Transmission electron microscopy*. Wiley Online Library: 1979.
68. Williams, D. B.; Carter, C. B., *Transmission electron microscopy: a textbook for materials science*. Springer: 2009.
69. Fultz, B.; Howe, J., *Transmission electron microscopy and diffractometry of materials*. Springer: 2005.
70. Perovic, D.; Rossouw, C.; Howie, A., Imaging elastic strains in high-angle annular dark field scanning transmission electron microscopy. *Ultramicroscopy* **1993**, *52* (3), 353-359.
71. Clarke, J.; Braginski, A. I., *The SQUID handbook*. Wiley Online Library: 2006; Vol. 1.

72. Rungger, I.; Sanvito, S., Ab initio study of the magnetostructural properties of MnAs. *Phys. Rev. B: Condens. Matter* **2006**, *74* (2), 024429.
73. Zheng, R. T.; Gao, J. W.; Wang, J. J.; Chen, G., Reversible temperature regulation of electrical and thermal conductivity using liquid-solid phase transitions. *Nature Communications* **2011**, *2*.
74. Lu, H.; Bark, C. W.; de los Ojos, D. E.; Alcala, J.; Eom, C. B.; Catalan, G.; Gruverman, A., Mechanical Writing of Ferroelectric Polarization. *Science* **2012**, *336* (6077), 59-61.
75. Tegus, O.; Bruck, E.; Buschow, K. H. J.; de Boer, F. R., Transition-metal-based magnetic refrigerants for room-temperature applications. *Nature* **2002**, *415* (6868), 150-152.
76. (a) Tolbert, S. H.; Alivisatos, A. P., Size Dependence of a First-Order Solid-Solid Phase-Transition - the Wurtzite to Rock-Salt Transformation in CdSe Nanocrystals. *Science* **1994**, *265* (5170), 373-376; (b) Jacobs, K.; Zaziski, D.; Scher, E. C.; Herhold, A. B.; Alivisatos, A. P., Activation volumes for solid-solid transformations in nanocrystals. *Science* **2001**, *293* (5536), 1803-1806.
77. Kuwahara, H.; Tomioka, Y.; Asamitsu, A.; Moritomo, Y.; Tokura, Y., A First-Order Phase-Transition Induced by a Magnetic-Field. *Science* **1995**, *270* (5238), 961-963.
78. Ohno, H.; Chiba, D.; Matsukura, F.; Omiya, T.; Abe, E.; Dietl, T.; Ohno, Y.; Ohtani, K., Electric-field control of ferromagnetism. *Nature* **2000**, *408* (6815), 944-946.
79. Dai, Z. R.; Sun, S.; Wang, Z. L., Phase Transformation, Coalescence, and Twinning of Monodisperse FePt Nanocrystals. *Nano Lett.* **2001**, *1* (8), 443-447.
80. (a) Stanley, H. E., *Introduction to Phase Transitions and Critical Phenomena*. Oxford University Press: New York, 1987; (b) Challa, M. S. S.; Landau, D. P.; Binder, K.,

- Monte-Carlo Studies of Finite-Size Effects at 1st-Order Transitions. *Phase Transitions* **1990**, 24-6 (1), 343-369.
81. Zheng, H. M.; Rivest, J. B.; Miller, T. A.; Sadtler, B.; Lindenberg, A.; Toney, M. F.; Wang, L. W.; Kisielowski, C.; Alivisatos, A. P., Observation of Transient Structural-Transformation Dynamics in a Cu₂S Nanorod. *Science* **2011**, 333 (6039), 206-209.
82. (a) Farvid, S. S.; Radovanovic, P. V., Phase Transformation of Colloidal In₂O₃ Nanocrystals Driven by the Interface Nucleation Mechanism: A Kinetic Study. *J. Am. Chem. Soc.* **2012**, 134 (16), 7015-7024; (b) Wang, C. M.; Li, X. L.; Wang, Z. G.; Xu, W.; Liu, J.; Gao, F.; Kovarik, L.; Zhang, J. G.; Howe, J.; Burton, D. J.; Liu, Z. Y.; Xiao, X. C.; Thevuthasan, S.; Baer, D. R., In Situ TEM Investigation of Congruent Phase Transition and Structural Evolution of Nanostructured Silicon/Carbon Anode for Lithium Ion Batteries. *Nano Lett.* **2012**, 12 (3), 1624-1632.
83. Chiba, D.; Yamanouchi, M.; Matsukura, F.; Ohno, H., Electrical manipulation of magnetization reversal in a ferromagnetic semiconductor. *Science* **2003**, 301 (5635), 943-945.
84. Mira, J.; Rivadulla, F.; Rivas, J.; Fondado, A.; Guidi, T.; Caciuffo, R.; Carsughi, F.; Radaelli, P. G.; Goodenough, J. B., Structural transformation induced by magnetic field and "Colossal-Like" magnetoresistance response above 313 K in MnAs (vol 90, art no 097203, 2003). *Phys. Rev. Lett.* **2003**, 90 (18).
85. Lazewski, J.; Piekarz, P.; Tobola, J.; Wiendlocha, B.; Jochym, P. T.; Sternik, M.; Parlinski, K., Phonon Mechanism of the Magnetostructural Phase Transition in MnAs. *Phys. Rev. Lett.* **2010**, 104 (14).

86. Tian, P.; Zhang, Y.; Senevirathne, K.; Brock, S. L.; Dixit, A.; Lawes, G.; Billinge, S. J. L., Diverse Structural and Magnetic Properties of Differently Prepared MnAs Nanoparticles. *ACS Nano* **2011**, *5* (4), 2970-2978.
87. Zhang, H.; Ha, D.-H.; Hovden, R.; Kourkoutis, L. F.; Robinson, R. D., Controlled Synthesis of Uniform Cobalt Phosphide Hyperbranched Nanocrystals Using Tri-n-octylphosphine Oxide as a Phosphorus Source. *Nano Lett.* **2010**, *11* (1), 188-197.
88. Schwartz, L. H.; Hall, E. L.; Felcher, G. P., Magnetic Structure of MnAs and MnAs_{0.92}P_{0.08}. *J. Appl. Phys.* **1971**, *42* (4), 1621-1622.
89. Schwartz, L.; Hall, E.; Felcher, G., Magnetic Structure of MnAs and MnAsP. *J. Appl. Phys.* **1971**, *42*, 1621.
90. Alivisatos, A. P.; Harris, T. D.; Brus, L. E.; Jayaraman, A., Resonance Raman-Scattering and Optical-Absorption Studies of Cdse Microclusters at High-Pressure. *J. Chem. Phys.* **1988**, *89* (10), 5979-5982.
91. Kodama, R. H., Magnetic nanoparticles. *J. Magn. Magn. Mater.* **1999**, *200* (1-3), 359-372.
92. Billas, I. M. L.; Chatelain, A.; Deheer, W. A., Magnetism from the Atom to the Bulk in Iron, Cobalt, and Nickel Clusters. *Science* **1994**, *265* (5179), 1682-1684.
93. Iikawa, F.; Brasil, M. J. S. P.; Adriano, C.; Couto, O. D. D.; Giles, C.; Santos, P. V.; Däweritz, L.; Rungger, I.; Sanvito, S., Lattice Distortion Effects on the Magnetostructural Phase Transition of MnAs. *Phys. Rev. Lett.* **2005**, *95* (7), 077203.
94. Bayrammurad, S.; Jonathan, E. M.; Athena, S. S., Properties of binary transition-metal arsenides (TAs). *Supercond. Sci. Technol.* **2012**, *25* (8), 084016.

95. Henkes, A. E.; Schaak, R. E., Trioctylphosphine: A general phosphorus source for the low-temperature conversion of metals into metal phosphides. *Chem. Mater.* **2007**, *19* (17), 4234-4242.
96. (a) Andresen, A.; Fjellvåg, H.; Skjeltorp, A.; Bärner, K. In *The structural and magnetic properties of MnAsP studied by neutron diffraction and magnetization measurements*, AIP Conference Proceedings, 1982; p 324; (b) Berg, H., The Magnetic Anisotropy of Orthorhombic MnAs. *97P0. 03. physica status solidi (a)* **1977**, *40* (2), 559-566.
97. (a) Wada, H.; Tanabe, Y., Giant magnetocaloric effect of $\text{MnAs}_{1-x}\text{Sb}_x$. *Appl. Phys. Lett.* **2001**, *79* (20), 3302-3304; (b) Ishikawa, F.; Koyama, K.; Watanabe, K.; Asano, T.; Wada, H., Structural Transformation of $\text{MnAs}_{1-x}\text{Sb}_x$ under High Magnetic Fields. *Mater. Trans., JIM* **2004**, *45* (2), 311-314.
98. Sun, N.; Ma, S.; Zhang, Q.; Du, J.; Zhang, Z., Large room-temperature magnetocaloric effects in $\text{Fe}_{0.8}\text{Mn}_{1.5}\text{As}$. *Appl. Phys. Lett.* **2007**, *91* (11), 112503-112503-3.

ABSTRACT**SYNTHESIS AND CHARACTERIZATION OF TRANSITION METAL
ARSENIDE NANOCRYSTALS AND THE METASTABILITY AND
MAGNETO-STRUCTURAL PHASE TRANSITION BEHAVIOR OF MNAS
NANOCRYSTALS**

by

YANHUA ZHANG**May 2013****Advisor:** Dr. Stephanie L. Brock**Major:** Chemistry**Degree:** Doctor of Philosophy

This dissertation study focuses on (1) probing the magneto-structural phase transformation in nanoscale MnAs; (2) evaluation of the size-dependent phase stability of type-B MnAs (prepared by rapid injection); and (3) developing a general synthetic method for transition metal arsenide nanoparticles.

Discrete MnAs nanoparticles that adopt different structures at room temperature (type-A, α -structure and type-B, β -structure) have been prepared by solution-phase arrested precipitation. Atomic pair distribution and Rietveld refinement were employed on synchrotron data to explore the structural transitions of the bulk and nanoparticle samples, and these results were compared to AC magnetic susceptibility measurements of the samples. The results confirm that the structural transition and the magnetic transition are highly correlated in bulk MnAs and suggest that for type-A MnAs nanoparticles, there is a similar magneto-structural phase transition occurring in the same temperature region as that for bulk MnAs. However, for type-B MnAs

nanoparticles, there is no magneto-structural phase transition, consistent that type-B MnAs nanoparticles being kinetically trapped in the β -structure.

Type-B MnAs nanoparticles adopting the β -structure undergo a transformation from β to α upon cooling. Temperature dependent XRD studies and magnetic measurements suggest that the T_p for $\alpha \rightarrow \beta$ conversion is suppressed to lower temperatures relative to bulk and type-A MnAs nanoparticles and that the transformation is reversible but has an enhanced hysteresis, which results in a large coexistence temperature range for the α and β structure. The transformation temperature may be correlated with the compression of the lattice parameters of the type-B MnAs nanoparticles due to the decrease in the particle size, the presence of chemical doping, or both.

A new general synthetic method for transition metal arsenide ($\text{Ni}_{11}\text{As}_8$, FeAs and CoAs) nanocrystals synthesis was developed by directly injecting the metal precursor into pre-reacted arsenic precursors. This method enables more control of the nanoparticle growth and monodispersity than is achieved by the direct conversion of metal nanoparticles.

AUTOBIOGRAPHICAL STATEMENT

YANHUA ZHANG

Education

- **2007-2013 Ph.D.** Inorganic Chemistry, Wayne State University, Detroit, MI
Dissertation: Synthesis and Characterization of Transition Metal Arsenide Nanoparticles and the Metastability and Magneto-structural Phase Transition Behavior of MnAs Nanocrystals
- **2004-2007 M.S.** Physical Chemistry, Nanjing University, Nanjing, China
- **2000-2004 B.S.** Chemistry, Nanjing University, Nanjing, China

Research and Teaching Experience

- **08/2007-12/2012** Graduate Teaching/Research Assistant, Department of Chemistry, Wayne State University, Detroit, MI

Affiliation and Fellowships

- Member of American Chemical Society
- Member of Phi-Lambda-Upsilon (PLU)
- Summer Dissertation Fellowship, WSU Graduate School, Summer 2012
- Graduate School Travel Award, Spring, 2012

Technical Skills

- Powder X-ray Diffraction (XRD), Differential Scanning Calorimetry (DSC), Transmission Electron Microscopy (TEM), Energy Dispersive Spectroscopy (EDS), UV-Visible and Infra-Red Spectroscopy (UV-vis and FTIR), Dynamic Light Scattering (DLS), Porosimetry Analysis.
- Handling air-sensitive chemicals by using glove-box and Schlenk line techniques

Publications

- Zhang, Y.; Gao, F.; Wan, H.; Wu, C.; Kong, Y.; Wu, X.; Zhao, B.; Dong, L.; Chen, Y. *Microporous Mesoporous Mater.* **2008**, 113, 393-401.
- Tian, P.; Zhang, Y.; Senevirathne, K.; Brock, S.; Dixit, A.; Lawes, G.; Billinge, S. *ACS Nano* **2011**, 5, 2970-2978.
- Gao, F.; Zhang, Y.; Wan, H.; Kong, Y.; Wu, X.; Dong, L.; Li, B.; Chen, Y. *Microporous Mesoporous Mater.* **2008**, 110, 508-516.
- Gao, F.; Zhang, Y.; Wang, C.; Wu, C.; Kong, Y.; Zhao, B.; Dong, L.; Chen, Y. *J. Nanosci. Nanotechnol.* 2007, 7, 4508-4514.
- Kong, Y.; Zhang, Y.; Wa, X.; Wang, J.; Wan, H.; Dong, L.; Yan, Q. *Stud. Surf. Sci. Catal.* 2007, 165, 749-754.

